# Experimental Study of Flat Plate Drag Reduction by Air Lubrication

*Sushma Pammi*

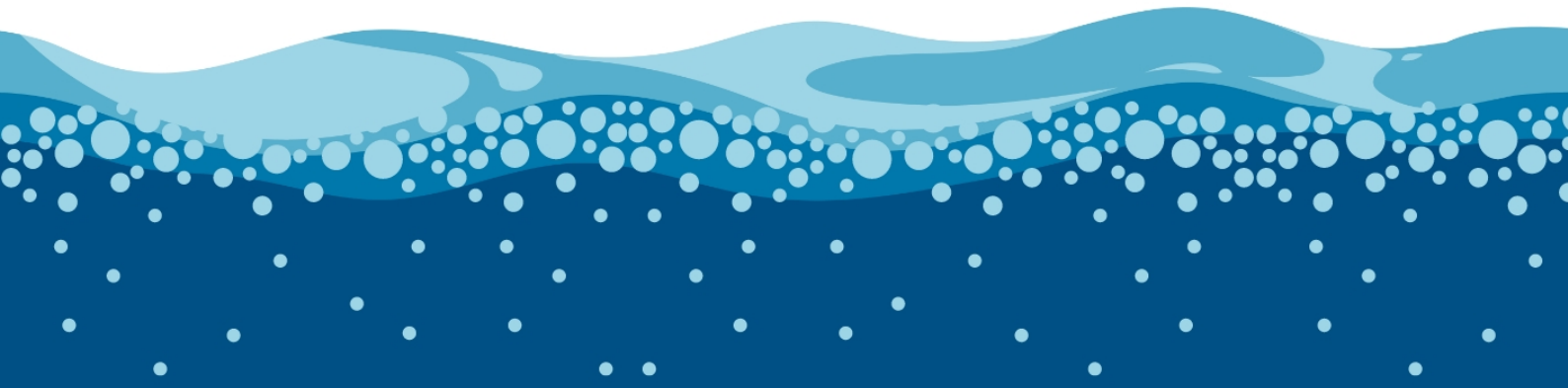

Thesis for the degree of MSc in Marine Technology
in the specialization of *Ship Hydromechanics*

# Experimental Study of Flat Plate Drag Reduction by Air Lubrication

By

Sushma Pammi

This thesis (MT.23/24.032.M) is classified as confidential in accordance with the general conditions for projects performed by the TU Delft.

19 June 2024

**Thesis Exam Committee**
Chair/Responsible Professor: Dr.ir. Tom van Terwisga
Staff Member: Dr. Angeliki Laskari
Staff Member: ir. Lina Nikolaidou
External Faculty Member: Dr.ing. Cornel Thill

**Author Details**
Student Number: 5465060
Author Contact E-Mail: pammisushma17@gmail.com

# Acknowledgement

I would like to express my sincere gratitude to all the individuals whose contributions were instrumental in the successful completion of this project. Without their unwavering support, invaluable insights, and unfailing guidance, this project would not have been possible.

Firstly, my earnest appreciation goes to Dr.ir. Tom van Terwisga, who chaired this project. I am thankful to him for his approachability and for providing me with the opportunity to work on a topic that aligns with my interests. His practical advice and reassuring presence helped me maintain focus and shape the trajectory of this work.

I am profoundly grateful to Dr. Angeliki Laskari and ir. Lina Nikolaidou for their constructive feedback, which significantly enhanced this work. Their dedication to excellence has significantly enriched the depth and quality of this work and profoundly influenced my academic growth. The intellectual exchanges and shared experiences I have had with them made my graduation journey memorable and rewarding.

I would also like to extend my gratitude to the esteemed staff at the Ship Hydromechanics Laboratory of Delft University of Technology. Their resourcefulness and pragmatic approach in managing advanced equipment were crucial to the execution of experiments for this work.

Finally, I am deeply indebted to my family, friends, housemates, and colleagues at TU Delft for their moral support and encouragement. Their patience and understanding have given me strength to persevere through the toughest times. I hope this work adds to their happiness and sense of pride, as their belief in me has been a significant source of motivation.

*Sushma Pammi*
*Delft, June 2024*

# Abstract

Drag reduction in ships is a key approach to decreasing their energy consumption. Besides saving fuel costs, it also decreases greenhouse gas emissions. One of the most promising techniques for drag reduction in ships is air lubrication, which reduces drag due to friction. Despite its great potential, application of air lubrication in the maritime industry is limited, owing to a lack of understanding of its underlying physical phenomena and stability issues.

The present work aims to experimentally study drag reduction on a flat plate resulting from air lubrication at a representative free-stream velocity of 2.5 m/s over a set of increasing air injection rates covering all the three air layer regimes (BDR, TALDR, ALDR) and assess its dependence on air morphology in terms of the plate's non-wetted area. The experiments were conducted at the Multi-Phase Flow Tunnel located at the Ship Hydromechanics group of TU Delft.

To achieve this, first, a custom force balance comprising a spring system was designed to facilitate the measurement of the total drag acting on the plate by means of a load cell. Drag measurements in single-phase flow were conducted on a conventional flat plate to obtain a reference dataset and validate the drag measurement system. An uncertainty analysis was performed to quantify the measurement accuracy. Then, single-phase and dual-phase experiments were conducted on another plate of similar dimensions fitted with additional parts necessary for the generation of air lubrication. For the quantification of the plate's non-wetted area in dual phase flow, these experiments were accompanied by image capture with cameras positioned vertically below the plate. The recorded images were processed using a binary approach to distinguish regions under the plate covered with water and air. Finally, the non-wetted area ratio of the plate was computed based on these processed images. Uncertainty in both drag reduction and the non-wetted area ratio was also determined before analysing the results.

Results from the present work indicate a positive linear correlation between drag reduction and the associated non-wetted area ratio achieved in BDR and ALDR. However, this correlation varies in slope per air layer regime, possibly due to the physical phenomena governing the regime. Thus, further investigation into the underlying physical phenomena governing each regime could shed light on the reason(s) for different slopes in the correlation. To improve the current work, estimation of the non-wetted area ratio in the TALDR regime may be carried out to increase the resolution of the correlation found. Moreover, the non-wetted area resulting from the thickness of the air layer may also be studied to define the non-wetted area ratio of the plate more accurately.

# Contents


Acknowledgement ii

Abstract iii

1 Introduction 1
- 1.1 Motivation . . . 1
- 1.2 Background . . . 1
- 1.3 Scope . . . 3
- 1.4 Outline . . . 3

2 Literature Review 5
- 2.1 Turbulent Boundary Layer . . . 5
- 2.2 Bubble Drag Reduction . . . 7
- 2.3 Transitional and Air Layer Drag Reduction . . . 12
- 2.4 Partial Cavity Drag Reduction . . . 14
- 2.5 Experimental Techniques and Instrumentation . . . 16
- 2.6 Research Objectives . . . 17

3 Experimental Setup 19
- 3.1 Setup . . . 19
  - 3.1.1 Multi-Phase Flow Tunnel . . . 19
  - 3.1.2 Flat Plates . . . 19
  - 3.1.3 Zig-Zag Strip . . . 20
  - 3.1.4 Sensors . . . 21
    - 3.1.4.1 Total Drag . . . 21
    - 3.1.4.2 Temperature . . . 23
    - 3.1.4.3 Free-Stream Velocity . . . 24
    - 3.1.4.4 Air Injection Rate . . . 24
  - 3.1.5 Force Balance . . . 24
    - 3.1.5.1 Deflection due to drag . . . 24
    - 3.1.5.2 Buckling . . . 26
  - 3.1.6 Cameras . . . 27
- 3.2 Calibration . . . 27

4 Data Acquisition and Processing 32
- 4.1 Conventional Plate . . . 32
- 4.2 Test Plate . . . 33
  - 4.2.1 Images . . . 33
    - 4.2.1.1 Image Processing . . . 34

5 Uncertainty Analysis 37
- 5.1 Conventional Plate . . . 37

5.1.1 Friction Coefficient . . . 37
5.2 Test Plate . . . 39
5.2.1 Friction Coefficient . . . 39
5.2.2 Drag Reduction . . . 39
5.2.3 Effective Drag Reduction . . . 39
5.2.4 Non-Wetted Area Ratio . . . 39
6 Results and Discussion 41
7 Conclusions and Recommendations 47
7.1 Conclusions . . . 47
7.2 Recommendations . . . 48
7.2.1 Improvements . . . 48
7.2.2 Further Research . . . 48
A Image Processing Code 49
Bibliography 69
Nomenclature 71

# List of Figures


1.1 Conceptual sketches of ADR techniques . . . 3

2.1 BDR results from a few initial studies . . . 8
2.2 Mean wall shear stress acting on the top wall of the minimum turbulent channel versus time for flows with and without bubbles. (Lu et al., 2005) . . . 10
2.3 Schematic diagram of the test model. For clarity, the model is presented with the test surface facing upward. (Sanders et al., 2006) . . . 10
2.4 Measured skin friction ratio versus non-wetted area ratio. UI = upstream air injection at $x$ = 1.32 m; DI = downstream air injection at $x$ = 9.79 m. (Sanders et al., 2006) . . . 11
2.5 Flow speed versus bubble size (Murai, 2014) . . . 12
2.6 Drag reduction and key injection rates corresponding to the three regimes of BDR, TALDR, and ALDR . . . 13
2.7 Non-wetted area and normalised non-wetted area versus air flow rate (Nikolaidou et al., 2021) 14
2.8 Air-layer length and thickness versus free-stream velocity for two different stream-wise positions, $x = 1.45$m and 3.95 m (Nikolaidou et al., 2022) . . . 15
2.9 Experimental setup used by (Zverkhovskyi, 2014) . . . 15

3.1 Technical drawings of the MPFT (Fiscaletti et al., 2023) . . . 20
3.2 Parts of the test plate . . . 21
3.3 Theoretically estimated drag (based on Prandtl-Schlichting formula) versus free-stream velocity for the intended test conditions . . . 23
3.4 Sectional view of the setup inside the test section . . . 25
3.5 Spring System . . . 26
3.6 Effective length of a column with one end fixed and one free end (Rajput, 2018) . . . 27
3.7 Setup of the cameras underneath the test section indicating their respective FOV along with regions of overlap. (not to scale; for representative purposes only) . . . 28
3.8 Wet calibration setup . . . 29
3.9 Wet calibration results (a), (b) - Conventional Plate (c), (d) - Test Plate . . . 31

4.1 Signals of measured parameters from a sample run at $U_\infty = 2.11$ m/s . . . 32
4.2 A glance at the steps involved in image processing for the upstream camera and $Q_{air} = 30$ l/min. Flow direction is from right to left. . . . 36

5.1 Block diagram of the test procedure . . . 37
5.2 Overlay of the code-generated result (light red) upon the corrected grayscale image corresponding to the upstream camera and $Q_{air} = 50$ l/min. . . . 40

6.1 Comparison of experimentally determined $C_F$ versus $Re$ of the conventional plate with different friction lines . . . 41
6.2 Drag versus free-stream velocity . . . 42
6.3 Distribution of wetted surface area of the test plate . . . 43
6.4 Drag reduction, effective drag reduction and non-wetted area ratio versus air injection rate at a representative free-stream velocity of 2.5 m/s . . . 44

6.5 Images corresponding to the middle camera and $Q_{air}$ = {30, 60, 100} captured at an instance of time . . . . . 45
6.6 Drag reduction versus non-wetted area ratio at a representative free-stream velocity of 2.5 m/s and increasing air injection rates . . . . . 45

# List of Tables


2.1 Distinct experimental techniques & instrumentation employed in previous studies discussed above . . . 16
2.2 Overview of parameters considered for present study . . . 18

3.1 Dimensions of the two plates used . . . 20
3.2 Intended test conditions . . . 22
3.3 Different cases of drag estimated at the intended test conditions in single-phase flow . . . 23
3.4 Details of the spring system . . . 25
3.5 Specifications of the cameras used in dual-phase experiments . . . 28
3.6 Details of wet calibration . . . 30

4.1 Camera settings for image capture in dual-phase flow . . . 34

5.1 Experimental data . . . 37

6.1 Experimental data used in drag reduction estimates . . . 46

# 1 Introduction

*This chapter explains the motivation and background that lead to the present study. It also briefly describes the objective and scope of the study defined from this literature research. Finally, a short outline of the content of this report is provided.*

## 1.1 Motivation

The ever-growing fuel costs and the newly imposed emission restrictions by International Maritime Organisation (2022) impact the shipping industry enormously. While several energy saving technologies (ESTs) such as bow enhancements, bow foils, and hull fins are applicable for ship hulls (Gao, 2022), these demand a considerable amount of modification to the hull. On the other hand, requiring minimal hull modification and boasting proven fuel savings between 5% and 10% (Silverstream Technologies, 2023), *air lubrication* is one of the rising ESTs for optimising ships' energy efficiency. However, this technology is not widely adopted as questions persist about its underlying physical mechanisms and the associated drag reduction performance. For example, an important challenge to the practical implementation of this technology is achieving and maintaining a stable air layer. This sets the purpose of the current study.

## 1.2 Background

Air lubrication, otherwise known as *air drag reduction* (ADR), is an active method to reduce the *skin friction drag* or frictional resistance in ships. Since this technology uses air, which, at normal temperature and pressure, is known to have $\sim 1/50$ times the viscosity and $\sim 1/800$ times the density of water, it has the potential to result in energy-saving effects under suitable interaction conditions. According to ITTC (1972), the total resistance of a ship is the sum of the tangential (shear) and normal forces acting on its wetted surface. The integration of shear stresses is called skin friction drag.

The frictional resistance coefficient, $C_F$ is defined as (e.g.,Larsson et al. (2010)):

$$C_F = \frac{R_F}{\frac{1}{2}\rho S V^2} \tag{1.1}$$

where $R_F$ is frictional resistance, $\rho$ is water density, $V$ is ship speed, and $S$ is wetted surface area of hull.

In *displacement vessels* (e.g.,Woud and Stapersma (2002)), the speed-dependent friction drag forms up to 85% of the total resistance when travelling at *low speeds* (less than 20 knots). The magnitude of frictional resistance or drag mainly depends on the Reynolds number, *Re*, defined by Equation (1.2), where $V$ is flow velocity, $D$ is characteristic diamter, $L$ is characteristic length, and $\nu$ is kinematic viscosity of fluid.

$$Re = \frac{VD}{\nu} = \frac{VL}{\nu} \tag{1.2}$$

On the other hand, when travelling at *high speeds* (between 20 and 25 knots), frictional resistance makes up only about 40% of the total resistance. This is because at higher speeds, radiation of waves by the hull

increases, thus implying the appearance of another speed-dependent type of resistance; *wave resistance*. Although frictional resistance constitutes a relatively lower proportion of the total resistance, it is still large in magnitude because the resistance encountered at higher speeds is larger. The magnitude of wave resistance mainly depends on the Froude number, $Fr$ defined by Equation (1.3), where $g$ is acceleration due to gravity.

$$Fr = \frac{V}{\sqrt{gL}} \tag{1.3}$$

Therefore, logically, air lubrication technology can particularly yield better drag reduction in low-speed displacement vessels, like bulk carriers and tankers.

Air lubrication can be applied under a flat surface by several methods (Mäkiharju et al., 2012, Pavlov et al., 2020) as described below.

1. **Bubble Drag Reduction** (BDR)
   Air is released into the boundary layer coating the ship bottom from a series of slots, nozzles, openings, or porous material flush with the surface designed to generate a bubble stream, so the flow downstream of the outlets is a mixture with both fine air bubbles and water to reduce the friction.
2. **Transitional Air Layer Drag Reduction** (TALDR)
   As air volume flow is increased, it is found that the flow regime changes and sheet flow starts to develop. This type of flow is characterised by both bubbly and stratified, i.e., the hull is covered by interwoven regions of bubbly flow and segments of the air layer. In other words, it is representative of the transition from bubbly flow to that of a continuous air layer.
3. **Air Layer Drag Reduction** (ALDR)
   This is the same as BDR except that a continuous jet of air is generated by the air injection system.
4. **Partial Cavity Drag Reduction** (PCDR)
   This method is similar to ALDR except that it uses a thick groove filled with air to form a deeper cavity under the hull and separate it from water. PCDR refers to partial coverage of the hull bottom by the cavity.

The conceptual differences between these drag reduction methods are illustrated in Figure 1.1.

BDR, TLDR, and ALDR can be considered to be related to each other since they can all be achieved using the same configuration of the flat surface, as shown in Figure 1.1a. However, to progress from BDR to TALDR, and finally to ALDR, the air flux must be increased, as demonstrated by Elbing et al. (2008). These three techniques have been categorised based on the resultant % drag reduction (% DR), i.e., below 20% for BDR, from 20% to 80% for TALDR, and finally greater than 80% for ALDR, as shown in Figure 2.6.

On the other hand, PCDR, also referred to as the *air chamber concept*, requires a cavitator to separate the mean flow in the upstream region to form *external* cavities but also requires a recess in the hull bottom with a beach enclosure to form *internal* cavities. The cavitator is an obstruction in the span-wise direction that creates a suction pressure immediately downstream of it. Cavities can be generated only for non-zero flow velocity and have a limited maximum length for a specific velocity and depth. This is approximately equal to half the wavelength of the gravity-dominated surface wave (Zverkhovskyi, 2014), as given by Equation (1.4).

$$L_{\text{cavity, max}} \approx \frac{\lambda}{2} \tag{1.4}$$

As explained by Rotte et al. (2016), the free surface of the internal cavity is not limited by the wavelength of the gravity-dominated surface wave when the recess is of sufficient depth. Thus, a multi-wave cavity can be formed, which is not possible with external cavities. Both the internal and external cavities needs side fences to remain stable.

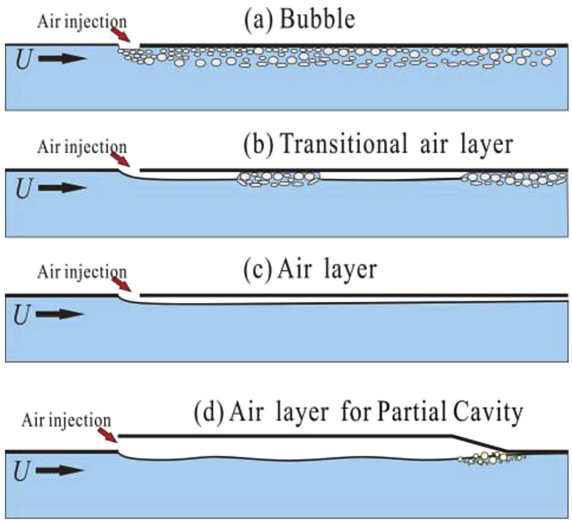


(a) From top to bottom: BDR, TALDR, ALDR, (multi-wave) internal PCDR (Hao et al., 2019)

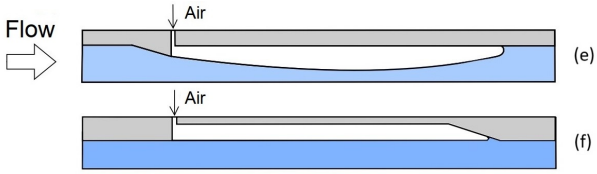


(b) External and (single-wave) internal PCDR. (Zverkhovskyi, 2014)

Figure 1.1: Conceptual sketches of ADR techniques

## 1.3 Scope

Among the techniques mentioned above, BDR, TALDR, and ALDR require the least amount of modification to the hull. Further, among these three techniques, ALDR has a proven maximum capacity for (local) drag reduction in excess of 80% (Sanders et al., 2006), thus making it the most attractive ADR technique. However, since ALDR is achieved after BDR and TALDR, this work aims to experimentally investigate the effect of bubbles, an intermittent air layer, and a continuous air layer formed under a horizontal flat plate on the total drag at the air-water interface. Specifically, the influence over a range of air bubble/layer conditions defined by a free-stream velocity and volumetric air flux were studied, with the intention to measure the total drag acting on the plate and analyse the drag reduction behaviour in terms of the associated non-wetted area generated by air. This study deals with freshwater devoid of impurities and surfactants in the free-stream flow. Experimental methods were used as they are considered the most reliable and accurate tools in investigating the associated two-phase flow.

## 1.4 Outline

Chapter 1 discusses first a motivation and the theoretical background of the present study. Then, a brief description of the objective and scope of the study is given.

Chapter 2 reviews relevant studies conducted on drag reduction achieved by the use of air/gas. Knowledge gaps derived from the cited literature, which form the basis of the present work, are also introduced here. Furthermore, it enumerates the research objectives that arise from this literature study. The research questions and sub-questions formulated to help achieve the said objectives are also discussed here.

Chapter 3 provides the main details of the experimental setup used in this study: from the pre-existing facilities to newly designed components and employed devices.

Chapter 4 describes the sequential procedure followed to obtain experimental data and process it obtain the desired parameters.

Chapter 5 gives an account on the uncertainty associated with the measurements taken as part of this work.

The results from the current work are presented in Chapter 6. A comparison with the most relevant studies from existing literature is also made to identify potential agreements and highlight how the present study differs from them.

Chapter 7 summarises the key findings from the present work and reflects on possible improvements and scope for further research.

# 2

# Literature Review

*This chapter reviews relevant studies that form the basis for the present work. Section 2.1 summarises the fundamental concepts of turbulent boundary layer theory. Section 2.2 discusses previous studies conducted on BDR whereas and Section 2.3 discusses the same on TALDR and ALDR. Moreover, Section 2.4 describes a PCDR study conducted under experimental conditions very similar to those pre-defined by the testing facility where experiments for the present study will be carried out. Section 2.5 summarises the experimental techniques and instruments that have been used in cited literature and leads into the possibilities for measurement in the present work. Finally, the research objectives of the present work are explained in Section 2.6*

## 2.1 Turbulent Boundary Layer

As measurements were conducted under turbulent boundary layer (TBL) conditions, it is crucial to understand the fundamental physics of this flow. The motion of an object through a fluid or that of a fluid past an object causes disturbance among the molecules of the fluid near the object. A thin layer of fluid near the surface of the object in which fluid velocity changes from zero at the surface to the free-stream velocity farther away from the surface is called a boundary layer. Such a layer characterised by eddies and large exchange of mass, momentum and energy between adjacent layers is categorised as turbulent. It is associated with high $Re$. The parameters that characterise a TBL with zero pressure gradient (ZPD), i.e., thin flat plate, originating from the plate's leading edge are given below (Sclichting, 1979):

1. **Local Wall Shear Stress**
   The wall shear stress $\tau_w$, is related to momentum thickness $\theta$ and free-stream velocity as in Equation (2.1). This is a local parameter because it varies with $x$, the downstream distance from the leading edge of the plate.

$$\tau_w = \rho U_\infty^2 \frac{\mathrm{d}\theta}{\mathrm{d}x} \tag{2.1}$$

2. **Velocity Profile**
   Considering the assumption that the velocity distribution in the boundary layer on a plate obeys a $\frac{1}{7}^{\text{th}}$ power law,

$$\frac{u}{U_\infty} \approx \left(\frac{y}{\delta}\right)^{1/7} \tag{2.2}$$

   Thus, the local velocity varies with the boundary layer thickness $\delta$.

3. **Momentum Thickness**
   Applying the $\frac{1}{7}^{\text{th}}$ power law to establish the dependence of momentum thickness on boundary layer thickness $\delta$,

$$\theta \approx \int_0^\delta \frac{u}{U}\left[1 - \frac{u}{U}\right] \mathrm{d}y \tag{2.3}$$

From Equation (2.2),

$$\theta \approx \frac{7}{72}\delta \tag{2.4}$$

4. **Boundary Layer Thickness**
From Prandtl's empirical formula for local wall shear stress proposed in 1927,

$$\tau_w = 0.0225\rho U_\infty^2 \left(\frac{\nu}{U_\infty \delta}\right)^{1/4} \tag{2.5}$$

From Equation (2.1) and Equation (2.4),

$$\rho U_\infty^2 \frac{\mathrm{d}\theta}{\mathrm{d}x} \approx \rho U_\infty^2 \frac{\mathrm{d}}{\mathrm{d}x}\left(\frac{7}{72}\delta\right)$$

Upon cancelling $\rho U_\infty^2$ and rearranging terms,

$$\delta^{1/4}\mathrm{d}\delta \approx 0.2314\left(\frac{\nu}{U_\infty}\right)^{1/4}\mathrm{d}x$$

Upon integration on both sides,

$$\frac{4}{5}\delta^{5/4} \approx 0.2314\left(\frac{\nu}{U_\infty}\right)^{1/4} x$$

Therefore,

$$\delta \approx 0.37\left(\frac{\nu}{U_\infty}\right)^{1/5} x^{4/5} \tag{2.6}$$

Or,

$$\frac{\delta}{x} \approx \frac{0.37}{Re_x^{1/5}} \tag{2.7}$$

where $Re_x$ represents the Reynolds number based on $x$.

5. **Local Friction Coefficient**
The corresponding skin friction is given by Equation (2.8).

$$c_f' = \frac{\tau_w}{\frac{1}{2}\rho U_\infty^2} \tag{2.8}$$

From Equation (2.5) andEquation (2.6),

$$c_f' \approx \frac{2 \times 0.0225}{(0.37)^{1/4}}\left(\frac{\nu}{xU_\infty}\right)^{1/5}$$

Thus,

$$c_f' \approx 0.0576 Re_x^{-1/5} \tag{2.9}$$

6. **Friction Coefficient**
By definition,

$$C_F = \frac{1}{l}\int_0^l c_f' dx \tag{2.10}$$

After substituting Equation (2.9) in Equation (2.10), the *Prandtl formula* is obtained as

$$C_F = 0.074 Re^{-1/5} \quad \forall \quad 5 \times 10^5 < Re < 10^7 \tag{2.11}$$

where $Re = U_\infty l/\nu$ is Reynolds number based on plate length $l$. Equation (2.11) is an exact theoretical representation of the turbulent friction drag. However, when compared with experimental data, it is found to be only ±25% accurate. A number of other empirical and semi-empirical turbulent skin-friction coefficient relations have also been developed, some of which are considerably more accurate than the Prandtl formula (Bertin and Cummings, 2009).

- *Karman-Schoenherr*
  ±2% accurate

$$\frac{1}{\sqrt{C_F}} = 4.13 \log_{10}(Re \cdot C_F) \tag{2.12}$$

- *Prandtl-Schlichting (Sclichting, 1979)*
  *±3% accurate*

$$c_f' = (2\log_{10} Re_x - 0.65)^{-2.3} \tag{2.13}$$

$$C_F = \frac{0.455}{(\log_{10} Re)^{2.58}} \quad \forall \quad Re \leq 10^9 \tag{2.14}$$

- *Schultz-Grunow*
  *(±7% accurate)*

$$C_F = \frac{0.427}{(\log_{10} Re - 0.407)^{2.64}} \quad \forall \quad 10^6 \leq Re \leq 10^9 \tag{2.15}$$

While the Karman-Schoenherr relation is the most accurate of these relationships, it requires an iterative solution method to obtain a result, since $C_F$ is not explicitly represented. Therefore, the most accurate relation which is also straight-forward to use is Equation (2.14).

Additionally, two more algebraic approximations for $C_F$ are known for a flat plate. These are the friction lines proposed by Grigson (1992) and Katsui et al. (2005), as given by Equation (2.16) and Equation (2.17), respectively.

$$C_F = \left[0.93 + 0.1377\left(\log_{10} Re - 6.3\right)^2 - 0.06334\left(\log_{10} Re - 6.3\right)^4\right] \frac{0.075}{\left(\log_{10} Re - 2\right)^2} \quad \forall \quad 1.5 \times 10^6 < Re < 2 \times 10^7 \tag{2.16}$$

$$C_F = \frac{0.0066577}{\left(\log_{10} Re - 4.3762\right)^{(0.042612 \log_{10} Re + 0.56725)}} \quad \forall \quad 10^6 \leq Re \leq 10^9 \tag{2.17}$$

7. **Drag Coefficient**
   Since a thin flat plate exhibits 100% friction drag and no pressure drag (White, 2016), the drag coefficient $C_D$ defined as $C_D = C_{D,\text{friction}} + C_{D,\text{pressure}}$ is equal to $C_F$. Thus, in the context of a thin flat plate, the terms friction coefficient and drag coefficient may be used interchangeably.
8. **Friction Drag**
   From the distribution of the wall shear stress $\tau(x)$, the friction drag $D$ can be easily computed by integration over the surface of the plate (Schlichting, 2017). The drag due to friction acting on the bottom face of a flat plate with a wetted surface area $A$ is

$$D = b \int_0^l \tau_w \mathrm{d}x \tag{2.18}$$

$$D = C_F \cdot \left(\frac{1}{2}\rho U_\infty^2\right) \cdot A \tag{2.19}$$

## 2.2 Bubble Drag Reduction

Preliminary experiments conducted on a *fully-submerged body of revolution* by McCormick and Bhattacharya (1973) confirmed the drag-reducing ability of hydrogen micro-bubbles (smaller than the inner scales of turbulent flow) generated by *electrolysis*. They studied the effects of variable power supply for Reynolds numbers between 0.3 and 1.8 million by using different combinations of current and voltage.

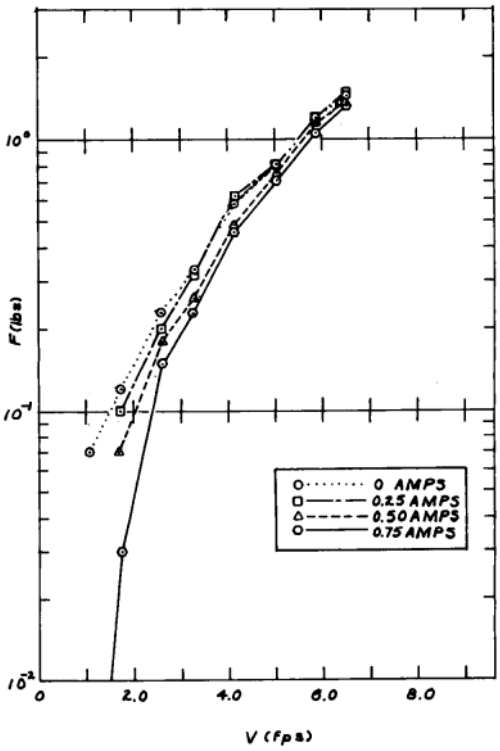


(a) Total drag versus towing speed for Configuration 5.
The case with 0 amps is representative of a no-bubble situation
(McCormick and Bhattacharya, 1973)

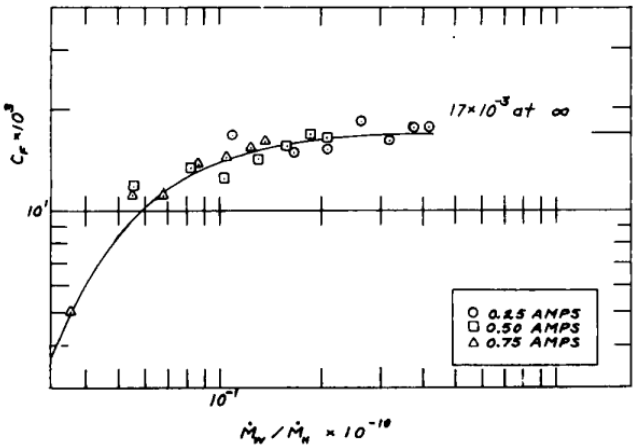


(b) Skin friction coefficient versus $H_2$ mass production rate obtained with Configuration 5 (McCormick and Bhattacharya, 1973)

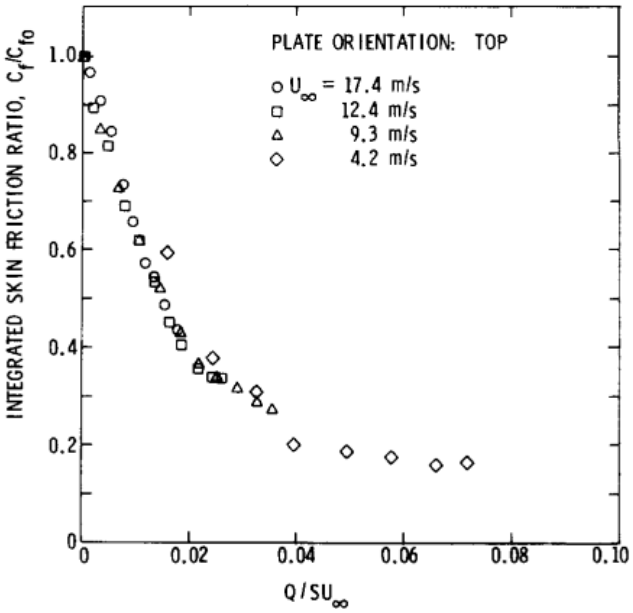


(c) Dimensionless skin friction as a function of dimensionless injection rate. $C_{f0}$ denotes skin friction without bubbles.
(Madavan et al., 1984)

Figure 2.1: BDR results from a few initial studies

Upon measuring total drag by a force dynamometer, they observed that the amount of drag reduction was maximum at the lowest towing speeds and decreased as the speed increased, as shown in Figure 2.1a. Nevertheless, a clear physical justification for this behaviour was not given. In addition, the magnitude of drag also varied with the applied current. These trends indicated that the amount of drag reduction depends on the *towing speed* and the *time-rate of hydrogen mass production*, the latter being proportional to the applied current. Here, the hydrogen mass production indicates the amount of gas used to form micro-bubbles. Therefore, $C_F$ was expressed as a function of a single parameter: the ratio of the mass flow of water in the wake of the hull ($\dot{M}_W$) to the rate of hydrogen mass produced by electrolysis ($\dot{M}_H$). By doing so, it became evident that drag reduction resulted from the creation of hydrogen gas beneath the boundary layer. In Figure 2.1b, this is indicated by a decreasing trend in $C_F$ as $\dot{M}_H$ increases. Finally, the authors noted that when the flow in

the boundary layer is turbulent, i.e., when the length-based Reynolds number, $Re > 6 \times 10^5$, the micro-bubbles lead to a decrease in the turbulent stresses by absorbing momentum with their elasticity, thereby reducing the frictional drag. This study marked the dawn of a technology that could possibly be applied on ships to achieve savings in fuel and emissions.

For $Re$ ranging between 2.2 and 10.6 million, Madavan et al. (1984) examined BDR on a laboratory-scale flat plate (279 mm × 533 mm) in a configuration that allows buoyancy to retain the bubbles in the boundary layer. In these experiments conducted at the Pennsylvania State University, gas was injected through a porous, sintered stainless-steel section and integrated (total) skin friction was strain-gauged tension/compression member. The flow velocity in the water tunnel was determined from a differential pressure transducer, whereas the injected gas flow rates were measured with a turbine flow meter. After achieving maximum skin friction reduction in excess of 80%, the authors reasoned that the integrated skin friction is much lower at the lower tunnel velocities because a given amount of airflow corresponds to a larger volumetric concentration of air in the boundary than at the higher speeds. Therefore, through this study, they added on to the original findings from McCormick and Bhattacharya (1973). Moreover, the authors expressed drag reduction as a function of the dimensionless quantity given by Equation (2.20). This choice implies that this parameter is the ratio of the effective velocity of the incoming air to the tunnel velocity. Figure 2.1c shows that this parameter collapses data into a single curve, indicating a unique skin friction correlation for all tunnel speeds:

$$\frac{Q}{SU_\infty} \tag{2.20}$$

where $Q$ is gas flow rate, $S$ is the wetted surface of the porous section, and $U_\infty$ is the tunnel speed.

Although McCormick and Bhattacharya (1973) and Madavan et al. (1984) established that micro-bubbles can reduce drag in turbulent flow, the bubbles formed from porous plates, which are commonly used in injectors, are frequently much larger, i.e., comparable with the length scales of coherent structures (defined as organised fluid elements of significant scale and life-time). This is because such bubbles are easily and naturally realised in the air–water combination of bubbly flow (Murai, 2014). In this context, Lu et al. (2005) examined the effect of bubbles of a size comparable to the buffer layer in a low-Reynolds number turbulent flow using direct numerical simulation (DNS).

The bubbles investigated in their numerical study are comparable in size (~300 $\mu$m) with those examined in the experimental study by Sanders et al. (2006), which will be discussed later. Lu et al. (2005) showed that deformable bubbles can lead to a significant drag reduction by suppression of stream-wise vorticity because they are able to slide along the wall at the right distance. On the other hand, the less-deformable bubbles are slowed down as they reach into the viscous sublayer and act as obstacles to the liquid flow, thus leading to a large increase in drag. This behaviour can be observed in Figure 2.2, where less deformable bubbles are characterised by a low Weber number and a high mean shear stress. The Weber number $We$ indicates the deformability of the bubbles as expressed in Equation (2.21), where $d_0$ is diameter of bubble, $\rho$ is density of liquid, $\sigma$ is surface tension, $u^* = \sqrt{\frac{\tau_w}{\rho}}$ is friction velocity, and $\tau_w$ is shear stress in arbitrary layer of liquid.

$$We = \frac{\rho d (u^*)^2}{\sigma} \tag{2.21}$$

For the no-bubbles case, the average drag remains approximately constant, but in the case with deformable bubbles there is a significant reduction in the wall drag. The shear stress is non-dimensionalised by the average shear stress for the flow without bubbles. Thus, it can be concluded that deformable bubbles are desirable to achieve drag reduction.

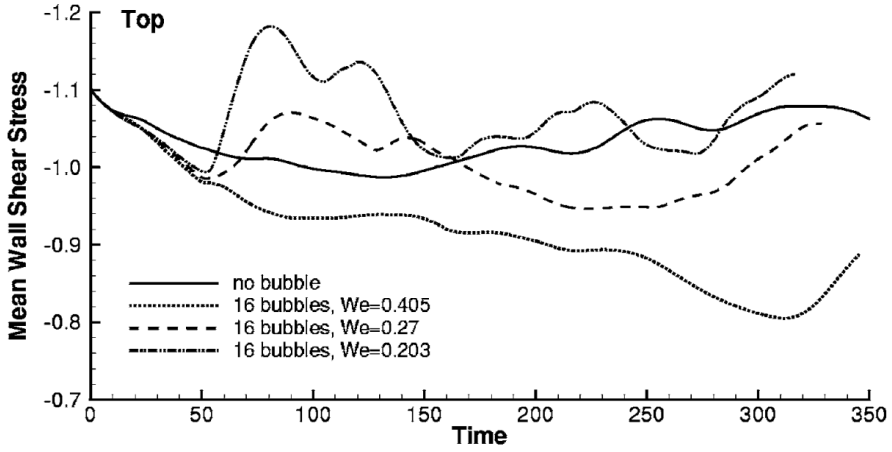


Figure 2.2: Mean wall shear stress acting on the top wall of the minimum turbulent channel versus time for flows with and without bubbles. (Lu et al., 2005)

Later, Sanders et al. (2006) conducted experiments on BDR at $Re_x$ (based on downstream distance) as high as 210 million on a 12.9 m long, and 18.4 cm thick hydraulically smooth (White, 1991) flat plate that spanned a 3 m-wide test section. As shown in Figure 2.3, the shear stress sensors were located 50.8 cm from the centre span. The inlet flow speeds were monitored by a single-component laser Doppler velocimeter (LDV). The bubble camera was located 77.5 cm from the centre span. The stream-wise locations of the instrumentation are indicated relative to the leading edge of the model at $x = 0$. The observation windows were centred at $x = 1.96$ m, 5.94 m, and 10.68 m. The model was oriented with the test-surface facing downward during the experiment so that gravitational buoyancy forced bubbles toward the test surface. The tests were carried out in the USA Navy's Large Cavitation Channel (LCC).

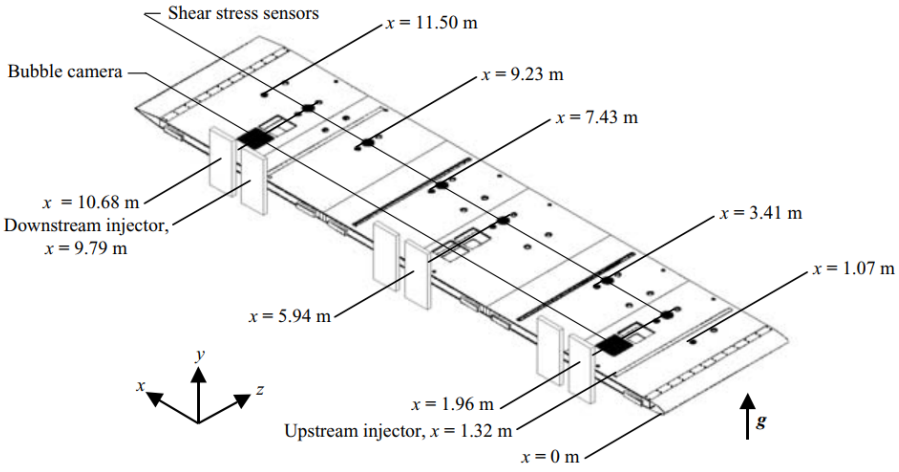


Figure 2.3: Schematic diagram of the test model.
For clarity, the model is presented with the test surface facing upward.
(Sanders et al., 2006)

With a mean bubble diameter of ~300 $\mu$m, the authors showed that significant levels of BDR could be achieved near the location of the porous-plate-type injector. Interestingly, they also observed that the largest non-wetted area ratio (18 m s$^{-1}$ with UI at $x = 1.96$ m) does not correspond to the case of the greatest drag reduction (see Figure 2.4). Here, $A_b$ is the area of the imaged section covered by focused bubbles and $A_{total}$ is the total area of the imaged section for $U_\infty$ from 12 and 18 m s$^{-1}$. The authors suggested a reason for this: drag reduction is driven by the *combination* of *large void fraction* with *small bubbles* in *close proximity* to the flat plate. In other

words, for optimal drag reduction, smaller bubbles resulting in a large void fraction must be ideally present near the test surface of the flat plate. However, for the range of bubble sizes generated in their experiments, the authors found that abundance and proximity of the bubbles to the test surface was more important than the bubble size in producing significant BDR.

On the other hand, limited persistence of BDR beyond 2 m from the injection location was observed, owing to bubble migration from the plate surface induced by near-wall shear. Therefore, it was concluded that such a short persistence distance deems BDR impractical for the application to ships as it would demand many injection locations and large volume fluxes of gas. This triggered investigation into alternative drag reduction (TALDR and ALDR) techniques with a persistence distance extending up to the full length of the flat plate and a similarly high drag reduction performance. These were inadvertently realised in the same study at lower flow speeds and higher gas injection rates. An explanation of these findings is given in Section 2.3.

Here, it is important to note that in contrast to the previously discussed experimental studies, the drag measurements made by Sanders et al. (2006) using shear stress sensors are specific to certain locations along the flat plate, i.e., *local*, and vary across the plate as there may be local regions where drag increases significantly or reduces only by a relatively small amount. This distinction is crucial because changes in a local region may have both localised and more widespread effects on the overall drag. Thus, for the assessment of overall drag reduction performance, it can be said that total drag is a better measurement parameter than local drag.

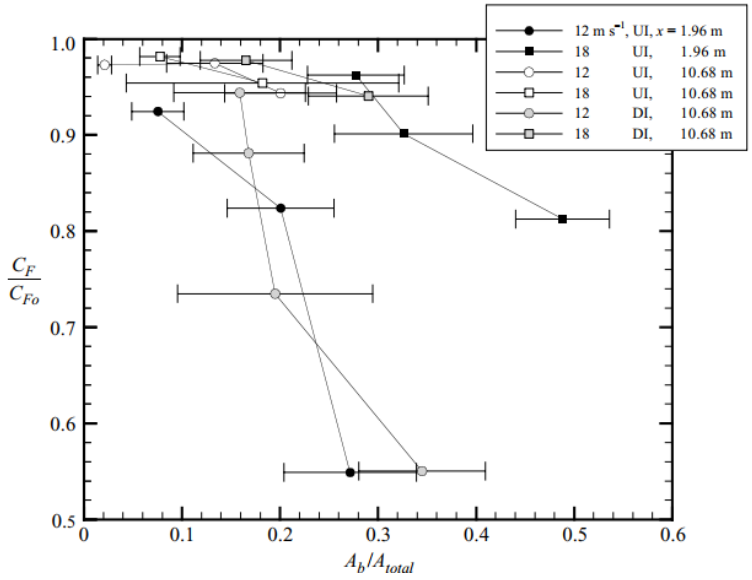


Figure 2.4: Measured skin friction ratio versus non-wetted area ratio.
UI = upstream air injection at $x$ = 1.32 m; DI = downstream air injection at $x$ = 9.79 m.
(Sanders et al., 2006)

Although BDR may not be a viable option for ships, numerous other technical papers have been reported on this subject by fluid engineering researchers. A schematic characterisation of such reports published until 2014 was plotted in a review article by Murai (2014) clearly depicting the domain of flow speed and bubble size explored. As indicated in Figure 2.5, three distinct regions were identified: the first representing the domain where increase in friction was observed, despite a drop in the mixture density of the boundary layer, the second where drag reduction was achieved, and the last representing a domain where the bubbles become unstable and cannot maintain their initial size owing to shear stress. He also noted that the unstable region occurs only in the transition from small to large bubbles for coalescence (at high void fraction) or from large to small bubbles (for fragmentation). From this, it can be inferred that the unfavourable regions must be avoided to realise BDR.

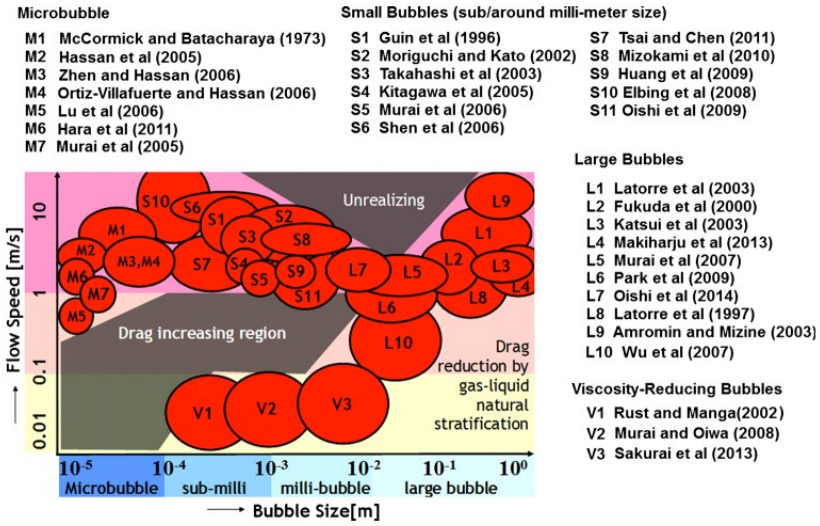


Figure 2.5: Flow speed versus bubble size
(Murai, 2014)

More recently, Zhao and Zong (2023) provided a justification for total drag increase observed in the presence of bubbles as big as 5 mm, based on their numerical study on a model ship for a speed of 0.542 m/s. At low air flow rates and nearly the same void fraction, they found that larger bubbles (5 mm) produce a larger increase in turbulence kinematic viscosity than smaller bubbles (0.5 mm). Then, for insignificant reduction in the mixture density and similar decrease in velocity gradient, the larger bubbles increased shear stress whereas the smaller bubbles decreased it. Thus, they concluded that bubble size influences whether drag reduction occurs or not because it is related to the flow characteristics. In significance, this study adds to the explanations for drag increase observed in the presence of air bubbles.

Overall, it can be summarised that drag increase in the BDR regime, while mainly dependent on bubble size, could arise either from unfavourable proximity of the bubbles to the wall (Lu et al., 2005, Sanders et al., 2006) or the combined effect of increase in effective kinematic viscosity and insignificant decrease in mixture density (Zhao and Zong, 2023). On the other hand, the main positive impact factors for BDR are reduction in turbulent momentum transfer (McCormick and Bhattacharya, 1973), large near-wall void fraction from high concentration of small bubbles (Sanders et al., 2006), and suppression of streamwise vorticity (Lu et al., 2005).

## 2.3 Transitional and Air Layer Drag Reduction

Although few or no experimental investigations have been conducted specifically to investigate ALDR, BDR researchers have inadvertently created and reported some of the characteristics of ALDR.

For example, Madavan et al. (1984) reported a maximum level of drag reduction, in excess of 80 – 90 %, where the increase of gas injection yielded little or no improvement in drag reduction. This was probably associated with the formation of an air layer. Similarly, Sanders et al. (2006) recognised intermittent as well as continuous air layers that were successfully realised in their study primarily aimed at BDR. They reported of both intermittent and continuous gas films that formed underneath a flat plate. The continuous film persisted up to its full length at lower flow speeds and higher gas injection rates, leading to (local) skin friction reduction greater than 80%. However, air layers were observed for only a limited number of flow conditions with the same test model as in Section 2.2, since examination of this phenomenon was not the principal goal of their study.

Following up on the above observations, Elbing et al. (2008) continued the study of BDR and ALDR using the same test model in an effort to understand the mechanisms underlying the limited persistence of BDR and the

onset conditions for ALDR. For this, the free-stream liquid velocity, $U_\infty$, (6.7 to 20 m s$^{-1}$), gas injection rate (2.83 to 22.7 m$^3$ min$^{-1}$), injection location, and injector type (porous-plate or slot) were varied. The physical size of the bubbles observed ranged from approximately 25 to 1000 $\mu$m. Local drag measurements were made by six force balances at their respective stream-wise locations. The schematic of the test model's working surface is the same as in Figure 2.3. The authors examined the transition from BDR to ALDR carefully at location, $X - X_{inj} = 6.05$ m. Here, three distinct regimes were apparent and identified as in Figure 2.6a with % DR versus $q$, the volumetric gas injection rate per unit span. *Region I* represents a BDR regime where drag reduction is nearly linear with gas injection, whereas *Region II* represents a transitional region with a much steeper slope. Lastly, *Region III* is an ALDR regime where a maximum level of drag reduction is achieved. Additionally, two gas injection-rate thresholds are defined; a transition threshold, $q_{trans}$, and a critical gas injection rate for ALDR, $q_{crit}$. These gas injection rates are located at the break point (abrupt slope change) between regions I and II ($q_{trans}$) and between regions II and III ($q_{crit}$), as seen in the same figure. They also found that the gas injection-rate thresholds were strongly influenced by $U_\infty$. This dependence is shown in Figure 2.6b. The two curves define the boundaries for the transition across three drag reduction regions: I, BDR; II, TALDR; and III, ALDR.

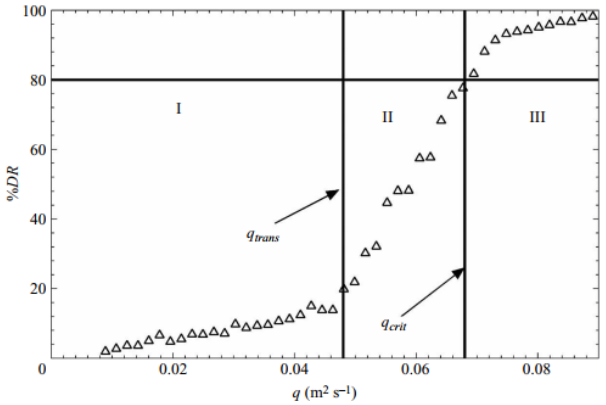


(a) % (local) drag reduction versus volumetric gas injection rate per unit span for the porous-plate injector at 11.1 m s$^{-1}$ and $X - X_{inj} = 6.05$ m (Elbing et al., 2008)

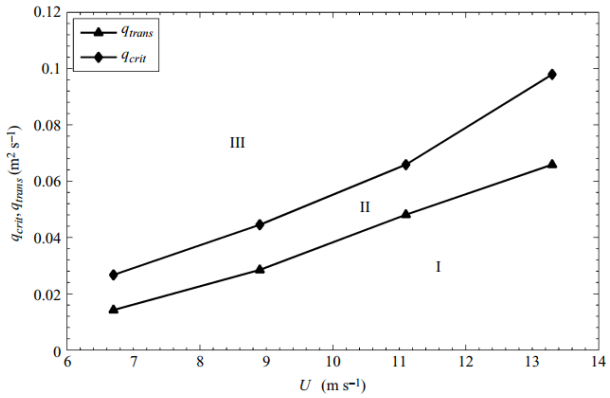


(b) Transition gas injection rate, $q_{trans}$ and critical gas injection rate, $q_{crit}$ versus free-stream speed for the porous-plate injector. (Elbing et al., 2008)

Figure 2.6: Drag reduction and key injection rates corresponding to the three regimes of BDR, TALDR, and ALDR

Additionally, they performed integrated drag measurements to study the sensitivity to the inlet condition (porous-plate versus slot) on a slightly modified configuration by adding a 1-cm backward-facing step at the injector. To accomplish this integrated skin-friction measurement, precision rails and linear bearings were used to affix the model skin to the body of the model. Each of the six sections was instrumented with force transducers/load cells to measure the total frictional force on the respective section. After experiencing unintentional disturbances in the test model due to in situ repairs, they noted that the TBL upstream of an air layer should be free of large-scale non-uniformities and that a small step can provide a clean flow separation line for the air layer, even if the incoming TBL is not uniform. Although air layers were reported to have been formed, data on % DR achieved in this configuration were not provided.

More recently, Nikolaidou et al. (2021) provided an alternative definition for the identification of the different air-layer regimes based on the distribution of wetted/non-wetted areas. For this, experiments were performed in the water tunnel of the Laboratory for Aero & Hydrodynamics of Delft University of Technology. After capturing the images of the different air layer regimes with an imaging camera, they found that for a given $U_\infty$, initially, increasing air flow rate results in increased non-wetted area. Then, further increase in air flow rate results in an abrupt increase of non-wetted area. Even further increase in air flow rate led to a decrease in non-wetted area. While the maximum non-wetted area was observed in the transitional regime for all the

low velocities, this effect seemed to diminish with increasing free-stream velocities. This is evident from Figure 2.7a. They also found that the extent of the non-wetted area increases with increasing air flow rate in BDR and TALDR but remains almost independent of the air flow rate in ALDR. This behaviour is shown in Figure 2.7b.

Here, it is worth noting that since Elbing et al. (2008) obtained three different regimes of air by increasing the gas injection rate that correspond to different ranges of drag reduction and Nikolaidou et al. (2021) observed changes in the non-wetted area of the plate with increasing gas injection rate while still achieving the same three regimes, a correlation is likely to exist between non-wetted area and drag reduction achieved.

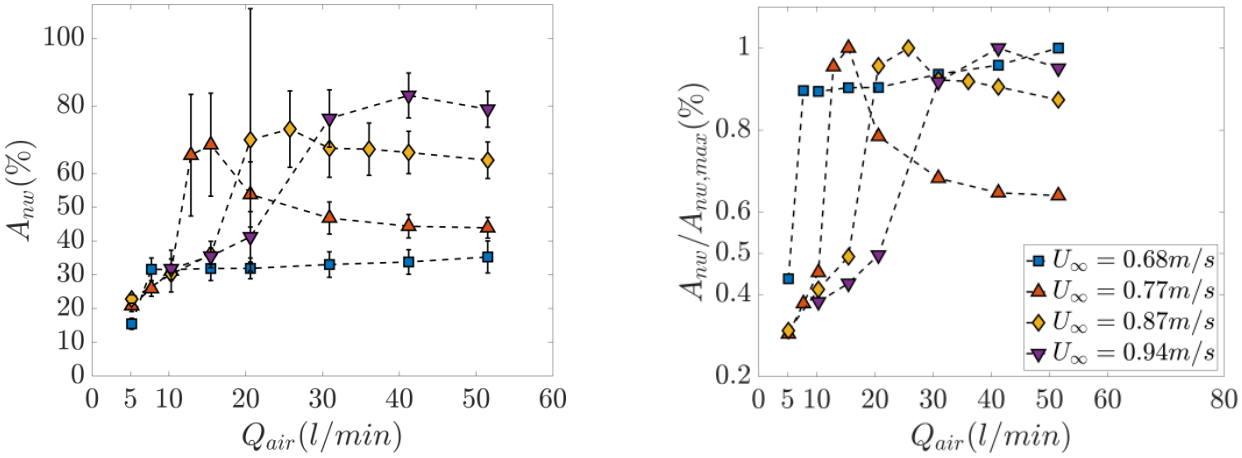


(a) Percentage of non-wetted area versus air flow rate

(b) Normalised percentage of non-wetted area versus air flow rate

Figure 2.7: Non-wetted area and normalised non-wetted area versus air flow rate (Nikolaidou et al., 2021)

Later, at the same test facility, Nikolaidou et al. (2022) investigated the effect of different incoming flow characteristics on the air layer's geometry by varying both $U_\infty$(0.68 to 0.96 m/s) and the stream-wise development length of the TBL (1.45 and 3.95 m). For this study, air was injected underneath a two-plate setup through a slot-type injector of length 4 mm. The incoming boundary layer as well as the flow around the air layer were measured with planar particle image velocimetry (PIV). The authors observed that increasing the $U_\infty$ resulted in an increase of the air layer length, while its maximum thickness remained relatively unaltered (within the experimental uncertainty of 2 mm). This behaviour is depicted in Figure 2.8.

Although this study did not investigate drag, the increasing trend in the air layer's length is of importance. Since non-wetted area is obtained from the product of the length and width of the air layer, this relationship could possibly impact the correlation that is likely to exist between non-wetted area and drag reduction suggested earlier.

## 2.4 Partial Cavity Drag Reduction

Zverkhovskyi (2014) conducted a parameter study on PCDR applied to the lower surface of a flat plate with an area of 2000 × 298 mm$^2$ for flow velocities from 0.9 to 2.8 m/s and air flow rates between 0.24 and 12 l/min. The experiments were carried out in the cavitation tunnel at the Ship Hydromechanics group of Delft University of Technology. Although this study did not employ ALDR, it is still considered relevant owing to the elaborate explanation on other important aspects of the research such as drag reduction measurement and uncertainty analysis.

To measure the (total) drag acting on the flat plate, a custom-made force balance as shown in Figure 2.9a was used.

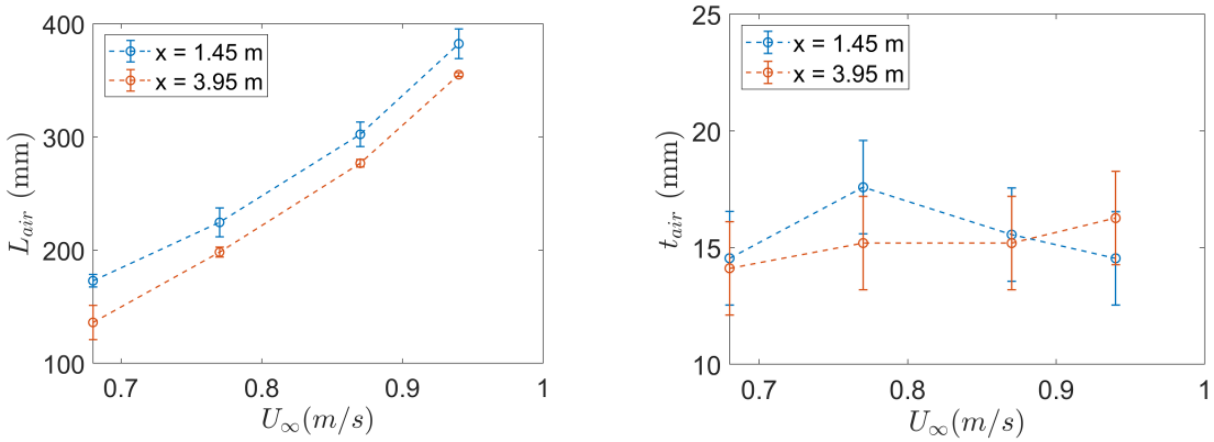


(a) Air-layer length versus free-stream velocity

(b) Maximum air-layer thickness versus free-stream velocity

Figure 2.8: Air-layer length and thickness versus free-stream velocity for two different stream-wise positions, $x = 1.45$m and 3.95 m (Nikolaidou et al., 2022)

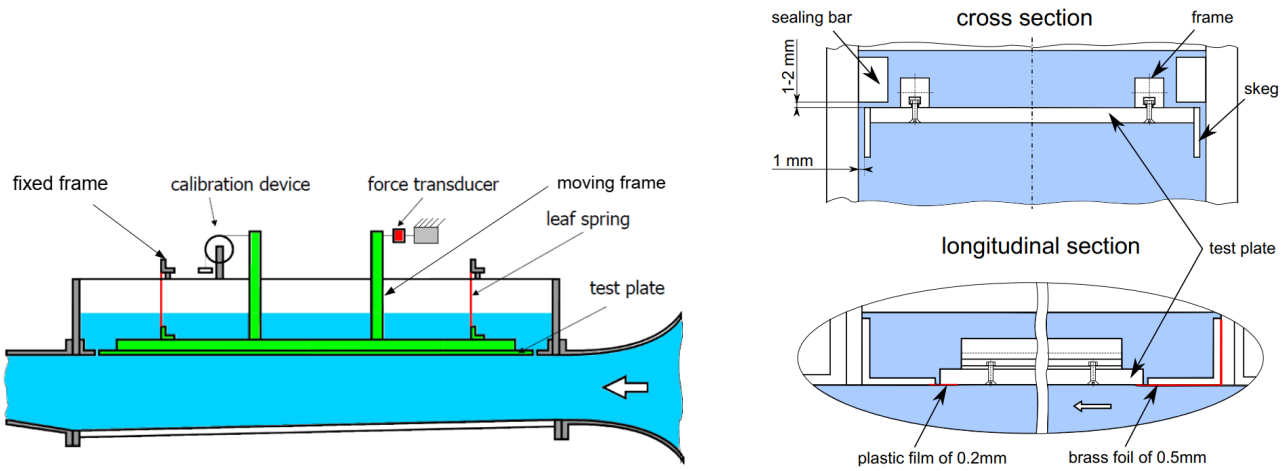


(a) Schematic diagram of the force balance

(b) Schematic of the sealing of the test plate

Figure 2.9: Experimental setup used by (Zverkhovskyi, 2014)

The force balance comprised of a frame that was fixed to the tunnel and a moving frame attached to the flat plate. The two frame were connected to each other by means of leaf springs. However, to ensure that the plate did not touch the fixed frame, small gaps were present between the plate and the walls of the test section. These slots, if not kept small and sealed, may disturb the flow at the front and rear edges of the plate as well as cause flow above the plate. These effects may result in unwanted influence on the force measurement on the lower side of the test plate. Therefore, to avoid or minimise these effects, the gaps around the plate are kept small and sealed; the front and rear edges are overlapped with a thin brass plate and plastic foil respectively, as shown in Figure 2.9b. Finally, the contact of the foils with the overlapping surfaces was assumed to be small and not affect the force measurements. This configuration allowed for a free movement of the test plate with the moving frame in the flow direction, but not in other directions.

Furthermore, the moving frame was also connected to the strain gauge load cell, which measured the longitudinal displacement induced by the drag force. To avoid additional error in the force measurement that may be caused by vibrations of the tunnel, the load cell was connected from the other side to a construction not connected to the tunnel. The measurement procedure required the balance to be calibrated in situ. This involved conducting an extensive calibration first. Then, for each time the balance was removed from the test

section, a simplified calibration procedure of checking a calibration coefficient by first applying the maximum calibration force and then returning to zero force was done.

Zverkhovskyi (2014) also performed an uncertainty analysis following the guidelines given by International Towing Tank Conference (2002) to estimate the accuracy and uncertainty of the measurements made. This involved consideration of bias and precision errors contributed by each measured parameter to compute the total uncertainty in the estimation of the friction coefficient. However, he noted that for relative drag measurements, the bias uncertainty need not be considered. Finally, by comparing the bias and precision limits and the uncertainties, the relative contribution of each term can be calculated. This makes it possible to determine where an upgrade in the measurement system has the largest effect.

## 2.5 Experimental Techniques and Instrumentation

From Section 2.2 and Section 2.3, it can be said that a diverse range of instruments and equipment can be utilised for drag reduction studies. To help understand the experimental requirements for the present study, an overview of the distinct measurement techniques and devices employed in the literature discussed so far is given in Table 2.1. From this table, it is noticeable that a force balance with strain gauge is commonly applied for drag measurements. On the other hand, for determining air layer length and wetter area, image capture and processing is necessary. The same was adopted for the present study. Since all other parameters could be measured with the pre-existing instruments at the test facility, the available resources were utilised for the present work.

Table 2.1: Distinct experimental techniques & instrumentation employed in previous studies discussed above

| # | Measured Parameter | Measurement Technique / Device |
|---|---|---|
| 1 | free-stream velocity | • differential pressure transducer (Madavan et al., 1984)<br>• laser Doppler velocimeter (Sanders et al., 2006) |
| 2 | volumetric gas flux | • thermal mass flow meter (Elbing et al., 2008)<br>• control valve with mass flow meter (Nikolaidou et al., 2022) |
| 3 | drag (local) | • force balance with strain gauge (Elbing et al., 2008) |
| 4 | drag (total) | • force dynamometer (McCormick and Bhattacharya, 1973)<br>• load cell (Lay et al., 2008)<br>• force balance with strain gauge (Zverkhovskyi, 2014) |
| 5 | air-layer length | • image capture and processing (Nikolaidou et al., 2022) |
| 6 | wetted area | • image capture and processing (Nikolaidou et al., 2022) |

## 2.6 Research Objectives

Following the above literature review on previous ADR experiments, the following key points of interest can be established:

1. **Total Drag Measurement**
   Experiments investigating % DR across all three ALDR regimes predominantly measure *local* drag, which is not constant across the region of interest. This is possible when there may be local regions where drag is altered; for example, where drag increases significantly or reduces only by a relatively small amount. Hence, to assess the drag acting on the entire plate, i.e., not just specific to certain positions along its length, total drag measurements are necessary.
2. **Correlation between Drag and Wetted Area**
   The increasing trends in % DR (Elbing et al., 2008) and non-wetted area (Nikolaidou et al., 2021) when $\dot{Q}_{air}$ is increased suggest that non-wetted area and drag reduction may be correlated.

Therefore, within the interest of low-speed ships, the primary goal of the current research is to develop an experimental setup that can accurately measure the *total* drag acting on a thin flat plate (~2 m × ~0.3 m) at different $Re$ associated with turbulent flow under single-phase and dual-phase conditions. Thereafter, a second objective to assess the reduction in total drag acting on a thin flat plate in three different air flow regimes, namely: bubbles, intermittent air layer, and continuous air layer with the experimental setup follows. Finally, the influence of the so-obtained air morphology on the associated drag reduction shall be investigated based on the plate's non-wetted area.

The objectives of this project give rise to the following main research questions:

*How can the reduction in total drag acting on a flat plate subjected to turbulent flow arising from each of BDR, TALDR, and ALDR be assessed experimentally?*
*How does the morphology of air under the plate influence drag reduction?*

This can be answered through the following sub-questions:

1. **How to design a force balance to experimentally measure the total friction drag on a flat plate?**
2. **How can the drag measurement system be validated?**
   (a) What empirical and semi-empirical formulas can be used for comparison?
   (b) What is the recommended procedure for performing an uncertainty analysis?

   Analogous to previous studies, the regime development and transition shall be studied over increasing volumetric air flux for a given set of free-stream velocities. This is required for determining the boundaries for each regime.
3. **How does drag reduction vary across the three air regimes?**
   (a) What is the maximum drag reduction achieved in each regime?
   (b) Does drag increase in the presence of air in any case? If yes, why?
   This could be answered, for example, based on bubble deformability.
4. **How does the morphology of air under the plate influence drag reduction?**
   This will be assessed in terms of non-wetted area (defined as the area of the plate covered by air).

An overview of the control and measured parameters considered for the present work is given in Table 2.2.

Table 2.2: Overview of parameters considered for present study

| Control Parameters | Measured Parameters |
|---|---|
| • free-stream velocity of water<br>• volumetric flux of air | • total drag on plate<br>• area of plate covered by air layer |

# 3

# Experimental Setup

*This chapter describes the experimental facility and apparatus, including several measurement sensors and imaging equipment employed in the present study. The various aspects considered in the design of the force balance are explained as well. Finally, the calibration of the load cell selected based on drag estimation is discussed.*

## 3.1 Setup

### 3.1.1 Multi-Phase Flow Tunnel

A cavitation tunnel named *Multi-Phase Flow Tunnel* (MPFT) located at Ship Hydromechanics group of Delft University of Technology served as the experimentation site for this study. A schematic representation of the MPFT is given in Figure 3.1a. As shown in Figure 3.1b, this facility features a test section with a decreasing cross-sectional area to allow uniform flow of water across its length from inlet to outlet. The water velocity is set by the rotational frequency of a RIM drive pump. Within the interest of air lubrication, the MPFT also features degassers to remove air from the system before the flow completes a loop.

### 3.1.2 Flat Plates

Two flat plates of nearly identical length and width made of polycarbonate were used in this experimental study. The first plate is a conventional flat plate, which was used in single-phase flow experiments to obtain a reference dataset. The second plate, as shown in Figure 3.2, additionally features:

- an air injection system for air lubrication
- a spanwise injection slot (10 mm wide) at a distance of 0.134 m from the leading edge for air outlet
- two vertical fences running across its length along the sides to avoid air escape
- an extension lip at its trailing edge to prevent air from getting stuck at the end of test section
- an LED panel across its length downstream of the injection slot for illumination during image capture

and was used in both single-phase and dual-phase flow for the assessment of drag reduction performance. Hereafter, the first plate shall be referred to as the *conventional plate* and the second plate shall be referred to as the *test plate*. The thickness of these plates was considered to be negligible when compared to their other dimensions. An overview of the dimensions of the two plates is given in Table 3.1.

Moreover, to facilitate free displacement of the plates in the presence of drag, gaps of ~1.5 mm and ~3.5 mm were provided between the plates and the tunnel walls at the upstream and downstream ends, respectively. The gap at the downstream position was kept higher in order to accommodate for the downstream displacement of the plate due to drag. Similarly, gaps between 1 mm and 2 mm were also maintained on either sides of the plates.

Table 3.1: Dimensions of the two plates used

| Parameter | Conventional Plate | Test Plate | Units |
|---|---|---|---|
| $l$ | 1.949 | 1.95 | m |
| $b$ | 0.2935 | 0.2942 | m |
| $h_{\text{fence}}$ | - | 0.049 | m |
| $t_{\text{fence}}$ | - | 0.001 | m |
| $l_{\text{lip}}$ | - | 0.03 | m |
| $t_{\text{lip}}$ | - | 0.001 | m |
| $S$ | 0.5733 | 0.7752 | $m^2$ |

### 3.1.3 Zig-Zag Strip

To ensure that the TBL originates from the same location, a zig-zag strip with a width of 10 mm and thickness of 1.98 mm was placed 0.098 m before the entrance of the test section. This corresponds to an upstream distance of ~ 0.01 m from the leading edge of the test plate.

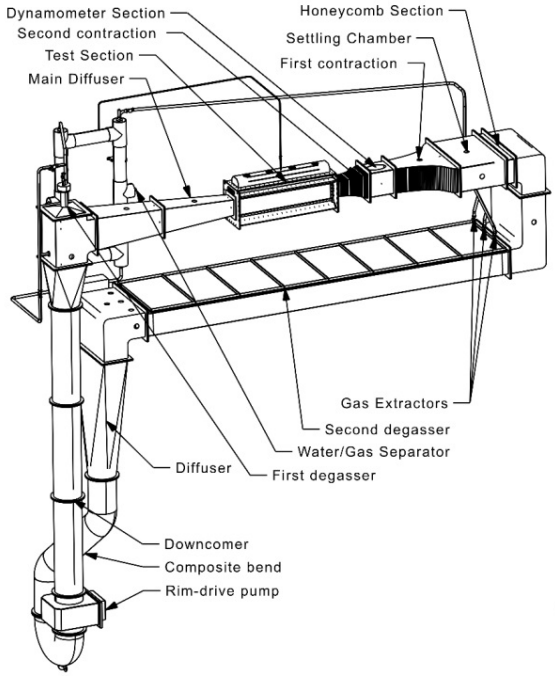


(a) An overview of the architecture circuit of the MPFT, with tags highlighting the different systems and units constituting the cavitation tunnel

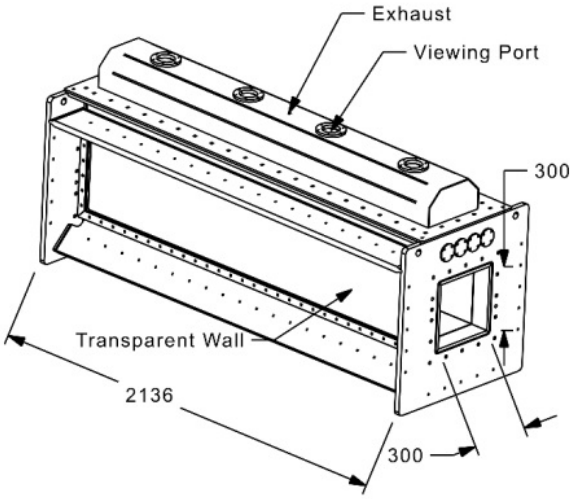


(b) Test section with lid on top

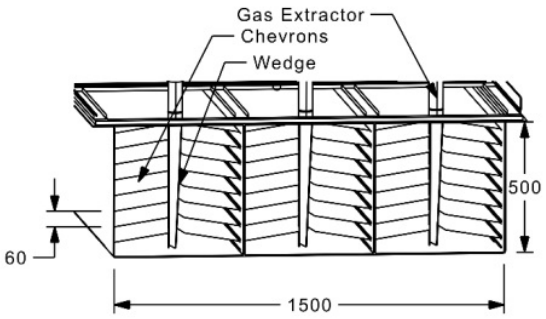


(c) A cross-section at the outlet of the second degasser showing the arrangement of the chevron plates used to remove the bubbles of free non-condensable gas

Figure 3.1: Technical drawings of the MPFT (Fiscaletti et al., 2023)

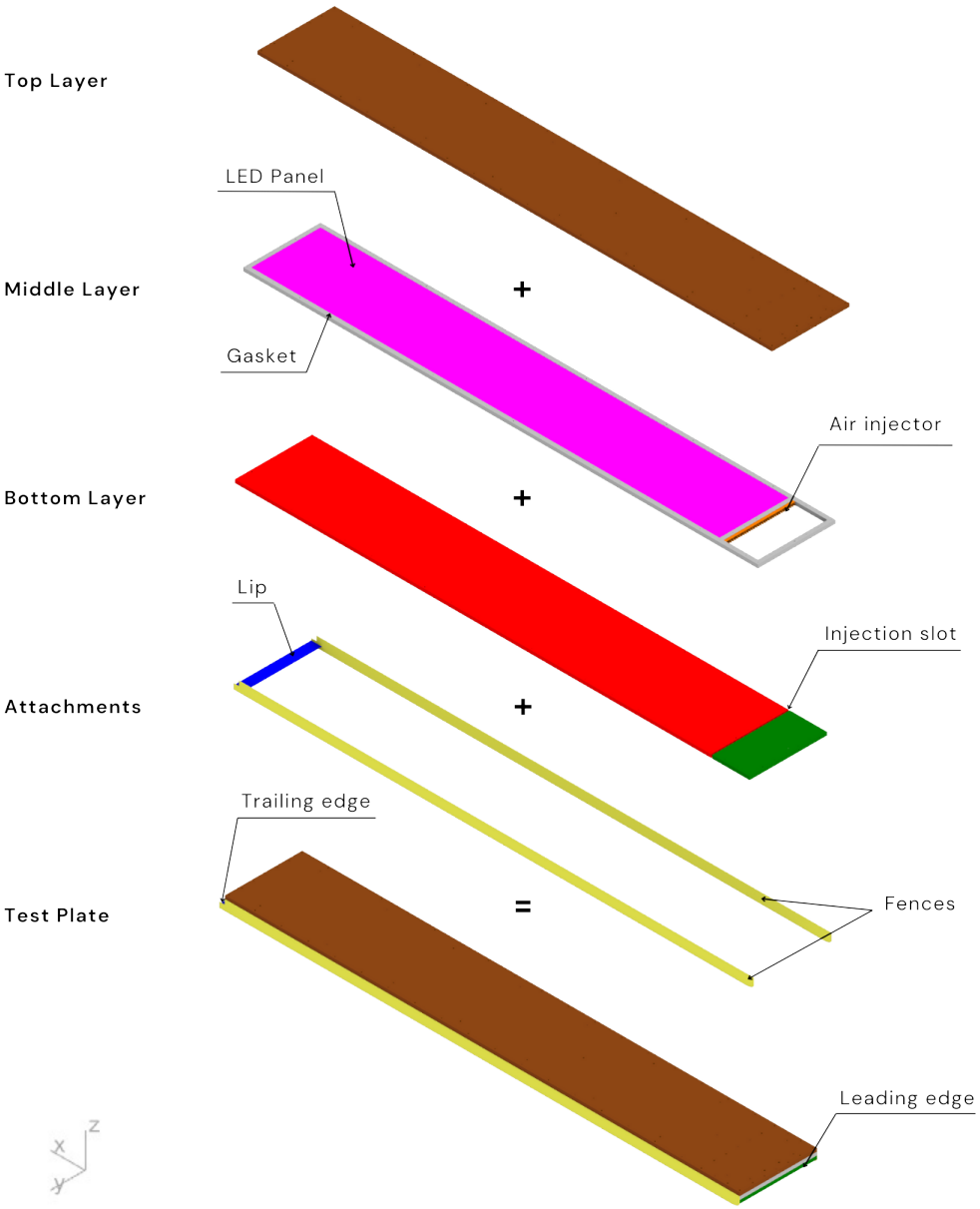


Figure 3.2: Parts of the test plate

### 3.1.4 Sensors

Different sensors were used to read the relevant test parameters during experimentation. These include drag, free-stream velocity, temperature and air flow rate. Data acquisition from these sensors was done through a programming environment called *LabVIEW*.

#### Total Drag

First, drag estimation was required to define the range and resolution of the load cell that could be employed for drag measurement. In this context, drag estimates for a flat plate in single-phase flow are discussed. Then, a comparison of the estimated drag under different levels of air lubrication is given. Different scenarios for when the origin of the TBL starts at or prior to the leading edge were considered because the downstream distance from the origin of the boundary layer influences the wall shear stress, which ultimately determines the resultant drag.

1. **Turbulent boundary layer starts at leading edge**
   Table 3.2 gives the known parameters corresponding to the intended test conditions and the boundary

layer (that would form) under the same. Here, the values for density $\rho$ and viscosity $\nu$ of water were computed based on temperature $T = 18$℃, using approximations given in International Towing Tank Conference (2002). The minimum boundary layer thickness $\delta$ corresponds to the value at 0.1 m downstream of the plate's leading edge (LE), as determined from previously conducted LDV measurements Fiscaletti et al. (2023). Equation (2.19) indicates that for a fixed plate length and width, drag increases

Table 3.2: Intended test conditions

| Parameter | Magnitude | | Units |
|---|---|---|---|
| | Min. | Max. | |
| $T$ | | 18 | ℃ |
| $U_\infty$ | 2.13 | 4 | m/s |
| $\rho$ | | 998.83 | kg/m$^3$ |
| $\nu$ | | $1.054 \times 10^{-6}$ | m$^2$/s |
| $\delta$ (at 5 m/s) | 0.016 | 0.077 | m |
| $l$ | | 2 | m |
| $b$ | | 0.3 | m |
| $h_{fence}$ | | 0.05 | m |
| $t_{fence}$ | | 0.001 | m |

with increasing free-stream velocity. Thus, extreme values of drag can be expected at extreme values of free-stream velocity, i.e., maximum drag at maximum free-stream velocity. The drag obtained using Prandtl-Schlichting's approximation given by Equation (2.14) in single-phase flow is tagged *Case 1* and tabulated in Table 3.3. Similar estimates were made with different friction lines, namely, Grigson, and Katsui. The maximum drag corresponding to the desired velocity range between 2.1 m/s and 4 m/s from among these estimates was taken as reference for the case when the TBL starts at the leading edge of the plate.

2. **Turbulent boundary layer starts upstream of leading edge**
Within the test range of free-stream velocities, it was found that the TBL starts upstream of the leading edge (ULE) of the plate. To quantify this, a computation for the upstream distance $x$ corresponding to the given $\delta$ was made. This was calculated using Equation (2.7), thus leading to the origin of the boundary layer at 0.820 m upstream of the leading edge.

$$x = 0.820 \text{ m} \tag{3.1}$$

As a result of this upstream distance, the (imaginary) characteristic length of the plate is $l + x$. To determine drag using Prandtl-Schlichting's approximation under this condition, the same steps as in the LE scenario were implemented. But, to accommodate the effect of the TBL starting upstream of the leading edge, it was determined as the difference between drag obtained from two cases of different characteristic lengths as defined in Equation (3.2). An overview of the drag acting on the flat plate in the 4 cases discussed so far is given in Table 3.3.

$$D_{l,x} = D_{l+x} - D_x \tag{3.2}$$

where:

$D_{l,x}$ = drag associated with a flat plate of length $l$ and TBL starting at distance $x$ upstream of leading edge *(Case 2)*

$D_{l+x}$ = drag associated with a flat plate of length $l + x$ and TBL starting at leading edge *(Case 3)*

$D_x$ = drag associated with a flat plate of length $x$ and TBL starting at leading edge *(Case 4)*

Upon comparison of *Case 1* and *Case 4*, it can be observed that the drag acting on the flat plate of length $l$ when the boundary layer originates from a point upstream of the leading edge is lower than that when it originates from the leading edge. This phenomenon is a direct result of the fact that the local friction coefficient decreases with increasing downstream distance (Equation (2.13)). When the TBL originates

Table 3.3: Different cases of drag estimated at the intended test conditions in single-phase flow

| Case # | $l$ (m) | $D$ (N) | |
|---|---|---|---|
| | | Min. | Max. |
| 1 | 2.000 | 4.74 | 15.06 |
| 2 | 2.082 | 6.31 | 20.09 |
| 3 | 0.820 | 2.27 | 7.17 |
| 4 | 2.000 | 4.04 | 12.92 |

upstream of the leading edge, the local friction coefficient at the leading edge is lower than that when the TBL starts at the leading edge. Furthermore, as shown in Figure 3.3a, the drag acting on the flat plate with fences is expected to be higher than the estimates made above. This increased drag arises from the 34.68% increased wetted area in the presence of the fences.

As done for single-phase flow, drag estimates were made for the flat plate considering the two scenarios for the origin of the boundary layer. This also involved taking into consideration the increase in wetted surface area originating from the fences. With air lubrication, the drag acting on the test plate was expected to decrease significantly. Drag reduction between 20% and 80% was considered, based on the categorisation made by Elbing et al. (2008). Figure 3.3b shows the estimated drag with 20% and 80% drag reduction. From Figure 3.3, it was concluded that the desirable range of the load cell lies between the interval of 0 and 20 N.

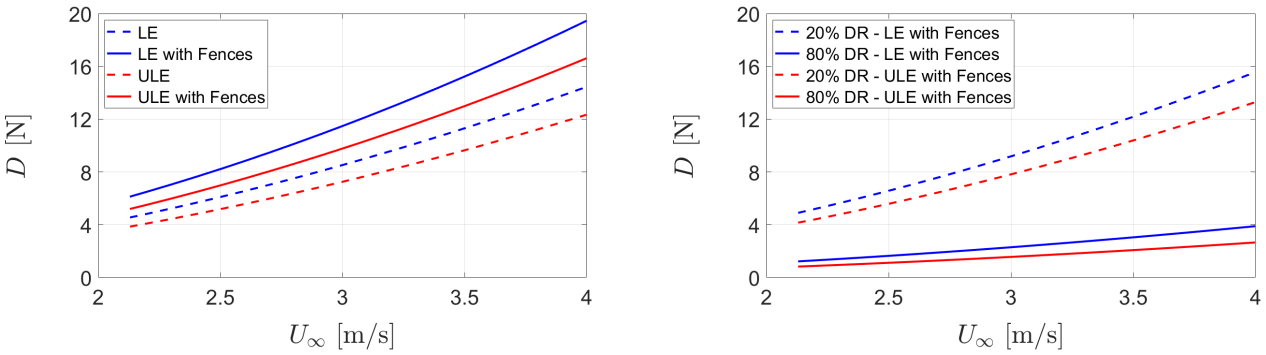


(a) For single-phase flow

(b) For dual phase flow

Figure 3.3: Theoretically estimated drag (based on Prandtl-Schlichting formula) versus free-stream velocity for the intended test conditions

Based on the theoretical estimates for drag resulting under the defined test conditions as discussed above and availability in the market, a stainless steel load cell with IP68 rating, *BM6A* manufactured by ZEMIC®, with a maximum capacity of 6 kg was selected for drag measurement. This load cell was calibrated in-situ after the installation of each plate inside the test section. Owing to the physical limitations of the experimental setup, calibration of the load cell could not be done under conditions exactly representative of the test conditions. During the calibration of the load cell, the test section was not covered with its lid (shown in Figure 3.1b) to facilitate room for the addition or removal of weights to or from the pulley arrangement. Further details about the procedure followed for the calibration of the load cell are given in Section 3.2.

### Temperature

The temperature of water inside the test section was measured with a pre-existing thermometer. The recorded temperature was used to determine the density and viscosity of water according to International Towing Tank

Conference (2006) as given by Equation (3.3) and Equation (3.4), respectively.

$$\rho = 1000.1 + 0.0552 \cdot T - 0.0077 \cdot T^2 + 0.00004 \cdot T^3 \tag{3.3}$$

$$\nu = \left(1.72256 - 0.04765 \cdot T + 0.000585 \cdot T^2\right) 10^{-6} \tag{3.4}$$

### Free-Stream Velocity

A pre-existing differential pressure sensor, *PD-33X* manufactured by KELLER® was used to measure the pressure difference $\Delta p$ across the first contraction. Then, with the application of Bernoulli's principle and equation of continuity, the free-stream velocity at the inlet of the test section was determined using Equation (3.5). This computation was performed by a programme within LabVIEW so that the output signal from the differential pressure sensor displayed free-stream velocity in m/s.

$$U_{\Delta p} = \sqrt{\frac{2 \cdot \Delta p}{\rho \left(1 - \left(\frac{A_1}{A_2}\right)^2\right) \left(\frac{A_0}{A_1}\right)^2}} \tag{3.5}$$

where:

$A_0$ = cross-sectional area at the inlet of the first contraction = 0.735 m$^2$
$A_1$ = cross-sectional area at the inlet of the second contraction = 0.2507 m$^2$
$A_2$ = cross-sectional area at the inlet of the test section = 0.09 m$^2$
$\rho$ = water density based on temperature = $999.796 + 0.0777 \cdot T - 0.0071 \cdot T^2$

Finally, as in Equation (3.6), this velocity was further multiplied with a correction factor of 1.042 determined from previously conducted LDV measurements Fiscaletti et al. (2023) to represent the free-stream velocity at 0.1 m downstream of the test section's inlet.

$$U_\infty = 1.042 \cdot U_{\Delta p} \tag{3.6}$$

### Air Injection Rate

For dual-phase experiments, a pre-existing mass flow controller manufactured by Bronkhorst® with a range between 5 l/min and 500 l/min was used to set the air injection rate.

## 3.1.5 Force Balance

A force balance to facilitate the measurement of drag acting on the plate from the corresponding displacement of the plate was designed based on the concepts of beams, columns, and springs from Beer et al. (2009). Each aspect considered for the design of the force balance is explained in detail further below.

To allow the free movement of the plate in the presence of drag, the plate was suspended freely by means of four vertical rods with a diameter of 5 mm, as shown in Figure 3.4. For convenience, the load cell was mounted at the front section of the plate, with one side fixed to the walls of the tunnel and another side connected to the test plate by means of a horizontal rod of the same diameter. Mounting brackets were fixed on the walls of the test section as well as across the longitudinal C-beams. Altogether, this can be treated as a system of springs attached to the plate. The known parameters used in the design process are given in Table 3.4a and an overview of the stiffness and maximum deflection of this system, as obtained from the design calculations, is given in Table 3.4b.

### Deflection due to drag

When drag acts on the plate, the problem is analogous to the case where the four vertical suspension rods act as cantilever beams, each subjected to a concentrated transverse point load equivalent to the drag at its free end. This translates to a parallel configuration of four springs, where each spring experiences the same deflection. The estimation for deflection in each component of the spring system is discussed below.

Table 3.4: Details of the spring system

(a) Known parameters of the spring system

| Parameter | Numerical Value | Units |
|---|---|---|
| $E$ | 200000 | N/mm$^2$ |
| $d$ | 5 | mm |
| $l_\mathrm{v}$ | 155 | mm |
| $l_\mathrm{h}$ | 430 | mm |
| $D_{\mathrm{sensor,\,max}}$ | 58.86 | N |
| $x_{\mathrm{sensor,\,max}}$ | 1.017 | mm |

(b) Stiffness and maximum deflection of the spring system

| Parameter | Numerical Value | Units |
|---|---|---|
| $k_\mathrm{sensor}$ | 50.31 | N/mm |
| $k_{\mathrm{rod_h}}$ | 9132.54 | N/mm |
| $k_{\mathrm{rod_v}}$ | 50.31 | N/mm |
| $k_\mathrm{res}$ | 69.81 | N/mm |
| $x_{\mathrm{sensor,\,max}}$ | 1.17 | mm |
| $x_{\mathrm{rod_h,\,max}}$ | 9132.54 | mm |
| $x_{\mathrm{rod_v,\,max}}$ | 50.31 | mm |
| $x_{\mathrm{res,\,max}}$ | 0.84 | mm |

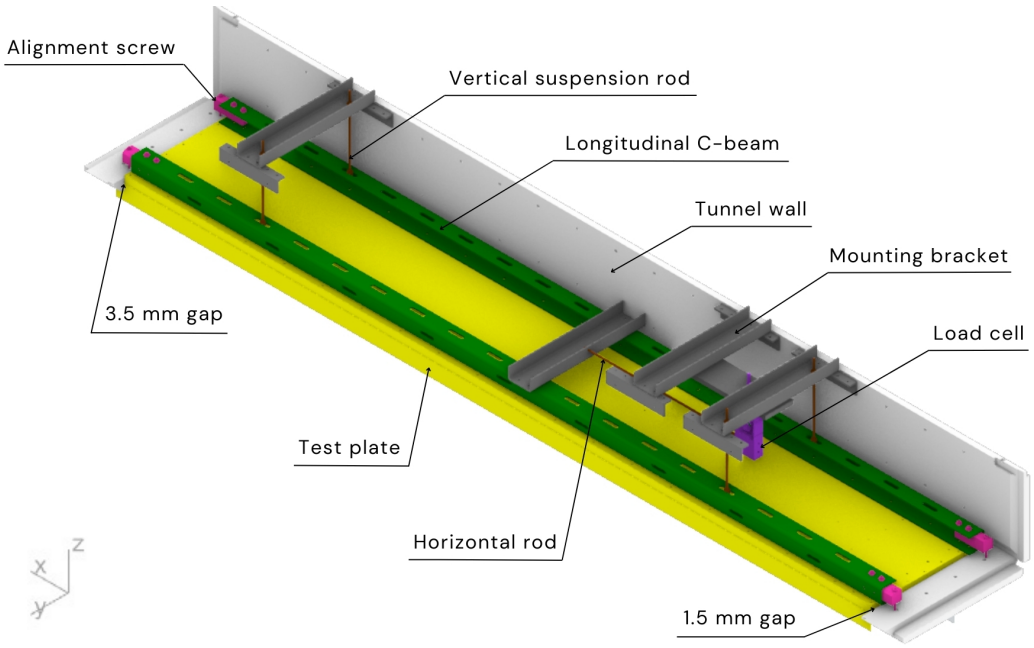


Figure 3.4: Sectional view of the setup inside the test section

**Suspension Rods**

For a single suspension rod, the second moment of area is

$$I = \frac{\pi d^4}{64} = 30.68 \times 10^{-11}\ \mathrm{mm}^4$$

The bending moment resulting from the applied drag is given by

$$M_z = EI\frac{\mathrm{d}^2 x}{\mathrm{d}z^2} = -Dz$$

Considering $z = 0$ and $z = l_v$ at the fixed end and free end of the suspension rod, respectively, successive integration w.r.t $z$ and the application of the boundary conditions at the fixed end yields the relevant deflection equation for the rod. This is given by

$$x = \frac{D}{6EI}\left(-z^3 + 3l_\mathrm{v}^2 z - 2l_\mathrm{v}^3\right) \tag{3.7}$$

The applied boundary conditions are:

$$\frac{\mathrm{d}x}{\mathrm{d}z}\Big|_{z=0} = 0 \qquad\qquad x_{z=0} = 0$$

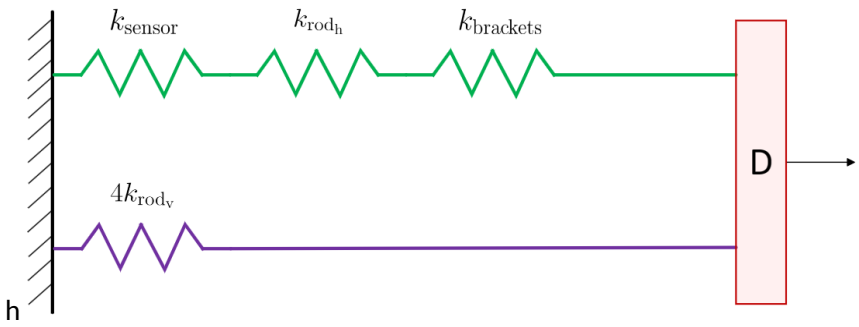


Figure 3.5: Spring System

The deflection at the free end is given by

$$x_{z=0} = -\frac{Dl_v^3}{3EI}$$

The maximum deflection in the suspension rod, i.e., corresponding to $D_{\text{sensor, max}}$ is $x_{\text{rod}_v,\text{max}} = -11.91$ mm. Here, the negative sign indicates the direction of deflection, i.e., downstream.

Then, the stiffness of each suspension rod is

$$k_{\text{rod}_v} = \frac{3EI}{l_v^3} = 4.94 \text{ N/mm} \tag{3.8}$$

**Load Cell**

On the other hand, the stiffness of the load cell is

$$k_{\text{sensor}} = \frac{F_{\text{sensor, max}}}{x_{\text{sensor, max}}} = 50.31 \text{ N/mm} \tag{3.9}$$

**Resultant**

For a spring system comprising all the components shown in Figure 3.5, i.e., the load cell, horizontal rod, and mounting brackets (assumed to be infinitely stiff) on the first arm and the four vertical suspension rods on the second arm:

The stiffness from the first arm is given by

$$\frac{1}{k_1} = \frac{1}{k_{\text{sensor}}} + \frac{1}{k_{\text{rod}_h}} + \frac{1}{k_{\text{brackets}}}$$

which yields $k_1 = 50.03$ N/mm. The stiffness from the second arm is $k_2 = 4k_{\text{rod}_v} = 19.77$ N/mm. Finally, the resultant stiffness from the parallel configuration of $k_1$ and $k_2$ is

$$k_{\text{res}} = k_1 + k_2 = 69.80 \text{ N/mm} \tag{3.10}$$

And the resultant maximum deflection in the spring system is

$$x_{\text{res}} = \frac{F_{\text{sensor, max}}}{k_{\text{res}}} = 0.84 \text{ mm} \tag{3.11}$$

## Buckling

**Critical Buckling Load**

As per Euler's theory, under the assumption that the compressive load is exactly axial and passes through the centroid of the column (vertical rod) section, the buckling load $P_{\text{buckling}}$ is defined as in Equation (3.12), where $l_e$ is the effective length of the column. For the configuration where one end of the column is fixed and the other end is free, the free end will sway sidewise and the curvature in the length will be similar to that of the upper half of the simple column, as shown in Figure 3.6. Thus, $l_e = 2l$.

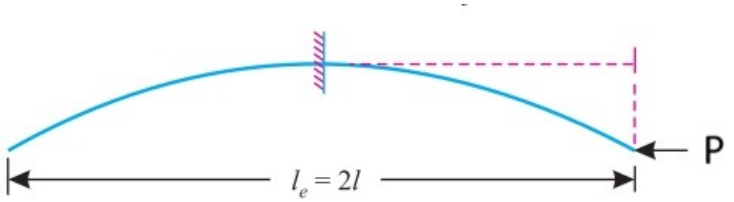


Figure 3.6: Effective length of a column with one end fixed and one free end (Rajput, 2018)

$$P_{\text{buckling}} = \frac{\pi^2 EI}{l_e^2} \tag{3.12}$$

$$\therefore P_{\text{buckling}} = 630.17 \text{ N} \tag{3.13}$$

**Buoyancy**
The buoyant force from water acting on the submerged volume $V$ of the experimental setup under acceleration due to gravity $g = 9.812$ is

$$B = \rho V g$$

$$\therefore B = 204.63 \text{ N} \tag{3.14}$$

Upon comparison of Equation (3.13) and Equation (3.14), the critical buckling load is much higher than buoyancy. Hence, buckling does not occur.

### 3.1.6 Cameras

In dual-phase flow experiments, a total of three digital cameras of the model *Imager Pro X 4M* with a pixel size of 7.4$\mu$m and a resolution of 2048 x 2048 pixels manufactured by *LaVision* were used to capture images of the air layer. They were positioned below the test section as shown in Figure 3.7 to capture consecutive longitudinal segments of the test plate, collectively covering its full length downstream of the injection slot. Data acquisition from the cameras was done through the software *Davis 10.2.1*. The camera that captured the most upstream segment of this length shall be called the *upstream camera* whereas the camera that captured the most downstream segment shall be called the *downstream camera*. The camera that captured the segment between the end segments shall be referred to as the *middle camera*.

The lenses of these cameras differed in their focal length, owing to their availability at the time of experimentation. As shown in Figure 3.7, each camera's field of view (FOV) was manually adjusted to obtain the best parallel orientation with respect to the test plate's bottom face and clarity. As a sanity check, an overlap between the FOVs of adjacent cameras was made sure to exist. Thereafter, with the help of a reference object in (almost) the same plane as the target plane (plate's bottom face), the magnification factor $M$ of each camera was determined according to Equation (3.15). For the upstream camera, the width of the air injection slot was taken as a reference object. For the remaining 2 cameras, a geometrically distinct air bubble travelling from upstream FOV to downstream FOV in reference dual-phase images was used as a reference object. This distinct bubble, however, was first scaled to size using the magnification factor of the first camera. An overview of the specifications of each camera is provided in Table 3.5.

$$M = \text{pixel size} \cdot \frac{\text{length of reference object (px)}}{\text{length of reference object (mm)}} \tag{3.15}$$

## 3.2 Calibration

Calibration of the load cell was performed before experimentation to ensure that measurements taken with it were indicative of the true value. This was done using a primary force standard (weights) and a pulley arrangement in accordance with the guidelines given by ITTC (2017). The end-to-end calibration procedure required

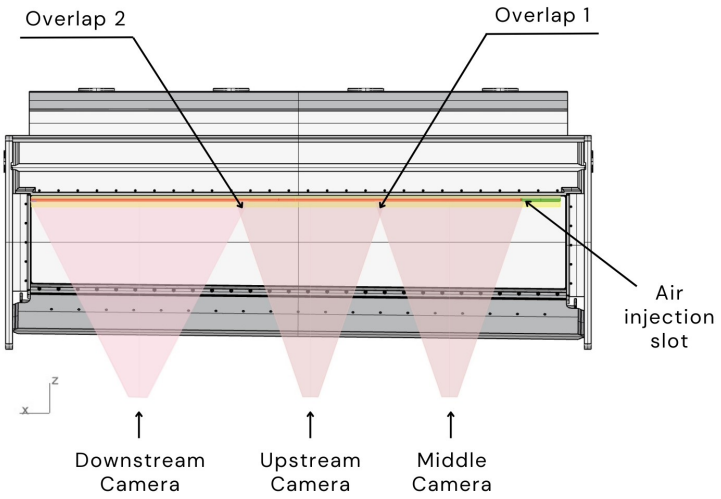


Figure 3.7: Setup of the cameras underneath the test section indicating their respective FOV along with regions of overlap.
(not to scale; for representative purposes only)

Table 3.5: Specifications of the cameras used in dual-phase experiments

| Parameter | Upstream Camera | Middle Camera | Downstream Camera | Units |
|---|---|---|---|---|
| Pixel size | 0.0074 | | | mm |
| Resolution | 2048 x 2048 | | | px |
| Focal length | 35 | 35 | 24 | mm |
| Magnification factor | 0.0296 | 0.0312 | 0.0193 | - |

the implementation of several additional components, namely:

1. **Amplifier**
   *AP28a* produced by BMC Messsysteme GmbH© was used to amplify the voltage signal from the load cell to the range of -5 V to +5 V.
2. **Low-Pass Filter**
   An anti-aliasing filter with a cut-off frequency of 22 Hz was used to process the output from the amplifier.
3. **AD Converter**
   *NI 9205*, an analog-digital (AD) conversion module produced by BMC Messsysteme GmbH©, was used for digitization. The calibration points were chosen such that the highest and lowest values did not over-range the AD converter.
4. **Software**
   *LabVIEW* was used to process the data and output a signal in voltage units of the AD converter. For this, a sampling frequency of 100 Hz was used.

Overall, calibration was performed in three stages, each corresponding to a unique configuration of the load cell as described below. To ensure the same starting condition for each calibration, the force-sensor was pre-loaded at least twice for a duration of 5 minutes.

1. **Dry Calibration - Sensor Only**
   First, the load cell was calibrated when rigidly mounted to a table in air. This was done to assess the performance of the load cell under tension in both its positive and negative directions. To apply load in the opposite direction, the load cell was rotated by 180 ° in the same position. This calibration involved a total of 30 steps with 8 steps in loading and 8 steps in unloading in each direction.

2. **Dry Calibration - Mock Setup**
   Here, the load cell was calibrated when it was mounted in air to a mock experimental setup that mimics the geometry of MPFT's test section. The steps used for this calibration were the same as in the previous stage but the position of the load cell was not changed between opposite directions. Instead, the pulley arrangement was moved because the mock setup did not allow for easy repositioning of the load cell.

   Calibration in this configuration was done to test repeatability, in accordance with ITTC (2017). A null hypothesis using a Student-$t$ test was conducted separately for slope and intercept obtained from a pair of repeated calibrations. Both the slope and intercept obtained from this calibration fit passed this test.

3. **Wet Calibration**
   In this configuration, the load cell was mounted to the final experimental setup inside the test section. To facilitate room for the pulley arrangement and application of weights in air, the test section was not covered with its lid, as shown in Figure 3.8b. The test section (without lid) was filled with water almost up to its brim, such that the load cell was submerged underwater, as shown in Figure 3.8a. Unlike dry calibration, this configuration allowed for measurements in the positive direction only, which is representative of the direction of flow downstream. Therefore, this calibration involved only 16 steps in total, with equal number of steps in loading and unloading. This also meant that a repeatability test according to ITTC (2017) could not be performed in this configuration, owing to the fact that load could not be applied in the negative direction. Hence, the repeatability performance from *Dry Calibration - Mock Setup* was assumed to hold true in this case as well.

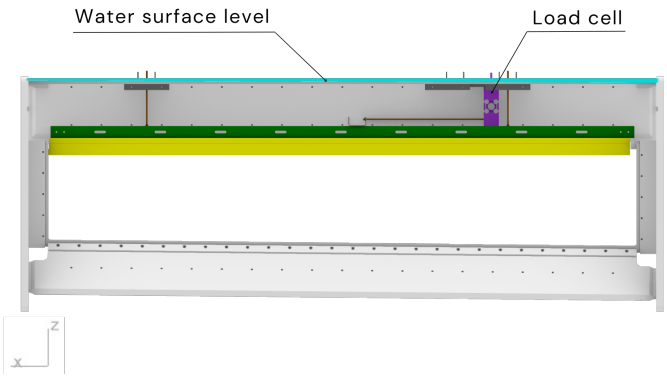


(a) Vertical sectional view of the test section showing the water surface level at which wet calibration was performed.

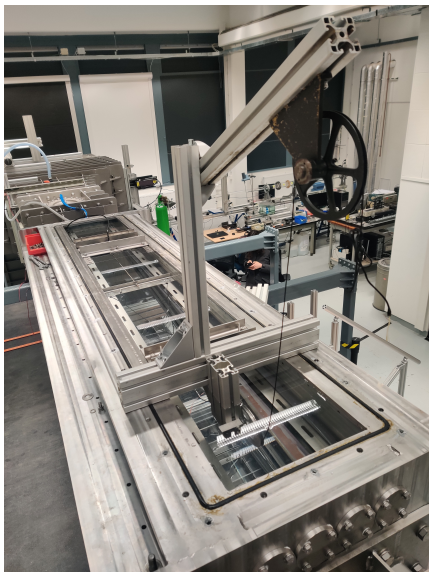

(b) Pulley arrangement for weights

Figure 3.8: Wet calibration setup

Wet calibration was performed after the installation of each plate inside the test section. The measured data obtained from this calibration is presented in Table 3.6a. This was used to determine the calibration factor $B$ of the load cell. From the wet calibration data, a linear regression analysis was conducted to obtain an equation of the form Equation (3.16), where $x$ represents the independent variable, i.e., drag [N] and $y$ represents the dependent variable, i.e., voltage [V].

$$y = a + bx \tag{3.16}$$

The corresponding standard deviation is given by the standard error of estimate $SEE$ defined as in Equa-

tion (3.18), where $SS_R$ is the sum of the square of the residuals.

$$SEE = \sqrt{SS_R/(n-2)} \tag{3.17}$$

$$\text{Residual}_i = y_i - a - bx_i \tag{3.18}$$

However, to convert the output signal from the load cell into drag, the force/volt relationship given by Equation (3.19) was used. Here, $x$ represents the independent variable, i.e., voltage [V] whereas $y$ represents the dependent variable, i.e., drag [N].

$$y' = A + Bx' \tag{3.19}$$

where $A = \frac{-a}{b}$ $B = \frac{1}{b}$ $SEE' = \frac{SEE}{b}$ To assess the validity of the linear regression analysis, normalised residuals were evaluated as

$$\text{Normalised Residual} = \frac{\text{Residual}}{\text{MAX}(y_i) - \text{MIN}(y_i)} \tag{3.20}$$

The linear fit of the wet calibration data along with the corresponding normalised residuals is shown in Figure 3.9. The numerical values for $a$ and $b$ in Equation (3.16) as well as $A$ and $B$ in Equation (3.19) were obtained from a calibration performed in this configuration. These are tabulated in Table 3.6b. $A$ and $B$ were ultimately used to express the voltage output in newtons.

Table 3.6: Details of wet calibration

(a) Wet calibration data

| Load [N] | Output [V] | |
|---|---|---|
| | Conventional Plate | Test Plate |
| 5.174 | 0.365 | 0.367 |
| 10.076 | 0.714 | 0.716 |
| 14.978 | 1.063 | 1.065 |
| 19.879 | 1.413 | 1.414 |
| 24.781 | 1.764 | 1.764 |
| 34.585 | 2.462 | 2.469 |
| 44.389 | 3.160 | 3.173 |
| 54.192 | 3.856 | 3.877 |
| 54.192 | 3.858 | 3.879 |
| 44.389 | 3.181 | 3.195 |
| 34.585 | 2.485 | 2.498 |
| 24.781 | 1.785 | 1.796 |
| 19.879 | 1.436 | 1.445 |
| 14.978 | 1.083 | 1.092 |
| 10.076 | 0.730 | 0.735 |
| 5.174 | 0.375 | 0.381 |

(b) Wet calibration results

| Plate | Parameter | Numerical Value | Units |
|---|---|---|---|
| Conventional Plate | a | 0.00705 | V |
| | b | 0.07182 | V/N |
| | A | -0.09812 | N |
| | B | 13.92465 | N/V |
| Test Plate | a | 0.00631 | V |
| | b | 0.07153 | V/N |
| | A | -0.08815 | N |
| | B | 13.98025 | N/V |

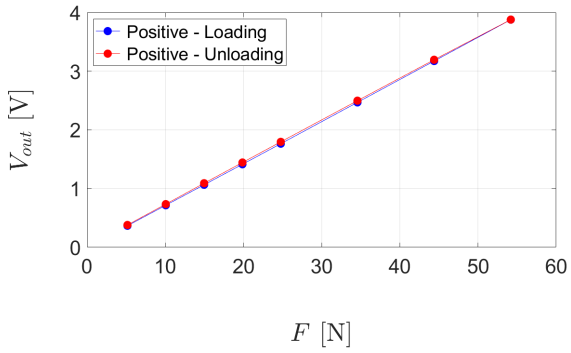


(a) Linear regression fit

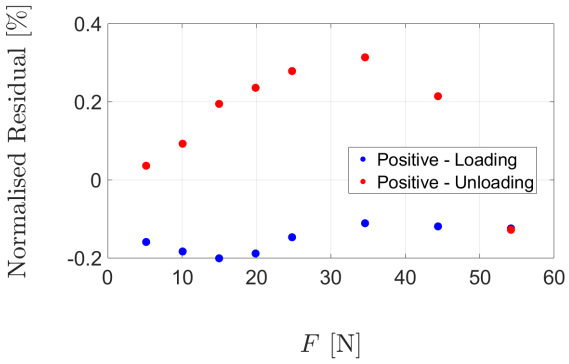


(b) Normalised residuals

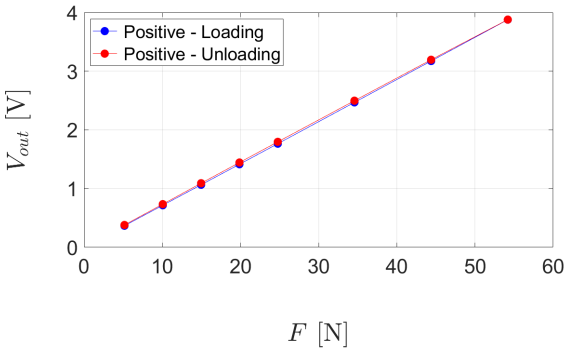


(c) Linear regression fit

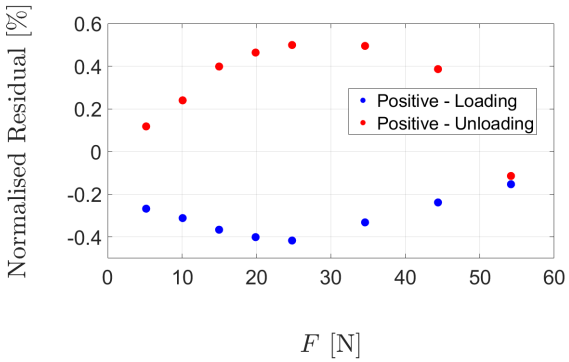


(d) Normalised residuals

Figure 3.9: Wet calibration results
(a), (b) - Conventional Plate
(c), (d) - Test Plate

# 4

# Data Acquisition and Processing

*This chapter describes the steps involved in data acquisition for the experiments conducted and the subsequent processing of images. First, drag was measured on the conventional flat plate in single-phase flow to get a reference dataset. Next, measurements using the test plate were conducted to obtain drag acting in both single-phase and dual phase flow. The drag measurements in dual-phase flow were also accompanied by image capture to visualise the coverage of plate area by air. Finally, the post-processing of images for the determination of the corresponding non-wetted area ratio is explained.*

## 4.1 Conventional Plate

Measurements of the relevant test parameters, namely, $U_\infty$, $T$, and $D$ acting on the conventional plate were taken between 2 m/s and 4 m/s. To ensure a similar starting condition, each run was preceded by a measurement corresponding to a nearly zero free-stream velocity. The runtime $t$ was defined with some trial and error such that the temporal mean of the measured parameters did not change significantly with added measurement time. The measured data, which was available in the form of a *.tdms* file, was averaged over an appropriate time interval in MATLAB to obtain the final experimental values.

Figure 4.1 shows measured signals obtained from a sample run at $U_\infty = 2.11\ \mathrm{m/s}$. Since the signal from the load cell was not equal to zero when there was no water flow, drag at a certain $U_\infty$ was computed as the difference between the averages of the load cell's signals obtained with water flow and without water flow (before the pump was activated). This can be seen in Figure 4.1a, where the signal without water flow used for averaging is highlighted in red and the signal with water flow used for averaging is highlighted in blue. On the other hand, water temperature and free-stream velocity were averaged over an appropriate time period during which the pump was active in the run. This is indicated in blue in Figures 4.1b and 4.1c. Then, as per Equation (3.6), the average of the recorded free-stream velocity was further multiplied with a correction factor of 1.042 to obtain $U_\infty$. Subsequently, $\rho$ and $\nu$ of water were computed from $T$ using Equation (3.3) and Equation (3.4), respectively. Finally, the corresponding $Re$ and $C_F$ were estimated according to Equation (1.2) and Equation (2.19), respectively.

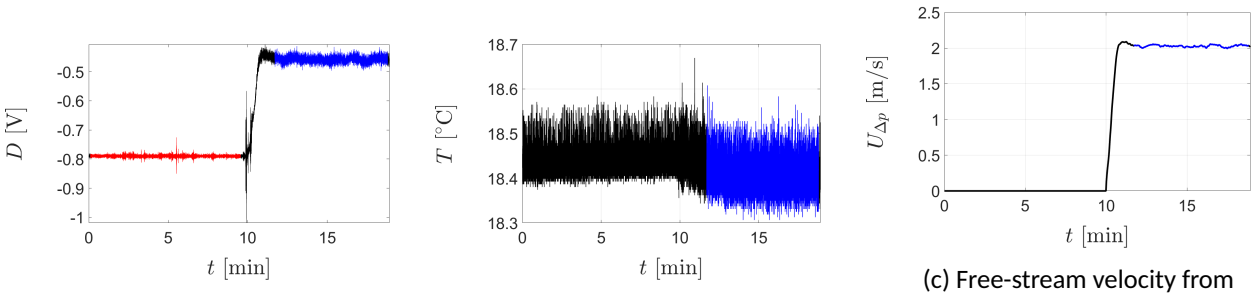


(a) Drag from load cell

(b) Temperature from thermometer

(c) Free-stream velocity from differential pressure sensor

Figure 4.1: Signals of measured parameters from a sample run at $U_\infty = 2.11\ \mathrm{m/s}$

Owing to the highly dependent nature of frictional resistance on viscosity, which is a function of temperature, it is a standard practice to correct $C_F$ to a temperature of 15°C. However, this was avoided because such practice implements prediction of $C_F$ based on theoretical friction lines rather than experimentally obtained values. Thus, it is important to note that $C_F$ reported in this study is characteristic of the range of operating temperature, i.e., $17.4°C \leq T \leq 19.5°C$.

## 4.2 Test Plate

Measurements of the relevant test parameters, namely, $U_\infty$, $T$, and $D$ acting on the test plate were taken in single-phase and dual-phase flow at a representative free-stream velocity of 2.5 m/s. 12 different values for air injection rate $Q_{air}$ = {5, 15, 20, 30, 40, 50, 60, 75, 90, 100, 120, 150} l/min spanning across the different air layer regimes were applied to achieve dual-phase flow. The data acquisition process followed is analogous to that described in Section 4.1. However, in dual-phase flow, an additional step of capturing images was carried out as explained in Section 4.2.1.

Moreover, in the dual-phase experiments, as air injection rate was increased over successive runs, the free-stream velocity was found to decrease even though the pump's rotational frequency remained nearly the same. This was observed probably because the pump was receiving some air, which virtually reduced its pitch. Consequently, the torque generated is lower, but since the pump's control system forces it to run at a constant rotational frequency, a lower free-stream velocity is achieved. This was also associated with significant decrease in the water level inside the test section to an extent that the test plate would not be submerged under water after some time. Therefore, the runtime in dual-phase flow was limited. The severity of this phenomenon increased dramatically with higher $Q_{air}$. Hence, to ensure a similar starting point, the test section was filled to its brim before each run in dual-phase flow.

With the aim to assess the effect of air lubrication on drag acting on the test plate at a certain $U_\infty$, the term drag reduction $DR$ was defined as

$$DR = \left(1 - \frac{C_F}{C_{F,0}}\right) \cdot 100 \tag{4.1}$$

where:
$C_F$ = friction coefficient of the test plate in dual-phase flow, i.e., with air injection
$C_{F,0}$ = friction coefficient of the test plate in single-phase flow, i.e., without air injection

Similarly, to assess the overall effect of air lubrication on drag with respect to the conventional plate, effective drag reduction $DR_{eff}$ is defined for a certain $U_\infty$ as

$$DR_{eff} = \left(1 - \frac{D}{D_{0,ref}}\right) \cdot 100 \tag{4.2}$$

where:
$D$ = drag acting on the test plate in dual-phase flow
$D_{0,ref}$ = drag acting on the conventional plate in single-phase flow

Here, $C_F$ is not taken as the basis for ratio because the two plates have different wetted surface areas, which influence its value differently.

### 4.2.1 Images

A crucial parameter associated with imaging is exposure time. In simple words, this is the amount of time a camera spends taking a picture. It is crucial because it determines:

- the amount of light the digital sensor in the camera receives or brightness of the image
- motion blur, i.e., the blur associated with moving objects in the FOV during that time period

A short exposure time is desirable for minimum motion blur but may produce a dark image. On the other hand, a long exposure time is desirable in low-light environments but produces large blur. For this study, the motion of air bubbles is of interest to capture the area covered by air and therefore exposure time was defined based

on the criteria of minimum motion blur.

Under the assumption that the velocity of injected air is equal to the free-stream velocity of water, the exposure time for each camera was determined from an acceptable motion blur of 1 or 2 pixels as follows:

$$t_{\text{exposure}} = \frac{\text{motion blur}}{U_\infty} \tag{4.3}$$

$$1 \text{ pixel} = \text{pixel size} \cdot \frac{1}{M} \tag{4.4}$$

For each air injection rate in dual-phase flow, a series of independent snapshots of the air layer were taken by the cameras simultaneous with the drag measurements to study its morphology. Here, the term independent means that each set of 3 images (as captured simultaneously by the 3 cameras) represents a unique segment of the aggregate air layer. Doing so essentially ensures that the air captured does not repeat across consecutive images, thus enhancing the quality of the sample set used for image processing. Although no measurements of the velocity of air injected in dual phase flow were recorded, it is assumed to be approximately the same as the free-stream velocity of water. This is because, upon injection into the test section, air is carried in the downstream direction by the tunnel flow. Hence, the frequency of capture $f$ required to obtain independent snapshots was determined based on this assumption as:

$$f = \frac{U_\infty}{x_{\text{extent}}} \tag{4.5}$$

where

$$x_{\text{extent}} = \frac{\text{pixel size} \cdot \text{resolution along flow direction}}{M}$$

Image capture corresponding to each $Q_{air}$ was preceded by a common practice of capturing a background image representative of the condition before air is injected into the system, i.e., single-phase flow. This is essential in image processing, as explained in Section 4.2.1.1. The total number of images $n$ captured at each $Q_{air}$ varied between 500 and 1500, depending on the achievable runtime given the decreasing water level in the test section. In the end, the captured images of the air layer were processed based on the concepts of image segmentation as described in Section 4.2.1.1 to determine the test plate area covered by air, i.e., non-wetted area as a ratio of its total wetted area $A_{nw}/A_w$.

Table 4.1: Camera settings for image capture in dual-phase flow

| Parameter | Upstream Camera | Middle Camera | Downstream Camera | Units |
|---|---|---|---|---|
| $t_{\text{exposure}}$ | 200 | 190 | 150 | $\mu$s |
| $f$ | 1.38 | | | Hz |
| $n$ | [500 1500] | | | - |

### Image Processing

It is known that the fluid in dual-phase flow is a mixture of water and air. In the presence of illumination from the LED panel in the test plate, the boundaries between these two phases cast a shadow and appear as edges in the images captured by the cameras. For the determination of the area covered by air, regions of air must be distinguished from regions of water. To achieve this, the pixels in the image representing air can be labelled a certain value whereas those representing water can be labelled a different value. Since there are only two labels, this translates to a binary approach for image segmentation.

The independent grayscale images of the air layer formed under each air injection rate were available in *.tiff* format. With the binary approach described above, these files were processed in MATLAB using the *Image Pro-*

*cessing* toolbox. A custom code, as given in Appendix A, with the following steps was developed to determine the non-wetted area ratio from each set of 3 images captured by the 3 cameras.

1. **Read**
   The first step was to read the independent grayscale images captured by the 3 cameras into an array of pixels. This was done using the function *imread()* to obtain corresponding raw images.
2. **Crop**
   Since the captured grayscale images contained regions of overlap and objects in the neighbourhood of the test plate, they were cropped to collectively show only the area illuminated by the LED panel with no overlap. This was achieved using the function *imcrop*.
3. **Normalise with background image**
   This is an important step because it removes any distortions in the raw image arising from the initial condition in single-phase flow. Normalisation was done by subtracting the background image from the corresponding raw image.
4. **Filter**
   To reduce noise in the normalised image, it was filtered using a Gaussian filter with a suitable standard deviation.
5. **Binarise with thresholding**
   Then, the normalised grayscale image was converted into a binary image using the function *imbinarise()* with a manually determined threshold based on trial and error. A starting point for this threshold was taken from the function *graythresh()*. This step helps separate the regions of large intensity drops in the image, which are representative of the edges of air or water, from the rest of the image. As a prerequisite to this operation, the normalised grayscale image was first rescaled to the range of [0 1] using the function *imrescale()*. The resultant binarised image shows edges of air or water in black and the remainder in white.
6. **Bridge**
   Upon binarisation, it was observed that the edges of air or water identified in the previous step were open and had gaps in some parts of the image. Thus, to close these edges, a morphological operation called bridging to connect the gaps of 1 pixel was performed using the function *bwmorph('bridge')*. This sets 0-valued (black) pixels to 1 (white), if they have two non-zero neighbouring pixels that are unconnected. Therefore, as a preliminary step to bridging, the binary image obtained from the previous step was inverted.
7. **Fill**
   The result obtained from the previous step only identifies edges of air or water regions. To obtain the area covered by air/water, the area enclosed by a closed boundary must be also assigned the same value as the boundary itself. This was achieved using the function *imfill('holes')* to distinguish areas of water from those of air.
8. **Correct**
   The illuminated area in the raw image did not cover the full extents of the test plate downstream of the injection slot. This means that the cropped grayscale image is missing some small regions of the lubricated plate area around some of its borders. To compensate for this, a correction was applied to expand the filled binary image obtained from the previous step up to the actual extents of the plate. This was done by repeating the area of the image at the relevant borders to artificially represent the situation at the missing regions. The binary image so obtained was used to determine the non-wetted area ratio for the segment downstream of the injection slot as the ratio of the number of white pixels to the total number pixels.

This code was applied on all images captured for $Q_{air}$ = {5, 15, 20, 30, 40, 50, 60}. The non-wetted area from all images corresponding to a certain air injection rate was averaged to get a single value. Finally, since the cor-

rected binary image obtained at the end of *Step 8* represents only the segment of the test plate downstream of the injection slot, this ratio was further multiplied by the factor 78.76/100 (corresponding to the maximum lubricatable area explained in Chapter 6) to get the non-wetted area ratio in terms of the test plate's total wetted surface area. Representative images corresponding to the upstream camera and $Q_{air} = 30\,\mathrm{l/min}$ obtained from image processing are shown in Figure 4.2.

Owing to the tedious nature of the manual optimisation of the binarisation threshold and the largely faint boundaries between air and water, images corresponding to $Q_{air}$ = {75, 90, 100, 120, 150} l/min were not processed as explained above to determine the non-wetted area ratio under these conditions. However, for $Q_{air}$ = {100, 120, 150} l/min, owing to the vast area covered by air, it was possible to manually fill the sparse regions of water. Then, the non-wetted area ratio was computed from the inverse of the manually filled image. Nevertheless, given the time-intensive nature of manual filling, this was only done for 2 image sets per $Q_{air}$.

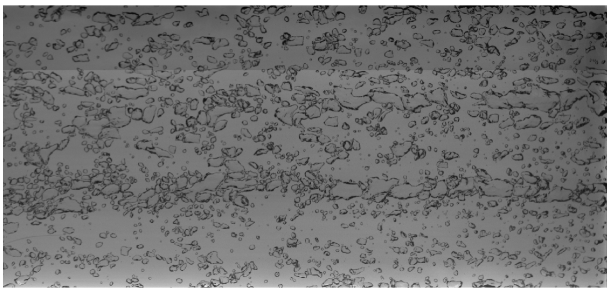

(a) Grayscale image after cropping

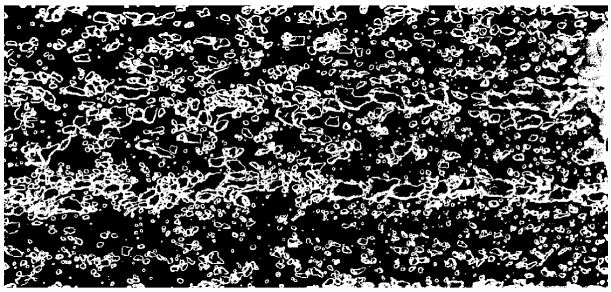

(b) Binary image after bridging, showing the detected boundaries of water/air

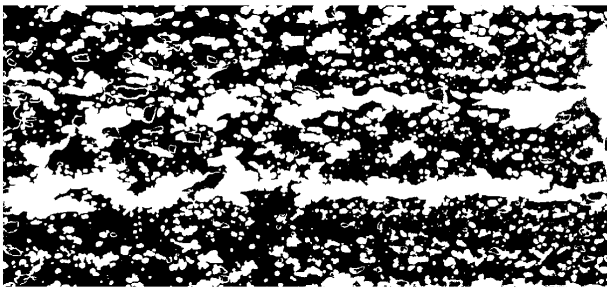

(c) Binary image after filling

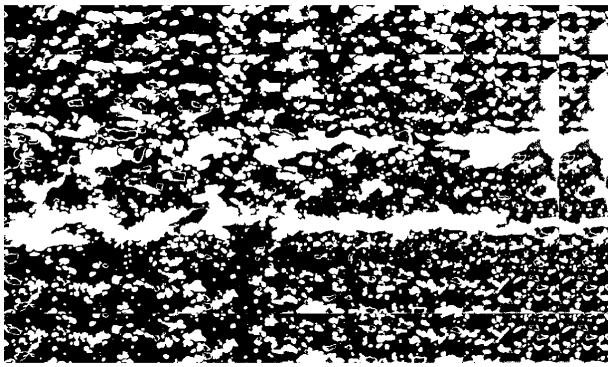

(d) Binary image after correction at the top, bottom, and right borders

Figure 4.2: A glance at the steps involved in image processing for the upstream camera and $Q_{air} = 30$ l/min. Flow direction is from right to left.

# 5 Uncertainty Analysis

*This chapter provides an estimation of uncertainty in friction coefficient, drag reduction, effective drag reduction, and non-wetted area ratio for the quantification of their accuracy. First, the uncertainty in the drag measurements conducted on the conventional plate is discussed. This is followed by the estimation of uncertainty in the drag measurements on the test plate. Thereafter, the uncertainty in the corresponding drag reduction, effective drag reduction, and non-wetted area ratio are assessed.*

## 5.1 Conventional Plate

### 5.1.1 Friction Coefficient

To assess the accuracy of the drag measurements conducted on the conventional plate, the recommendations set by International Towing Tank Conference (2002) for uncertainty in resistance tests were followed. This was done by considering the contribution of each relevant measured parameter and evaluating uncertainty of the dimensionless friction coefficient, $C_F$. Since $C_F$ is a function of several other individual variables, its uncertainty originates from the uncertainty in the individual variables. This data structure is depicted in a block diagram with individual measurement systems, measurement of individual variables, data reduction equation, and the final experimental results as shown in Figure 5.1.

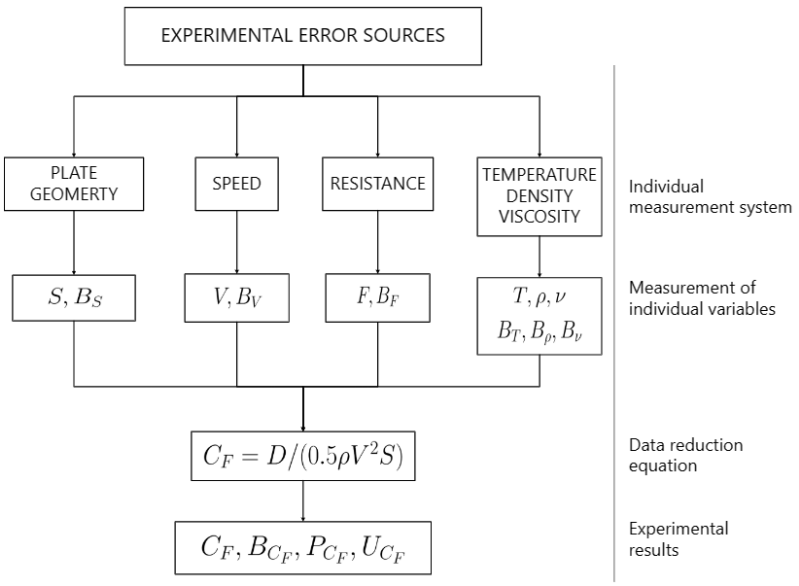


Figure 5.1: Block diagram of the test procedure

Table 5.1: Experimental data

| Parameter | Magnitude | Units |
|---|---|---|
| $V$ | 2.11 | m/s |
| $D$ | 4.63 | N |
| $l$ | 1.949 | m |
| $b$ | 0.2935 | m |
| $S$ | 0.5733 | $m^2$ |
| $T$ | 18.4 | °C |
| $\rho$ | 998.76 | $kg/m^3$ |
| $C_F$ | 0.003945 | - |

The total uncertainty in $C_F$ is defined as the root sum square of the uncertainties of the total bias and precision limits, as in Equation (5.1). A detailed account of the estimation of $U_{C_F}$ from the experimental data tabulated

in Table 5.1 is given below.

$$\left(U_{C_F}\right)^2 = \left(B_{C_F}^2\right) + \left(P_{C_F}{}^2\right) \tag{5.1}$$

1. **Bias Limit**
   Bias or systematic error remains fixed during the time period of one complete experimental run. It is simply a steady error. The total bias limit from the individual measurement systems: wetted surface area, free-stream velocity, drag, and density is given by:

$$\left(B_{C_F}\right)^2 = \left(\frac{\partial C_F}{\partial S} B_S\right)^2 + \left(\frac{\partial C_F}{\partial U_\infty} B_{U_\infty}\right)^2 + \left(B_{C_F}\right)^2 = \left(\frac{\partial C_F}{\partial D} B_D\right)^2 + \left(B_{C_F}\right)^2 = \left(\frac{\partial C_F}{\partial \rho} B_\rho\right)^2 \tag{5.2}$$

   (a) **Wetted Surface Area**
   A manufacturing error of ~1.3 mm$^2$ was measured. This leads to a bias limit in wetted surface area $B_S = 0.0013$ m$^2$ corresponding to a 0.219% of the wetted surface area of 0.5733 m$^2$.

   (b) **Free-stream Velocity**
   The uncertainty from LDV measurements used to obtain the correction factor for the free-stream velocity as determined using the differential pressure sensor and Bernoulli's principle was estimated to be 1%. This translates to a bias uncertainty in free-stream velocity $B_{U_\infty} = 0.0211$ m/s.

   (c) **Frictional Resistance or Drag**
   Several components contribute to the total bias error in drag. These were evaluated as follows.

   - **Calibration**
     Since the load cell was calibrated with weights, they are a source of error. The bias error arising from the tolerance of the calibration weights is defined as $B_{D_1} = D \cdot$ accuracy of weights $= 4.63 \times (1 - 0.999308) = 0.003203$ N, which is 0.0692% of $D$ = 4.63 N.
   - **Data Acquisition**
     The bias from the calibration fit of the load cell was calculated as $B_{D_2} = 2 \cdot SEE'$, where $SEE'$ is the standard error of estimate of the force/volt relation represented by Equation (3.19). With $SEE' = 0.0963$ N, $B_{D_2}$ evaluates to 0.1925 N, which represents 4.1598% of $D$ = 4.63 N.
   - **Misalignment**
     The possibility of misalignment in the flat plate induces a bias uncertainty. Based on an estimated misalignment of $\theta = \pm 1°$, this was computed as $B_{D_3} = D - D\cos\theta$. This evaluates to 0.000705 N or 0.0152% of $D$ = 4.63 N.
   - **AD Data Conversion**
     An AD converter typically has an error of 1 bit out of its accuracy. The resulting bias error is defined as $B_{D_4} = \left(1 \cdot \text{voltage range}\right) / 2^{\text{bits}} \cdot B$. For the 16-bit AD converter with a voltage range of 10 V used in calibration of the load cell, this leads to a bias uncertainty of 0.0021 N or 0.0459% of $D$ = 4.63 N.

   Thus, the total bias uncertainty in drag as a result of all these 4 subcomponents was obtained from $B_D = \left(B_{D_1}^2 + B_{D_2}^2 + B_{D_3}^2 + B_{D_4}^2\right)^{0.5} = 0.1926$ N. This is equal to 4.161% of $D = 4.63$N.

   (d) **Density**
   Two components contribute to the total bias error in density. These were evaluated as follows.

   - **Calibration**
     The thermometer was calibrated with an uncertainty of $B_T = 0.3°C$. Based on the density/temperature relation as given in Equation (3.3) proposed by International Towing Tank Conference (2006) for $g = 9.81$ m/s, the bias $B_{\rho_1}$ was calculated according to Equation (5.3).

$$B_{\rho_1} = \left|\frac{\partial \rho}{\partial T}\right| B_T \tag{5.3}$$

     For $T = 18.4°$ C, this yields $B_{\rho_1} = 0.0563$ kg/m$^3$.

- **Data Reduction**
  From the calibration curve fit of the density/temperature relationship, the bias limit in density is $B_{\rho_2} = 2 \cdot SEE = 0.070$ kg/m$^3$.

Finally, the total bias in density was found as $B_\rho = \sqrt{B_{\rho_1}^2 + B_{\rho_2}^2} = 0.1263$, which is $0.0124\%$ of $\rho = 998.76$ kg/m$^3$.

2. **Precision Limit**
   The precision or random uncertainty contributes to the scatter of the measured data. The precision limit was estimated using an end-to-end method that includes the precision errors of all the individual measurement systems. In order to include random errors such as misalignment, the standard deviation must be determined from multiple tests. The precision limit for multiple tests is calculated according to Equation (5.4), where $M$ is the number of runs, $SDev$ is the standard deviation established by $M$ runs, and $K$ is the coverage factor, which is equal to 2 for a 95% confidence level.

$$P(M) = \frac{K\, SDev}{\sqrt{M}} \tag{5.4}$$

   In the present work, the precision limit was determined from 6 experimental runs at $V = 2.11$ m/s with $SDev = 1.118 \cdot 10^{-6}$ as $P_{C_F} = 9.01 \times 10^{-6}$. Since the measurement equipment and apparatus remain unchanged, the precision limit was considered to be the same for all measurements.

3. **Total Uncertainty**
   The total uncertainty in the time-averaged value of $C_F$ was estimated using Equation (5.1). This was found to be $1.674 \times 10^{-4}$, which is 4.623% of $C_F = 3.621 \times 10^{-6}$.

## 5.2 Test Plate

### 5.2.1 Friction Coefficient

Uncertainty in friction coefficient corresponding to the test plate under single-phase and dual-phase flow was computed the same way as described in Section 5.1.1 using the parameters corresponding to the test plate.

### 5.2.2 Drag Reduction

According to the theory of propagation of errors, the uncertainty in $DR$ was obtained from $C_F$ and $C_{F,0}$ as

$$U_{DR} = \sqrt{\left(\frac{-1}{C_{F,0}}\right)^2 \cdot U_{C_F}^2 + \left(\frac{C_F}{C_{F,0}^2}\right)^2 \cdot U_{C_{F,0}}^2} \tag{5.5}$$

### 5.2.3 Effective Drag Reduction

The uncertainty in $DR_{eff}$ was also determined according to the theory of propagation of errors from $D$ and $D_{0,ref}$ as

$$U_{DR_{eff}} = \sqrt{\left(\frac{-1}{D_{0,ref}}\right)^2 \cdot U_D^2 + \left(\frac{D}{D_{0,ref}^2}\right)^2 \cdot U_{D_{0,ref}}^2} \tag{5.6}$$

### 5.2.4 Non-Wetted Area Ratio

To determine the uncertainty in the non-wetted area ratio as obtained from image processing, ground truth images were obtained by manual filling of the air regions in the grayscale image. This was done for 2 different image sets corresponding to a certain $Q_{air}$ using the *Image Segmenter* application in MATLAB. Then, the ground truth image was also corrected as described in *Step 8* under Section 4.2.1.1 to get the true value of non-wetted area ratio. The true value of non-wetted area ratio for a given $Q_{air}$ was determined as the average of the

true values obtained from the corresponding 2 image sets. For convenience, this exercise was performed only on images corresponding to a few injection rates. For the remaining injection rates, manual filling of regions covered by air proved to be much more tedious and time-consuming.

A bias error of 1% was assumed to originate from the manual filling operation. The remaining contribution to uncertainty was determined as the difference in positions of the wetted and non-wetted regions between the ground truth result and the code-generated result. Deviation from the ground truth image was found to arise from the following two factors:

- regions of air that remain unfilled due to pixel gaps found in their boundary upon binarisation
- regions of water that get filled owing to their position within a closed boundary formed by air bubbles

A sample image highlighting one region of water that is incorrectly filled and one region of air that incorrectly remains unfilled is given in Figure 5.2. Similiarly, there are several other regions (small to big) distributed across this image that deviate from the ground truth result.

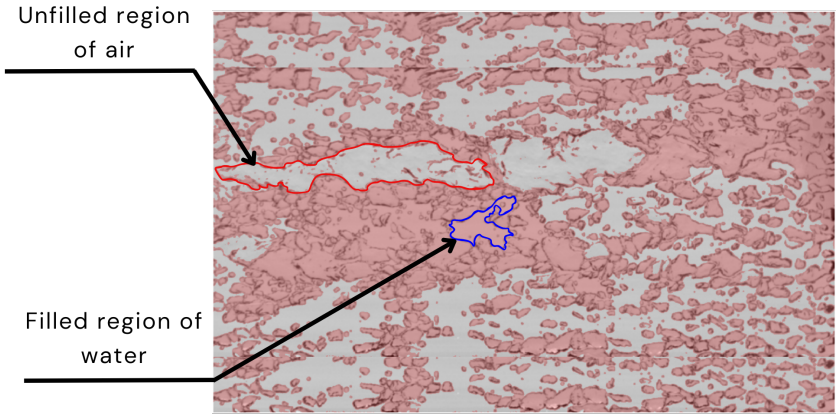


Figure 5.2: Overlay of the code-generated result (light red) upon the corrected grayscale image corresponding to the upstream camera and $Q_{air} = 50$ l/min.

# 6

# Results and Discussion

*This chapter presents the results from Chapters 3-5 in the order of their occurrence: from the design of the force balance to the drag measurements conducted on the conventional plate in single-phase flow and those conducted on the test plate in single-phase as well as dual-phase flow. To assess drag reduction due to air lubrication in terms of non-wetted area ratio, the results from image processing conducted on the test plate in dual-phase flow are presented. These are evaluated in terms of variation in drag across the three air regimes and based on their morphology. A comparison with the most relevant studies from the cited literature is also made to identify potential agreements and highlight how the present study differs from them.*

A force balance was designed to accommodate the free movement of the plate in the presence of drag. An experimental setup comprising a suitable load cell to measure drag acting on the plate along with other sensors and an imaging apparatus was built for data acquisition. Drag measurements were conducted on the conventional plate in single-phase flow between 2.1 m/s and 4 m/s to obtain a reference dataset. The results from these measurements are compared with different theoretical friction lines in Figure 6.1. The friction coefficient was found to be higher than the theoretical prediction for the same Reynolds number and appears to follow the same trend as the Prandtl-Schlichting line but with a slight offset. Although a possible explanation for this

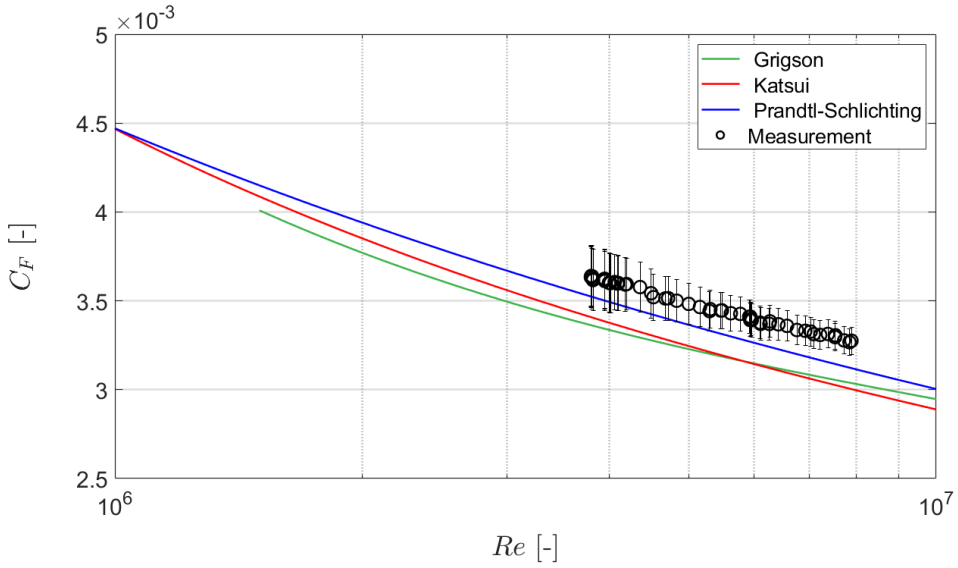


Figure 6.1: Comparison of experimentally determined $C_F$ versus $Re$ of the conventional plate with different friction lines

higher friction coefficient could not be identified, a comment on the associated uncertainty can be made. The uncertainty in $C_F$ decreases with increasing $Re$. This decrease could be explained by the contributions to the uncertainty. From the uncertainty analysis of $C_F$ conducted in Section 5.1.1, it can be deduced that the largest contributor to uncertainty is the bias error from the calibration fit of the load cell. This uncertainty improves as

the load cell moves away from operating near the extreme end (say < 10%) of its full-scale range (FSR), owing to the fact that a sensor is typically more susceptible to noise at the extreme ends of its FSR.

From the single-phase flow experiments conducted on the conventional plate and the test plate over the same range of free-stream velocities, the associated drag was obtained. In Figure 6.2, this experimental data is compared with results from Zverkhovskyi (2014), as the plates used in both these studies are similar in dimensions. The drag on both plates increases with increasing velocity. Moreover, for a given $U_\infty$, the drag acting on the test plate is between ~37% and ~39% higher than that on the conventional plate. This can be attributed to the 35.2% greater wetted surface area of the test plate originating from its fences and lip. In comparison to Zverkhovskyi's results, the drag on the conventional flat plate is rather similar. The drag on the test plate, however, is significantly higher, owing to the larger increase (as opposed to 20%) in wetted surface area from higher fences.

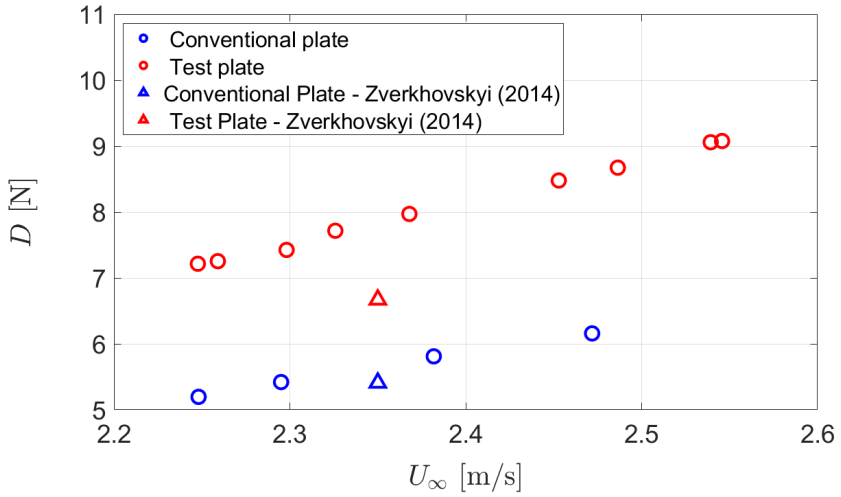


Figure 6.2: Drag versus free-stream velocity

Owing to the position of the injection slot on the test plate and the (approximate) maximum thickness of the air layer observed $t_{a,\max} = 2$ cm, the maximum area that could be covered with air, i.e., maximum lubricatable area, in dual-phase flow was found to be 78.76% of the test plate's total wetted surface area. This was estimated from the contributions of the following:

- part of the test plate's bottom layer downstream of the injection slot, 68.34%
- part of fences downstream of the injection slot but only up to a height of $t_{a,\max}$, 9.29%
- lip, 1.13%

An overview of this area distribution of the test plate is depicted in Figure 6.3.

From the single-phase and dual-phase flow experiments conducted on the test plate, drag reduction due to air lubrication and the corresponding non-wetted area ratio were determined. Figure 6.4 shows the drag reduction and non-wetted area ratio obtained with the 12 different air injection rates at the representative velocity of 2.5 m/s. The air layer regimes indicated here were identified based on the change in the slopes of $DR$ versus $Q_{air}$, as described by Elbing et al. (2008). Up to $Q_{air}$ = 20 l/min, the $DR$ is negative or nearly zero. Between $Q_{air}$ = 30 l/min and 50 l/min, a linearly increasing trend is observed. This regime is identified as BDR. Then, from $Q_{air}$ = 60 l/min to 90 l/min, a linearly increasing trend but with a slightly higher slope is observed. This is identified as TALDR. The onset of TALDR near $Q_{air}$ = 60 l/min is also evident in images from the appearance of coalesced air patches distributed randomly over the full length of the test plate downstream of the injection slot. Finally, between $Q_{air}$ = 100 l/min and 150 l/min, the slope no longer increases linearly and tends to flatten at $Q_{air}$ = 150 l/min. This is recognised as ALDR.

While Elbing et al. (2008) reported a maximum $DR$ of nearly 100% (Figure 2.6a), the maximum $DR$ obtained

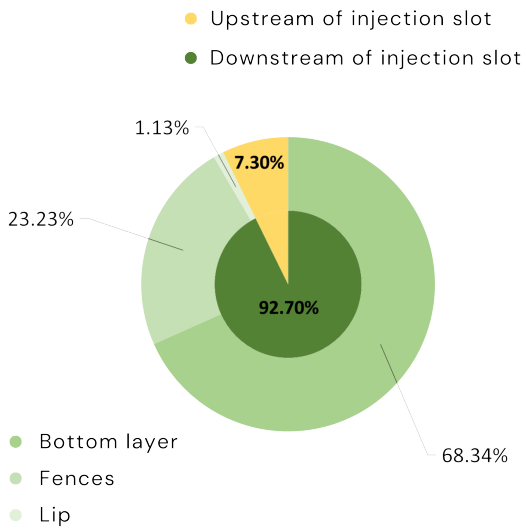


Figure 6.3: Distribution of wetted surface area of the test plate

from the present study is only ~55%. Nevertheless, both these maxima are observed in the ALDR regime. The maximum $DR$ achieved in the other two regimes is also comparatively lower: ~9% and ~32% instead of 20% and 80% in BDR and TALDR, respectively. These differences are mainly due to the fact that, in the present study, drag reduction was assessed with respect to the entire test plate whereas air lubrication was only possible on the section of the test plate downstream of the injection slot. Adjustment of this drag reduction to represent the drag reduction corresponding to the section of the test plate downstream of the injection slot would require eliminating the contribution to drag from the section of the test plate upstream of the injection slot, i.e., which does not receive air flow. However, since this drag was not actually measured, the drag reduction results from the current study are presented as they are. Besides, as explained above, a maximum of 78.76% of the test plate's total wetted surface area could be expected to be covered with air. So, a 100% total $DR$ would be practically impossible to achieve from the current setup.

For the lowest injection rate, a rough evaluation of the bubbly regime was made to identify the possible factors leading to a negative $DR$. First, the non-deformability of small bubbles as proposed by Lu et al. (2005) was considered. From a rough estimate of the bubble size based on 5 bubbles from 5 images corresponding to $Q_{air} = 5$ l/min, the bubble diameter $d_{bubble}$ was found to be ~6 mm. Since this is much higher than the size (~300 $\mu$m) at which drag increase was noted by Lu et al. (2005), the factor of non-deformability was discarded. On the other hand, however, this bubble size is comparable to the bubble size (5 mm) at which Zhao and Zong (2023) observed negative drag reduction in BDR. Although further investigation is necessary to identify why drag reduction is negative here, it can be conjectured that this could be explained by the same mechanism they proposed: the combined effect of increase in effective kinematic viscosity and insignificant decrease in mixture density.

Moreover, as $Q_{air}$ increases, $A_{nw}/A_w$ also increases. This is in agreement with Nikolaidou et al. (2021)'s results for $A_{nw}/A_w$ versus $Q_{air}$ (Figure 2.7a) at relatively higher free-stream velocities. However, a decrease in $A_{nw}/A_w$ at higher $Q_{air}$ was not observed. This is likely because 2.5 m/s is sufficiently high to support the downstream increase of the air layer's length, thus increasing its non-wetted area ratio. Another observation that can be made from this figure is that $A_{nw}/A_w$ is always higher than the corresponding $DR$. This means that to attain a certain percentage of drag reduction, a relatively higher percentage of non-wetted area is required. Additionally, in the ALDR regime, while the non-wetted area ratio increases by just $\sim 1\%$ between $Q_{air} = 100$ l/min and 120 l/min, a rather more significant increase of $\sim 7\%$ is observed in $DR$. This disproportionate increase could possibly be explained by the observed partial coverage of the fences by the thickness of the air layer $t_a$. However, since this parameter was not measured, a definitive answer cannot be given for this behaviour. Nevertheless, it is admittable that, since the non-wetted area ratio presented here does not take

into account the contribution from the non-wetted area of the fences, its reported value in the ALDR regime is lower than its true value. Lastly, with a broader perspective, the effective drag reduction with respect to the conventional plate is presented here as $DR_{eff}$ to quantify the overall effect of air lubrication. While $DR_{eff}$ is always expected to be lower than $DR$, it is encouraging to see that $DR_{eff}$ increases from a negative value ($\sim 35\%$) to a similarly large ($\sim 37\%$) positive value.

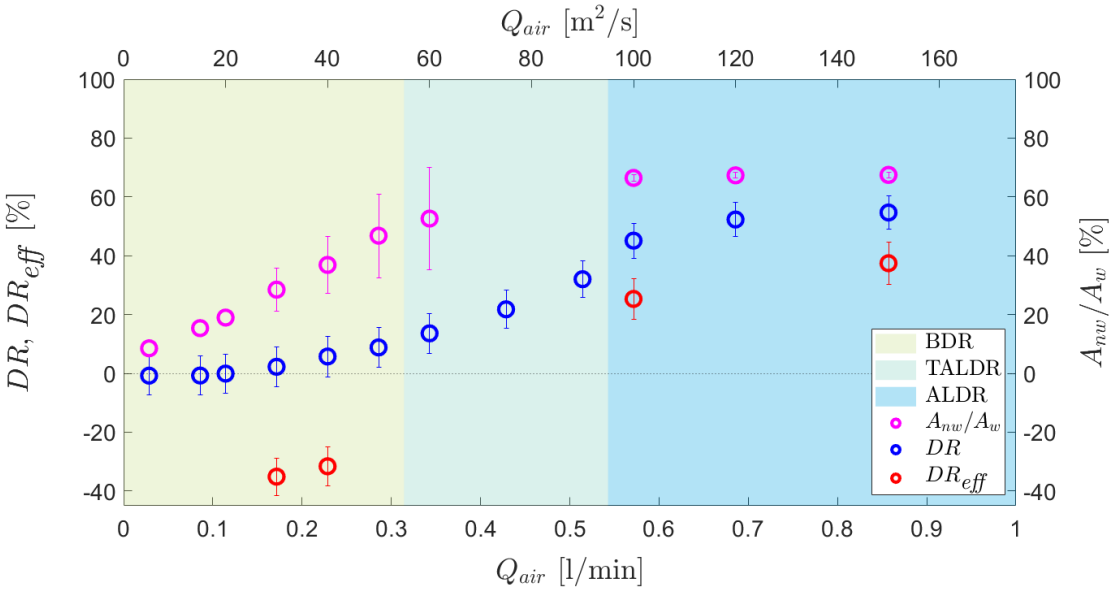


Figure 6.4: Drag reduction, effective drag reduction and non-wetted area ratio versus air injection rate at a representative free-stream velocity of 2.5 m/s

Representative images captured by the middle camera at $Q_{air}$ = {30, 60, 100} are shown in Figure 6.5. In Figure 6.5a, air appears as tiny to large bubbles with a rather sparse distribution across the image, whereas in Figure 6.5b, the bubbles are even larger and also exhibit coalescence to form patches of air. In Figure 6.5c, a rather continuous film of air is visible, with small droplets of water observed to drip from the plate's surface due to gravity as the air layer flaps against it.

Now, with the aim to understand how the morphology, i.e., area covered by the air layer, influences drag reduction on the plate, $DR$ is represented as a function of $A_{nw}/A_w$ in Figure 6.6. Within the BDR regime, after overcoming negative $DR$, a linearly increasing behaviour with a rather small slope is observed. Similarly, within the ALDR regime, a linearly increasing behaviour still persists but with a much steeper slope. While these linearly increasing trends confirm that a correlation between drag reduction and non-wetted area ratio exists in BDR and ALDR, they also indicate that some other factor influences the slope of this dependency across these two regimes. This factor is probably the underlying physical mechanisms responsible for drag reduction in the different air layer regimes. While the effect of decrease in fluid density and viscosity may be common to all, the significant variation of slope observed in the $DR$ vs $A_{nw}/A_w$ plot across the different regimes suggest there may be other phenomena that intensify the effect of non-wetted area ratio on drag reduction from BDR to ALDR.

As tabulated in Table 6.1, the test conditions in dual-phase experiments on the test plate varied in velocity between 2.55 m/s and 2.25 m/s (a standard deviation of 4.2%) over the range of air injection rates. This is why these tests were considered to be performed at a representative velocity of 2.5 m/s. Moreover, it was ensured that the velocity in the single-phase measurements lied within 1% of the corresponding velocity recorded in dual-phase flow. So, the drag reduction obtained from these conditions can still be considered as a pure effect of air lubrication.

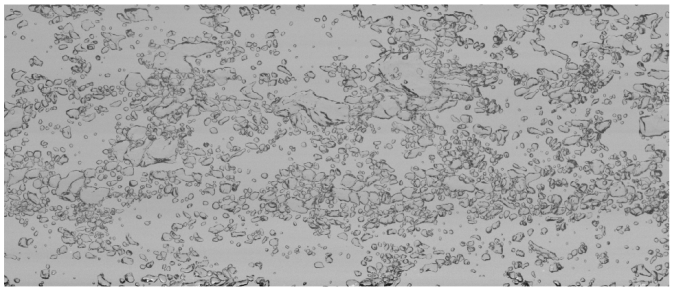

(a) $Q_{air}$ = 30 l/min

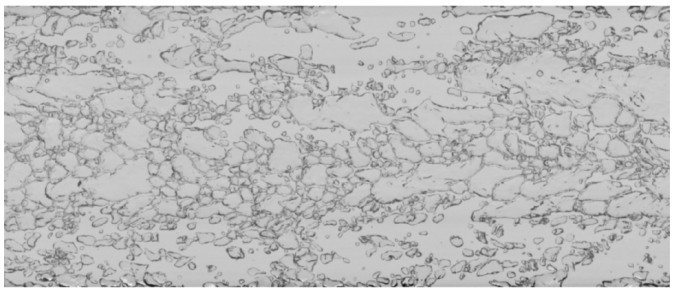

(b) $Q_{air}$ = 60 l/min

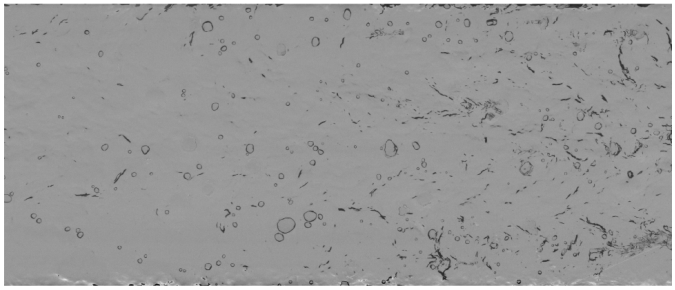

(c) $Q_{air}$ = 120 l/min

Figure 6.5: Images corresponding to the middle camera and $Q_{air}$ = {30, 60, 100} captured at an instance of time

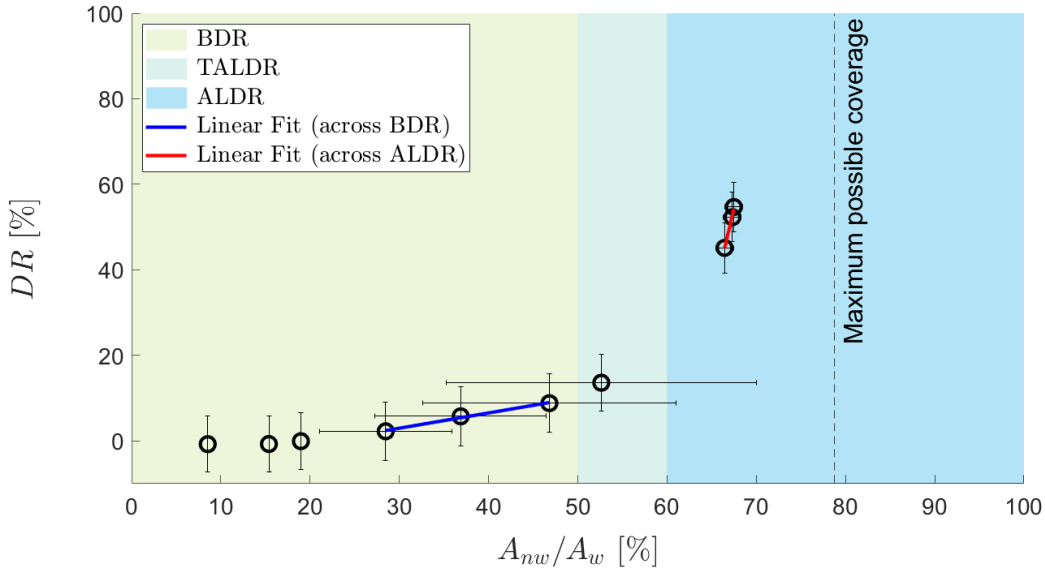


Figure 6.6: Drag reduction versus non-wetted area ratio at a representative free-stream velocity of 2.5 m/s and increasing air injection rates

Table 6.1: Experimental data used in drag reduction estimates

| **Single-Phase Flow** | | **Dual-Phase Flow** | | | |
|---|---|---|---|---|---|
| [m/s] | [N] | [l/min] | [m/s] | [N] | [$m^2$] |
| $U_\infty$ | $D$ | $Q_{air}$ | $U_\infty$ | $D$ | $A_{nw}/A_w$ |
| 2.55 | 9.08 | 5 | 2.54 | 9.10 | 8.52 |
| 2.54 | 9.06 | 15 | 2.53 | 9.09 | 15.36 |
| 2.49 | 8.67 | 20 | 2.50 | 8.81 | 18.95 |
| 2.45 | 8.48 | 30 | 2.46 | 8.32 | 28.44 |
| 2.37 | 7.97 | 40 | 2.39 | 7.65 | 36.83 |
| 2.37 | 7.97 | 50 | 2.36 | 7.23 | 46.76 |
| 2.37 | 7.97 | 60 | 2.35 | 6.75 | 52.57 |
| 2.33 | 7.72 | 75 | 2.33 | 6.03 | - |
| 2.33 | 7.72 | 90 | 2.32 | 5.23 | - |
| 2.30 | 7.42 | 100 | 2.29 | 4.05 | 66.36 |
| 2.26 | 7.25 | 120 | 2.26 | 3.46 | 67.24 |
| 2.25 | 7.22 | 150 | 2.24 | 3.25 | 67.40 |

# 7

# Conclusions and Recommendations

*This chapter summarises all the key findings from the present work by answering the main research questions through the defined sub-questions. It ends with a few recommendations, which may be either suggestion for improvement or scope for further research.*

## 7.1 Conclusions

1. **How to design a force balance to experimentally measure the total friction drag on a flat plate?**

   For the measurement of total friction drag on a flat plate, a custom force balance comprising a spring system with suspension rods and a load cell was designed based on the concepts of beams, columns, and springs. The load cell was calibrated to obtain a relation to convert its voltage output into drag. The calibration also passed a null hypothesis test (using a Student-$t$-test) for repeatability.

2. **How can the drag measurement system be validated?**

   (a) What empirical and semi-empirical formulas can be used for comparison?

   Total drag acting on a conventional flat plate was measured to obtain a reference dataset. For validation, the friction coefficient of the conventional flat plate was compared with a number of empirical and semi-empirical formulas, namely Grigson's, Katsui's, and Prandtl-Schlichting's. The drag acting on the conventional plate was found to be higher than predicted by these formulas and follows the same trend as the Prandtl-Schlichting line but with a slight offset.

   (b) What is the recommended procedure for performing an uncertainty analysis?

   To assess the accuracy of the drag measurements conducted on the conventional plate, the recommendations set by International Towing Tank Conference (2002) for uncertainty in resistance tests were followed. This required considering the contribution of each relevant measured parameter and evaluating uncertainty of the dimensionless friction coefficient, $C_F$.

3. **How does drag reduction vary across the three air regimes?**

   To study the variation in drag reduction across the three air regimes, tests at a representative free-stream velocity of 2.5 m/s for a set of increasing air injection rates were conducted. Air layer regimes were identified based on the change in slope of the $DR$ versus $Q_{air}$ curve. The corresponding results show that drag reduction increases with slightly different slopes in BDR and TALDR and reaches a plateau in ALDR.

   (a) What is the maximum drag reduction achieved in each regime?

   The maximum drag reduction achieved in each of BDR, TALDR, and ALDR are ~9%, ~32% and ~55%, respectively.

   (b) Does drag increase in the presence of air in any case? If yes, why?

   Negative drag reduction was observed in BDR for the lowest three air injection rates. The average size of the bubbles causing maximum drag increase was roughly estimated to be 6 mm. Based on this size, a conjecture that the drag increase could be explained by the combined effect of increase in effective kinematic viscosity and insignificant decrease in mixture density was suggested.

4. **How does the morphology of air under the plate influence drag reduction?**

   The non-wetted area of the plate was found to increase with increasing air injection rates across the three air layer regimes. Each of the three air layer regimes corresponded to a distinct air morphology observed in images. In BDR, air appears as tiny to large bubbles with a rather sparse distribution across the image, whereas in TALDR, the bubbles are even larger and also exhibit coalescence to form patches of air. In ALDR, a rather continuous film of air is visible, with small droplets of water observed to drip from the plate's surface due to gravity as the air layer flaps against it.

   A positive linear correlation was found to exist between drag reduction and the associated non-wetted area ratio achieved in BDR and ALDR. However, this correlation varies in slope per air layer regime, possibly due to the physical phenomena governing the regime.

## 7.2 Recommendations

Recommendations for the improvement of the present work and suggestions for further research are give below.

### 7.2.1 Improvements

1. The bias uncertainty in $C_F$ from the calibration fit of the load cell could be improved by the selection of a sensor with a smaller full-scale range that still fits the limits of the expected drag.

   The selected load cell has a large capacity of 6 kg. As known with sensors, their combined error (the error combining non-linearity and hysteresis) is specified as a percentage of their FSR. When a sensor is used to measure loads within a smaller range of its FSR, its absolute accuracy can be compromised because the sensor's combined error becomes a larger percentage of the smaller measurement range.

2. The variation in free-stream velocities in dual-phase flow could have been avoided by setting higher pump rotational frequency at higher $Q_{air}$.

   The variation in free-stream velocities (Table 6.1), which occurred at a constant pump rotational frequency, is likely due to the presence of air inside the pump, which led to a virtual decrease in its pitch (Section 4.2). Higher rotational frequencies at higher air injection rates could have helped overcome this effect and achieve nearly the same free-stream velocity for all the applied air injection rates.

3. Estimates for the non-wetted area ratio at $Q_{air} = \{75, 90\}$ l/min would have added more resolution to the correlation between $DR$ and $A_{nw}/A_w$ shown in Figure 6.6, particularly in the transitional regime. More time spent on image processing could have helped achieve this.

### 7.2.2 Further Research

1. Since the thickness of the air layer was found to partially cover the area of the fences along the plate, the investigation of the correlation between drag reduction and non-wetted area ratio could be expanded to incorporate the contribution to the non-wetted area ratio from the thickness of the air layer.

2. Further investigation into the underlying physical phenomenon governing drag reduction across each of the three air layer regimes could shed light on the factors determining the slope of the drag reduction/non-metted area relation in each regime.

# A

# Image Processing Code

```
Q_val = 5; % Q_air
Q = [5 15 20 30 40 50 60 75 90 100 120 150];
Q_index = find(Q==Q_val)
numfiles = [1500 1500 1500 1500 1500 1500 1500 1500 1500 1358 966 883];
% numfiles = [1 1 1 1 1 6 1 1 1 1 1 1];
if Q_index > 5 % based on frequency of aqcuisition
    step = 1; % for 1.38 Hz
else
    step = 3; % for images captured at 3 Hz, to get images captured at
       1 Hz
end
sd = [  0.5 0.5 0.5;    %  5
        0.5 0.5 0.5;    % 15
        0.5 0.5 0.5;    % 20
        0.5 0.5 0.5;    % 30
        1.0 1.0 1.0;    % 40
        0.1 1.5 1.5;    % 50
        0.5 1.5 1.5;    % 60
        0.5 1.5 1.5;    % 75
        0.5 1.5 1.5;    % 90
        0.5 0.5 0.5;    % 100
        0.5 0.5 0.5;    % 120
        0.5 0.5 0.5;    % 150
    ];
factor = [  99.9 96.0 97.5;     %  5
            99.9 97.5 97.0;     % 15
            99.5 96.5 93.5;     % 20
            98.0 87.35 89.0;    % 30
            95.0 92.0 88.3;     % 40
            92.5 89.6 88.5;     % 50
            93.0 90.75 89.0;    % 60
            90.0 91.0 90.0;     % 75
            99.5 93.0 92.5;     % 90
            90.0 90.0 90.0;     % 100
            98.0 92.5 92.5;     % 120
            99.5 93.0 92.5;     % 150
    ];
%% Image Files
% Read
    % Background image
```

```
    I_bg = imread('B0001.tif');
    I_bg_double = double(I_bg); % double
        % Display background image
            i = i+1;
            f = figure(i);
            f.WindowStyle = 'docked';
            title({[num2str(Q_val) ' l/min Grayscale Background']});
            imagegray_bg = imshow(I_bg_double, []);
            impixelinfo;
    % Grayscale image
    size = 0;
    for n = 1:step:numfiles(Q_index)
        n
        if n == 1
            display = 1;
        else
            display = 0;
        end
        size = size + 1
        myfilename = sprintf('1 (%d).tif', n);
        I_raw(:,:,size) = imread(myfilename);
        I_raw_double = double(I_raw); % double
        % Display grayscale image
        if display == 1
            i = 1;
            f = figure(i);
            f.WindowStyle = 'docked';
            title({[num2str(Q_val) ' l/min Grayscale Raw']});
            imagegray_raw = imshow(I_raw_double, []);
            impixelinfo;
        end
% Crop
    I_raw_crop_1(:,:,size) = imcrop(I_raw_double(:,:,size),[42 296 1977
        815-296]);
    I_raw_crop_2(:,:,size) = imcrop(I_raw_double(:,:,size),[1 2679 2048
        3542-2679]);
    I_raw_crop_3(:,:,size) = imcrop(I_raw_double(:,:,size),[66 4937
       1794-66 5740-4937]);
    % Overlap
    I_raw_overlap_12_1(:,:,size) = imcrop(I_raw_double(:,:,size),[1978
       296 2048-1978 815-296]);
    I_raw_overlap_12_2(:,:,size) = imcrop(I_raw_double(:,:,size),[1
       2679 118-1 3542-2679]);
    I_raw_overlap_23_2(:,:,size) = imcrop(I_raw_double(:,:,size),[1977
       2678 2048 3542-2679]);
    I_raw_overlap_23_3(:,:,size) = imcrop(I_raw_double(:,:,size),[1
       4937 66-1 5740-4937]);
    % Background Image
    I_bg_crop_1 = imcrop(I_bg_double,[42 296 1977 815-296]); %
       Downstream
    I_bg_crop_2 = imcrop(I_bg_double,[1 2679 2048 3542-2679]); % Middle
```

```
I_bg_crop_3 = imcrop(I_bg_double,[66 4937 1794-66 5740-4937]); %
    Upstream
% Display
if display == 1
    % Grayscale Cropped
    i = i+1;
    f = figure(i);
    f.WindowStyle = 'docked';
    sgtitle({[num2str(Q_val) ' l/min Grayscale: Raw Cropped']});
    subplot(3,1,1);
        imshow(I_raw_crop_1(:,:,size), []);
        title('Downstream');
    subplot(3,1,2);
        imshow(I_raw_crop_2(:,:,size), []);
        title('Middle');
    subplot(3,1,3);
        imshow(I_raw_crop_3(:,:,size), []);
        title('Upstream');
    impixelinfo;
    fname_crop = sprintf('%d_Grayscale_Crop',Q_val);
    saveas(f,fname_crop);
    % Overlap
        % Group
        i = i+1;
        f = figure(i);
        f.WindowStyle = 'docked';
        sgtitle({[num2str(Q_val) ' l/min Grayscale: Overlap']});
        subplot(2,2,1);
            imshow(I_raw_overlap_12_1(:,:,size), []);
            title({'Downstream - Middle (in Downstream)'});
        subplot(2,2,3);
            imshow(I_raw_overlap_12_2(:,:,size), []);
            title({'Downstream - Middle in Middle'});
        subplot(2,2,2);
            imshow(I_raw_overlap_23_2(:,:,size), []);
            title({'Middle - Upstream (in Middle)'});
        subplot(2,2,4);
            imshow(I_raw_overlap_23_3(:,:,size), []);
            title({'Middle - Upstream (in Upstream)'});
        impixelinfo;
        % Individually
        condition = 0;
        if condition == 1
            i = i+1;
            f = figure(i);
            f.WindowStyle = 'docked';
            title({'Overlap: Downstream - Middle (in Downstream)'})
                ;
            imshow(I_raw_overlap_12_1(:,:,size), []);
            impixelinfo;
            i = i+1;
```

```
                f = figure(i);
                f.WindowStyle = 'docked';
                title({'Overlap: Downstream - Middle (in Middle)'})
                imshow(I_raw_overlap_12_2(:,:,size), []);
                impixelinfo;
                i = i+1;
                f = figure(i);
                f.WindowStyle = 'docked';
                title({'Overlap: Middle - Upstream (in Middle)'});
                imshow(I_raw_overlap_23_2(:,:,size), []);
                impixelinfo;
                i = i+1;
                f = figure(i);
                f.WindowStyle = 'docked';
                title({'Overlap: Middle - Upstream (in Upstream)'});
                imshow(I_raw_overlap_23_3(:,:,size), []);
                impixelinfo;
            end
        % Background Cropped
            i = i+1;
            f = figure(i);
            f.WindowStyle = 'docked';
            sgtitle({[num2str(Q_val) ' l/min Grayscale'],['Background
               Cropped']});
            subplot(3,1,1);
                imshow(I_bg_crop_1, []);
                title({'Downstream'});
            subplot(3,1,2);
                imshow(I_bg_crop_2, []);
                title({'Middle'});
            subplot(3,1,3);
                imshow(I_bg_crop_3, []);
                title({'Upstream'});
            impixelinfo;
    end
%%
% Normalise grayscale image with background image
    % Subtraction
    I_sub_1(:,:,size) = (I_raw_crop_1(:,:,size)-I_bg_crop_1);
    I_sub_2(:,:,size) = (I_raw_crop_2(:,:,size)-I_bg_crop_2);
    I_sub_3(:,:,size) = (I_raw_crop_3(:,:,size)-I_bg_crop_3);
%%
% Filter normalised image
    % Gaussian
        % Calculation
            % Subtraction
            I_sub_gaussfilt_1 = imgaussfilt(I_sub_1,sd(Q_index,1));
            I_sub_gaussfilt_2 = imgaussfilt(I_sub_2,sd(Q_index,2));
            I_sub_gaussfilt_3 = imgaussfilt(I_sub_3,sd(Q_index,3));
        % Display filtered grayscale image
        if display == 1
```

```
            % Subtraction
            i = i+1;
            f = figure(i);
            f.WindowStyle = 'docked';
            sgtitle({[num2str(Q_val) ' l/min Cropped Grayscale
               Normalised (I-BI)'],['Unfiltered - Gaussian Filtered']})
            subplot(3,2,1);
                imshow(I_sub_1, []);
                title('Downstream');
            subplot(3,2,3);
                imshow(I_sub_2, []);
                title('Middle');
            subplot(3,2,5);
                imshow(I_sub_3, []);
                title('Upstream');
            impixelinfo;
            subplot(3,2,2);
                imshow(I_sub_gaussfilt_1, []);
                title('Downstream');
            subplot(3,2,4);
                imshow(I_sub_gaussfilt_2, []);
                title('Middle');
            subplot(3,2,6);
                imshow(I_sub_gaussfilt_3, []);
                title('Upstream');
            impixelinfo;
        end
%%
% Convert grayscale image into binary image using thresholding
down = [98,104,104];
mid = [161,176];
up = [152,154,154];
    % Rescale to [0, 1] before thresholding
        % Subtraction
            % Unfiltered
            I_sscale_1(:,:,size) = rescale (I_sub_1(:,:,size));
            I_sscale_2(:,:,size) = rescale (I_sub_2(:,:,size));
            I_sscale_3(:,:,size) = rescale (I_sub_3(:,:,size));
            % Gaussian Filtered
                % Original
                I_sub_gauss_scale_1(:,:,size) = rescale(
                   I_sub_gaussfilt_1(:,:,size));
                I_sub_gauss_scale_2(:,:,size) = rescale(
                   I_sub_gaussfilt_2(:,:,size));
                I_sub_gauss_scale_3(:,:,size) = rescale(
                   I_sub_gaussfilt_3(:,:,size));
                % Corrected
                    % Downstream
                    I_sub_gaussfilt_1c_left(:,:,size) = cat(2,
                       I_sub_gaussfilt_1(:,1:down(1,1),size),
                       I_sub_gaussfilt_1(:,:,size));
```

```
                    I_sub_gaussfilt_1c_top(:,:,size) = cat(1,
                       I_sub_gaussfilt_1c_left(1:down(1,2),:,size),
                       I_sub_gaussfilt_1c_left(:,:,size));
                    I_sub_gaussfilt_1c(:,:,size) = cat(1,
                       I_sub_gaussfilt_1c_top(:,:,size),
                       I_sub_gaussfilt_1c_top(end-down(1,3)+1:end,:,
                       size));
                    % Middle
                    I_sub_gaussfilt_2c_top(:,:,size) = cat(1,
                       I_sub_gaussfilt_2(1:mid(1,1),:,size),
                       I_sub_gaussfilt_2(:,:,size));
                    I_sub_gaussfilt_2c(:,:,size) = cat(1,
                       I_sub_gaussfilt_2c_top(:,:,size),
                       I_sub_gaussfilt_2c_top(end-mid(1,2)+1:end,:,size
                       ));
                    % Upstream
                    I_sub_gaussfilt_3c_right(:,:,size) = cat(2,
                       I_sub_gaussfilt_3(:,:,size), I_sub_gaussfilt_3
                       (:,end-up(1,1)+1:end,size));
                    I_sub_gaussfilt_3c_top(:,:,size) = cat(1,
                       I_sub_gaussfilt_3c_right(1:up(1,2),:,size),
                       I_sub_gaussfilt_3c_right(:,:,size));
                    I_sub_gaussfilt_3c(:,:,size) = cat(1,
                       I_sub_gaussfilt_3c_top(:,:,size),
                       I_sub_gaussfilt_3c_top(end-up(1,3)+1:end,:,size)
                       );
                I_sub_gauss_scale_1c(:,:,size) = rescale(
                   I_sub_gaussfilt_1c(:,:,size));
                I_sub_gauss_scale_2c(:,:,size) = rescale(
                   I_sub_gaussfilt_2c(:,:,size));
                I_sub_gauss_scale_3c(:,:,size) = rescale(
                   I_sub_gaussfilt_3c(:,:,size));
    % Define threshold
        % Subtraction
            % Gaussian Filtered
                % Graythresh
                level_sg_gauss_1(size) = graythresh(I_sub_gauss_scale_1
                   (:,:,size));
                level_sg_gauss_2(size) = graythresh(I_sub_gauss_scale_2
                   (:,:,size));
                level_sg_gauss_3(size) = graythresh(I_sub_gauss_scale_3
                   (:,:,size));
                % Graythresh adjusted
                level_sg_gauss_adj_1(size) = graythresh(
                   I_sub_gauss_scale_1(:,:,size))/factor(Q_index,1)
                   *100;
                level_sg_gauss_adj_2(size) = graythresh(
                   I_sub_gauss_scale_2(:,:,size))/factor(Q_index,2)
                   *100;
                level_sg_gauss_adj_3(size) = graythresh(
                   I_sub_gauss_scale_3(:,:,size))/factor(Q_index,3)
```

```
                *100;
% Binarise {0,1}

    % Gaussian Filtered
        % Original
            % Definition
                % Graythresh
                I_sgbinary_gauss_1(:,:,size) = imbinarize(
                   I_sub_gauss_scale_1(:,:,size), level_sg_gauss_1(
                   size));
                I_sgbinary_gauss_2(:,:,size) = imbinarize(
                   I_sub_gauss_scale_2(:,:,size), level_sg_gauss_2(
                   size));
                I_sgbinary_gauss_3(:,:,size) = imbinarize(
                   I_sub_gauss_scale_3(:,:,size), level_sg_gauss_3(
                   size));
                % Graythresh Adjusted
                I_sgbinary_gauss_adj_1(:,:,size) = imbinarize(
                   I_sub_gauss_scale_1(:,:,size),
                   level_sg_gauss_adj_1(size));
                I_sgbinary_gauss_adj_2(:,:,size) = imbinarize(
                   I_sub_gauss_scale_2(:,:,size),
                   level_sg_gauss_adj_2(size));
                I_sgbinary_gauss_adj_3(:,:,size) = imbinarize(
                   I_sub_gauss_scale_3(:,:,size),
                   level_sg_gauss_adj_3(size));
            % Non-Wetted Area
                % Graythresh
                camera_1 = 1;
                camera_2 = 2;
                camera_3 = 3;
                nw_sg_gauss(size,camera_1) = nnz(~
                   I_sgbinary_gauss_1(:,:,size))./(nnz(
                   I_sgbinary_gauss_1(:,:,size))+nnz(~
                   I_sgbinary_gauss_1(:,:,size)))*100;
                nw_sg_gauss(size,camera_2) = nnz(~
                   I_sgbinary_gauss_2(:,:,size))./(nnz(
                   I_sgbinary_gauss_2(:,:,size))+nnz(~
                   I_sgbinary_gauss_2(:,:,size)))*100;
                nw_sg_gauss(size,camera_3) = nnz(~
                   I_sgbinary_gauss_3(:,:,size))./(nnz(
                   I_sgbinary_gauss_3(:,:,size))+nnz(~
                   I_sgbinary_gauss_3(:,:,size)))*100;
                nw_sg_gauss_tot(size,camera_3/3) = (nnz(~
                   I_sgbinary_gauss_1(:,:,size))+nnz(~
                   I_sgbinary_gauss_2(:,:,size))+nnz(~
                   I_sgbinary_gauss_3(:,:,size)))./((nnz(
                   I_sgbinary_gauss_1(:,:,size))+nnz(~
                   I_sgbinary_gauss_1(:,:,size)))+(nnz(
                   I_sgbinary_gauss_2(:,:,size))+nnz(~
                   I_sgbinary_gauss_2(:,:,size)))+(nnz(
```

```
                I_sgbinary_gauss_3(:,:,size))+nnz(
                I_sgbinary_gauss_3(:,:,size))))*100;
            % Graythresh Adjusted
            camera_adj_1 = 1;
            camera_adj_2 = 2;
            camera_adj_3 = 3;
            nw_sg_gauss_adj(size,camera_adj_1) = nnz(~
                I_sgbinary_gauss_adj_1(:,:,size))./(nnz(
                I_sgbinary_gauss_adj_1(:,:,size))+nnz(~
                I_sgbinary_gauss_adj_1(:,:,size)))*100;
            nw_sg_gauss_adj(size,camera_adj_2) = nnz(~
                I_sgbinary_gauss_adj_2(:,:,size))./(nnz(
                I_sgbinary_gauss_adj_2(:,:,size))+nnz(~
                I_sgbinary_gauss_adj_2(:,:,size)))*100;
            nw_sg_gauss_adj(size,camera_adj_3) = nnz(~
                I_sgbinary_gauss_adj_3(:,:,size))./(nnz(
                I_sgbinary_gauss_adj_3(:,:,size))+nnz(~
                I_sgbinary_gauss_adj_3(:,:,size)))*100;
            nw_sg_gauss_adj_tot(size,camera_adj_3/3) = (nnz(~
                I_sgbinary_gauss_adj_1(:,:,size))+nnz(~
                I_sgbinary_gauss_adj_2(:,:,size))+nnz(~
                I_sgbinary_gauss_adj_3(:,:,size))./((nnz(
                I_sgbinary_gauss_adj_1(:,:,size))+nnz(~
                I_sgbinary_gauss_adj_1(:,:,size)))+(nnz(
                I_sgbinary_gauss_adj_2(:,:,size))+nnz(~
                I_sgbinary_gauss_adj_2(:,:,size)))+(nnz(
                I_sgbinary_gauss_adj_3(:,:,size))+nnz(
                I_sgbinary_gauss_adj_3(:,:,size))))*100;
        % Display
        if display == 1
            % Subtraction
            i = i+1;
            f = figure(i);
            f.WindowStyle = 'docked';
            sgtitle({[num2str(Q_val) ' l/min Cropped Normalised
                Binary (I-BI)'],['Graythresh - Graythresh Adjusted'
                ]})
            subplot(3,2,1);
                imshow(I_sgbinary_gauss_1, []);
                title('Downstream');
            subplot(3,2,3);
                imshow(I_sgbinary_gauss_2, []);
                title('Middle');
            subplot(3,2,5);
                imshow(I_sgbinary_gauss_3, []);
                title('Upstream');
            impixelinfo;
            subplot(3,2,2);
                imshow(I_sgbinary_gauss_adj_1, []);
                title('Downstream');
            subplot(3,2,4);
```

```
                imshow(I_sgbinary_gauss_adj_2, []);
                title('Middle');
            subplot(3,2,6);
                imshow(I_sgbinary_gauss_adj_3, []);
                title('Upstream');
            impixelinfo;
        end
%%
% Invert (holes are areas of dark pixels surrounded by light pixels)
    % Gaussian Filtered
        % Original
            % Definition
                % Graythresh
                I_sgbinary_gauss_inv_1(:,:,size) = ~I_sgbinary_gauss_1
                    (:,:,size);
                I_sgbinary_gauss_inv_2(:,:,size) = ~I_sgbinary_gauss_2
                    (:,:,size);
                I_sgbinary_gauss_inv_3(:,:,size) = ~I_sgbinary_gauss_3
                    (:,:,size);
                % Graythresh adjusted
                I_sgbinary_gauss_adj_inv_1(:,:,size) = ~
                    I_sgbinary_gauss_adj_1(:,:,size);
                I_sgbinary_gauss_adj_inv_2(:,:,size) = ~
                    I_sgbinary_gauss_adj_2(:,:,size);
                I_sgbinary_gauss_adj_inv_3(:,:,size) = ~
                    I_sgbinary_gauss_adj_3(:,:,size);
%%
% Bridge Gaps
    % Gaussian Filtered
        % Original
            % Definition
                % Graythresh
                J_sgbinary_gauss_inv_1(:,:,size) = bwmorph(
                    I_sgbinary_gauss_inv_1(:,:,size),'bridge');
                J_sgbinary_gauss_inv_2(:,:,size) = bwmorph(
                    I_sgbinary_gauss_inv_2(:,:,size),'bridge');
                J_sgbinary_gauss_inv_3(:,:,size) = bwmorph(
                    I_sgbinary_gauss_inv_3(:,:,size),'bridge');
                % Graythresh adjusted
                J_sgbinary_gauss_adj_inv_1(:,:,size) = bwmorph(
                    I_sgbinary_gauss_adj_inv_1(:,:,size),'bridge');
                J_sgbinary_gauss_adj_inv_2(:,:,size) = bwmorph(
                    I_sgbinary_gauss_adj_inv_2(:,:,size),'bridge');
                J_sgbinary_gauss_adj_inv_3(:,:,size) = bwmorph(
                    I_sgbinary_gauss_adj_inv_3(:,:,size),'bridge');
            % Non-Wetted Area
                % Graythresh
                camera_1 = camera_1+3;
                camera_2 = camera_2+3;
                camera_3 = camera_3+3;
                nw_sg_gauss(size,camera_1) = nnz(J_sgbinary_gauss_inv_1
```

```
                    (:,:,size))./(nnz(J_sgbinary_gauss_inv_1(:,:,size))+
                    nnz(~J_sgbinary_gauss_inv_1(:,:,size)))*100;
                nw_sg_gauss(size,camera_2) = nnz(J_sgbinary_gauss_inv_2
                    (:,:,size))./(nnz(J_sgbinary_gauss_inv_2(:,:,size))+
                    nnz(~J_sgbinary_gauss_inv_2(:,:,size)))*100;
                nw_sg_gauss(size,camera_3) = nnz(J_sgbinary_gauss_inv_3
                    (:,:,size))./(nnz(J_sgbinary_gauss_inv_3(:,:,size))+
                    nnz(~J_sgbinary_gauss_inv_3(:,:,size)))*100;
                nw_sg_gauss_tot(size,camera_3/3) = (nnz(
                    J_sgbinary_gauss_inv_1(:,:,size))+nnz(
                    J_sgbinary_gauss_inv_2(:,:,size))+nnz(
                    J_sgbinary_gauss_inv_3(:,:,size))./((nnz(
                    J_sgbinary_gauss_inv_1(:,:,size))+nnz(~
                    J_sgbinary_gauss_inv_1(:,:,size)))+(nnz(
                    J_sgbinary_gauss_inv_2(:,:,size))+nnz(~
                    J_sgbinary_gauss_inv_2(:,:,size)))+(nnz(
                    J_sgbinary_gauss_inv_3(:,:,size))+nnz(
                    J_sgbinary_gauss_inv_3(:,:,size))))*100;
                % Graythresh Adjusted
                camera_adj_1 = camera_adj_1+3;
                camera_adj_2 = camera_adj_2+3;
                camera_adj_3 = camera_adj_3+3;
                nw_sg_gauss_adj(size,camera_adj_1) = nnz(
                    J_sgbinary_gauss_adj_inv_1(:,:,size))./(nnz(
                    J_sgbinary_gauss_adj_inv_1(:,:,size))+nnz(~
                    J_sgbinary_gauss_adj_inv_1(:,:,size)))*100;
                nw_sg_gauss_adj(size,camera_adj_2) = nnz(
                    J_sgbinary_gauss_adj_inv_2(:,:,size))./(nnz(
                    J_sgbinary_gauss_adj_inv_2(:,:,size))+nnz(~
                    J_sgbinary_gauss_adj_inv_2(:,:,size)))*100;
                nw_sg_gauss_adj(size,camera_adj_3) = nnz(
                    J_sgbinary_gauss_adj_inv_3(:,:,size))./(nnz(
                    J_sgbinary_gauss_adj_inv_3(:,:,size))+nnz(~
                    J_sgbinary_gauss_adj_inv_3(:,:,size)))*100;
                nw_sg_gauss_adj_tot(size,camera_adj_3/3) = (nnz(
                    J_sgbinary_gauss_adj_inv_1(:,:,size))+nnz(
                    J_sgbinary_gauss_adj_inv_2(:,:,size))+nnz(
                    J_sgbinary_gauss_adj_inv_3(:,:,size))./((nnz(
                    J_sgbinary_gauss_adj_inv_1(:,:,size))+nnz(~
                    J_sgbinary_gauss_adj_inv_1(:,:,size)))+(nnz(
                    J_sgbinary_gauss_adj_inv_2(:,:,size))+nnz(~
                    J_sgbinary_gauss_adj_inv_2(:,:,size)))+(nnz(
                    J_sgbinary_gauss_adj_inv_3(:,:,size))+nnz(
                    J_sgbinary_gauss_adj_inv_3(:,:,size))))*100;
%%
% Fill
    % Gaussian Filtered
        % Original
            % Definition
                % Graythresh
                    % Simple
```

```
                % Unmodified
                J_sgbinary_gauss_fill_1(:,:,size) = imfill(
                    J_sgbinary_gauss_inv_1(:,:,size), "holes");
                J_sgbinary_gauss_fill_2(:,:,size) = imfill(
                    J_sgbinary_gauss_inv_2(:,:,size), "holes");
                J_sgbinary_gauss_fill_3(:,:,size) = imfill(
                    J_sgbinary_gauss_inv_3(:,:,size), "holes");
            % Graythresh adjusted
                % Simple
                % Unmodified
                J_sgbinary_gauss_adj_fill_1(:,:,size) = imfill(
                    J_sgbinary_gauss_adj_inv_1(:,:,size), "holes
                    ");
                J_sgbinary_gauss_adj_fill_2(:,:,size) = imfill(
                    J_sgbinary_gauss_adj_inv_2(:,:,size), "holes
                    ");
                J_sgbinary_gauss_adj_fill_3(:,:,size) = imfill(
                    J_sgbinary_gauss_adj_inv_3(:,:,size), "holes
                    ");
        % Non-wetted area
            % Graythresh
                % Simple
                % Unmodified
                camera_1 = camera_1+3;
                camera_2 = camera_2+3;
                camera_3 = camera_3+3;
                nw_sg_gauss(size,camera_1) = nnz(
                    J_sgbinary_gauss_fill_1(:,:,size))./(nnz(
                    J_sgbinary_gauss_fill_1(:,:,size))+nnz(~
                    J_sgbinary_gauss_fill_1(:,:,size)))*100;
                nw_sg_gauss(size,camera_2) = nnz(
                    J_sgbinary_gauss_fill_2(:,:,size))./(nnz(
                    J_sgbinary_gauss_fill_2(:,:,size))+nnz(~
                    J_sgbinary_gauss_fill_2(:,:,size)))*100;
                nw_sg_gauss(size,camera_3) = nnz(
                    J_sgbinary_gauss_fill_3(:,:,size))./(nnz(
                    J_sgbinary_gauss_fill_3(:,:,size))+nnz(~
                    J_sgbinary_gauss_fill_3(:,:,size)))*100;
                nw_sg_gauss_tot(size,camera_3/3) = (nnz(
                    J_sgbinary_gauss_fill_1(:,:,size))+nnz(
                    J_sgbinary_gauss_fill_2(:,:,size))+nnz(
                    J_sgbinary_gauss_fill_3(:,:,size)))./((nnz(
                    J_sgbinary_gauss_fill_1(:,:,size))+nnz(~
                    J_sgbinary_gauss_fill_1(:,:,size)))+(nnz(
                    J_sgbinary_gauss_fill_2(:,:,size))+nnz(~
                    J_sgbinary_gauss_fill_2(:,:,size)))+(nnz(
                    J_sgbinary_gauss_fill_3(:,:,size))+nnz(~
                    J_sgbinary_gauss_fill_3(:,:,size))))*100;
            % Graythresh adjusted
                % Simple
                % Unmodified
```

```
                camera_adj_1 = camera_adj_1+3;
                camera_adj_2 = camera_adj_2+3;
                camera_adj_3 = camera_adj_3+3;
                nw_sg_gauss_adj(size,camera_adj_1) = nnz(
                   J_sgbinary_gauss_adj_fill_1(:,:,size))./(nnz
                   (J_sgbinary_gauss_adj_fill_1(:,:,size))+nnz
                   (~J_sgbinary_gauss_adj_fill_1(:,:,size)))
                   *100;
                nw_sg_gauss_adj(size,camera_adj_2) = nnz(
                   J_sgbinary_gauss_adj_fill_2(:,:,size))./(nnz
                   (J_sgbinary_gauss_adj_fill_2(:,:,size))+nnz
                   (~J_sgbinary_gauss_adj_fill_2(:,:,size)))
                   *100;
                nw_sg_gauss_adj(size,camera_adj_3) = nnz(
                   J_sgbinary_gauss_adj_fill_3(:,:,size))./(nnz
                   (J_sgbinary_gauss_adj_fill_3(:,:,size))+nnz
                   (~J_sgbinary_gauss_adj_fill_3(:,:,size)))
                   *100;
                nw_sg_gauss_adj_tot(size,camera_adj_3/3) = (nnz
                   (J_sgbinary_gauss_adj_fill_1(:,:,size))+nnz(
                   J_sgbinary_gauss_adj_fill_2(:,:,size))+nnz(
                   J_sgbinary_gauss_adj_fill_3(:,:,size))./((
                   nnz(J_sgbinary_gauss_adj_fill_1(:,:,size))+
                   nnz(~J_sgbinary_gauss_adj_fill_1(:,:,size)))
                   +(nnz(J_sgbinary_gauss_adj_fill_2(:,:,size))
                   +nnz(~J_sgbinary_gauss_adj_fill_2(:,:,size))
                   )+(nnz(J_sgbinary_gauss_adj_fill_3(:,:,size)
                   )+nnz(~J_sgbinary_gauss_adj_fill_3(:,:,size)
                   )))*100;
% Display
if display == 1
    % Original
        % Graythresh
            % Unmodified
            i = i+1;
            f = figure(i);
            f.WindowStyle = 'docked';
            sgtitle({[num2str(Q_val) ' l/min Gaussian
               Filtered Graythresh Inverted Binary (I-BI)
               Bridged Filled'],['Simple']});
            subplot(3,1,1);
                imshow(J_sgbinary_gauss_fill_1(:,:,size),
                   []);
                title('Downstream');
            subplot(3,1,2);
                imshow(J_sgbinary_gauss_fill_2(:,:,size),
                   []);
                title('Middle');
            subplot(3,1,3);
                imshow(J_sgbinary_gauss_fill_3(:,:,size),
                   []);
```

```
                    title('Upstream');
                impixelinfo;
            % Graythresh adjusted
                % Unmodified
                i = i+1;
                f = figure(i);
                f.WindowStyle = 'docked';
                sgtitle({[num2str(Q_val) ' l/min Gaussian
                    Filtered Graythresh Adjusted Inverted Binary
                    (I-BI) Bridged Filled'],['Simple']});
                subplot(3,1,1);
                    imshow(J_sgbinary_gauss_adj_fill_1(:,:,size
                        ), []);
                    title('Downstream');
                subplot(3,1,2);
                    imshow(J_sgbinary_gauss_adj_fill_2(:,:,size
                        ), []);
                    title('Middle');
                subplot(3,1,3);
                    imshow(J_sgbinary_gauss_adj_fill_3(:,:,size
                        ), []);
                    title('Upstream');
                impixelinfo;
        end

    % Corrected
        % Definition
            % Graythresh
                % Simple
                    % Downstream
                    J_sgbinary_gauss_fill_1c_left(:,:,size) = cat
                        (2, J_sgbinary_gauss_fill_1(:,1:down(1,1),
                        size), J_sgbinary_gauss_fill_1(:,:,size));
                    J_sgbinary_gauss_fill_1c_top(:,:,size) = cat(1,
                        J_sgbinary_gauss_fill_1c_left(1:down(1,2)
                        ,:,size), J_sgbinary_gauss_fill_1c_left(:,:,
                        size));
                    J_sgbinary_gauss_fill_1c(:,:,size) = cat(1,
                        J_sgbinary_gauss_fill_1c_top(:,:,size),
                        J_sgbinary_gauss_fill_1c_top(end-down(1,3)
                        +1:end,:,size));
                    % Middle
                    J_sgbinary_gauss_fill_2c_top(:,:,size) = cat(1,
                        J_sgbinary_gauss_fill_2(1:mid(1,1),:,size),
                        J_sgbinary_gauss_fill_2(:,:,size));
                    J_sgbinary_gauss_fill_2c(:,:,size) = cat(1,
                        J_sgbinary_gauss_fill_2c_top(:,:,size),
                        J_sgbinary_gauss_fill_2c_top(end-mid(1,2)+1:
                        end,:,size));
                    % Upstream
                    J_sgbinary_gauss_fill_3c_right(:,:,size) = cat
```

```
                    (2, J_sgbinary_gauss_fill_3(:,:,size),
                    J_sgbinary_gauss_fill_3(:,end-up(1,1)+1:end,
                    size));
                J_sgbinary_gauss_fill_3c_top(:,:,size) = cat(1,
                     J_sgbinary_gauss_fill_3c_right(1:up(1,2),:,
                    size), J_sgbinary_gauss_fill_3c_right(:,:,
                    size));
                J_sgbinary_gauss_fill_3c(:,:,size) = cat(1,
                    J_sgbinary_gauss_fill_3c_top(:,:,size),
                    J_sgbinary_gauss_fill_3c_top(end-up(1,3)+1:
                    end,:,size));
            % Graythresh adjusted
                % Simple
                    % Downstream
                    J_sgbinary_gauss_adj_fill_1c_left(:,:,size) =
                        cat(2, J_sgbinary_gauss_adj_fill_1(:,1:down
                        (1,1),size), J_sgbinary_gauss_adj_fill_1
                        (:,:,size));
                    J_sgbinary_gauss_adj_fill_1c_top(:,:,size) =
                        cat(1, J_sgbinary_gauss_adj_fill_1c_left(1:
                        down(1,2),:,size),
                        J_sgbinary_gauss_adj_fill_1c_left(:,:,size))
                        ;
                    J_sgbinary_gauss_adj_fill_1c(:,:,size) = cat(1,
                         J_sgbinary_gauss_adj_fill_1c_top(:,:,size),
                         J_sgbinary_gauss_adj_fill_1c_top(end-down
                        (1,3)+1:end,:,size));
                    % Middle
                    J_sgbinary_gauss_adj_fill_2c_top(:,:,size) =
                        cat(1, J_sgbinary_gauss_adj_fill_2(1:mid
                        (1,1),:,size), J_sgbinary_gauss_adj_fill_2
                        (:,:,size));
                    J_sgbinary_gauss_adj_fill_2c(:,:,size) = cat(1,
                         J_sgbinary_gauss_adj_fill_2c_top(:,:,size),
                         J_sgbinary_gauss_adj_fill_2c_top(end-mid
                        (1,2)+1:end,:,size));
                    % Upstream
                    J_sgbinary_gauss_adj_fill_3c_right(:,:,size) =
                        cat(2, J_sgbinary_gauss_adj_fill_3(:,:,size)
                        , J_sgbinary_gauss_adj_fill_3(:,end-up(1,1)
                        +1:end,size));
                    J_sgbinary_gauss_adj_fill_3c_top(:,:,size) =
                        cat(1, J_sgbinary_gauss_adj_fill_3c_right(1:
                        up(1,2),:,size),
                        J_sgbinary_gauss_adj_fill_3c_right(:,:,size)
                        );
                    J_sgbinary_gauss_adj_fill_3c(:,:,size) = cat(1,
                         J_sgbinary_gauss_adj_fill_3c_top(:,:,size),
                         J_sgbinary_gauss_adj_fill_3c_top(end-up
                        (1,3)+1:end,:,size));
        % Non-wetted area
```

```
% Graythresh
    % Simple
        % Unmodified
        camera_1c = 1;
        camera_2c = 2;
        camera_3c = 3;
        nw_sg_gauss_corr(size,camera_1c) = nnz(
           J_sgbinary_gauss_fill_1c(:,:,size))./(nnz(
           J_sgbinary_gauss_fill_1c(:,:,size))+nnz(~
           J_sgbinary_gauss_fill_1c(:,:,size)))*100;
        nw_sg_gauss_corr(size,camera_2c) = nnz(
           J_sgbinary_gauss_fill_2c(:,:,size))./(nnz(
           J_sgbinary_gauss_fill_2c(:,:,size))+nnz(~
           J_sgbinary_gauss_fill_2c(:,:,size)))*100;
        nw_sg_gauss_corr(size,camera_3c) = nnz(
           J_sgbinary_gauss_fill_3c(:,:,size))./(nnz(
           J_sgbinary_gauss_fill_3c(:,:,size))+nnz(~
           J_sgbinary_gauss_fill_3c(:,:,size)))*100;
        nw_sg_gauss_tot_corr(size,camera_3c/3) = (nnz(
           J_sgbinary_gauss_fill_1c(:,:,size))+nnz(
           J_sgbinary_gauss_fill_2c(:,:,size))+nnz(
           J_sgbinary_gauss_fill_3c(:,:,size))./((nnz(
           J_sgbinary_gauss_fill_1c(:,:,size))+nnz(~
           J_sgbinary_gauss_fill_1c(:,:,size)))+(nnz(
           J_sgbinary_gauss_fill_2c(:,:,size))+nnz(~
           J_sgbinary_gauss_fill_2c(:,:,size)))+(nnz(
           J_sgbinary_gauss_fill_3c(:,:,size))+nnz(~
           J_sgbinary_gauss_fill_3c(:,:,size))))*100;
% Graythresh adjusted
    % Simple
        % Unmodified
        camera_adj_1c = 1;
        camera_adj_2c = 2;
        camera_adj_3c = 3;
        nw_sg_gauss_adj_corr(size,camera_adj_1c) = nnz(
           J_sgbinary_gauss_adj_fill_1c(:,:,size))./(
           nnz(J_sgbinary_gauss_adj_fill_1c(:,:,size))+
           nnz(~J_sgbinary_gauss_adj_fill_1c(:,:,size))
           )*100;
        nw_sg_gauss_adj_corr(size,camera_adj_2c) = nnz(
           J_sgbinary_gauss_adj_fill_2c(:,:,size))./(
           nnz(J_sgbinary_gauss_adj_fill_2c(:,:,size))+
           nnz(~J_sgbinary_gauss_adj_fill_2c(:,:,size))
           )*100;
        nw_sg_gauss_adj_corr(size,camera_adj_3c) = nnz(
           J_sgbinary_gauss_adj_fill_3c(:,:,size))./(
           nnz(J_sgbinary_gauss_adj_fill_3c(:,:,size))+
           nnz(~J_sgbinary_gauss_adj_fill_3c(:,:,size))
           )*100;
        nw_sg_gauss_adj_tot_corr(size,camera_adj_3c/3)
           = (nnz(J_sgbinary_gauss_adj_fill_1c(:,:,size
```

```
                    ))+nnz(J_sgbinary_gauss_adj_fill_2c(:,:,size
                    ))+nnz(J_sgbinary_gauss_adj_fill_3c(:,:,size
                    ))))./((nnz(J_sgbinary_gauss_adj_fill_1c(:,:,
                    size))+nnz(~J_sgbinary_gauss_adj_fill_1c
                    (:,:,size)))+(nnz(
                    J_sgbinary_gauss_adj_fill_2c(:,:,size))+nnz
                    (~J_sgbinary_gauss_adj_fill_2c(:,:,size)))+(
                    nnz(J_sgbinary_gauss_adj_fill_3c(:,:,size))+
                    nnz(~J_sgbinary_gauss_adj_fill_3c(:,:,size))
                    ))*100;
% Display
if display == 1
    % Corrected
        % Graythresh
            % Unmodified
            i = i+1;
            f = figure(i);
            f.WindowStyle = 'docked';
            sgtitle({[num2str(Q_val) ' l/min Gaussian
               Filtered Graythresh Binary (I-BI) Bridged
               Filled Corrected'],['Simple']});
            subplot(3,1,1);
                imshow(J_sgbinary_gauss_fill_1c(:,:,size),
                   []);
                title('Downstream');
            subplot(3,1,2);
                imshow(J_sgbinary_gauss_fill_2c(:,:,size),
                   []);
                title('Middle');
            subplot(3,1,3);
                imshow(J_sgbinary_gauss_fill_3c(:,:,size),
                   []);
                title('Upstream');
            impixelinfo;
        % Graythresh adjusted
            % Unmodified
            i = i+1;
            f = figure(i);
            f.WindowStyle = 'docked';
            sgtitle({[num2str(Q_val) ' l/min Gaussian
               Filtered Graythresh Adjusted Inverted Binary
                (I-BI) Bridged Filled Corrected'],['Simple'
               ]});
            subplot(3,1,1);
                imshow(J_sgbinary_gauss_adj_fill_1c(:,:,
                   size), []);
                title('Downstream');
            subplot(3,1,2);
                imshow(J_sgbinary_gauss_adj_fill_2c(:,:,
                   size), []);
                title('Middle');
```

```
                    subplot(3,1,3);
                        imshow(J_sgbinary_gauss_adj_fill_3c(:,:,
                            size), []);
                        title('Upstream');
                    impixelinfo;
        end
    % Overlay
    if display == 1
        % Original
            % Definition
                % Downstream
                stringArray = repmat("water",height(
                    J_sgbinary_gauss_adj_fill_1(:,:,size)),length(
                    J_sgbinary_gauss_adj_fill_1(:,:,size)));
                stringArray(J_sgbinary_gauss_adj_fill_1(:,:,size))
                    = "bubble";
                categoricalSegmentation = categorical(stringArray);
                J_overlay_1 = labeloverlay(I_sub_gauss_scale_1(:,:,
                    size),categoricalSegmentation,'IncludedLabels',"
                    bubble",'Colormap','autumn','Transparency',0.8);
                % Middle
                stringArray = repmat("water",height(
                    J_sgbinary_gauss_adj_fill_2(:,:,size)),length(
                    J_sgbinary_gauss_adj_fill_2(:,:,size)));
                stringArray(J_sgbinary_gauss_adj_fill_2(:,:,size))
                    = "bubble";
                categoricalSegmentation = categorical(stringArray);
                J_overlay_2 = labeloverlay(I_sub_gauss_scale_2(:,:,
                    size),categoricalSegmentation,'IncludedLabels',"
                    bubble",'Colormap','autumn','Transparency',0.8);
                % Upstream
                stringArray = repmat("water",height(
                    J_sgbinary_gauss_adj_fill_3(:,:,size)),length(
                    J_sgbinary_gauss_adj_fill_3(:,:,size)));
                stringArray(J_sgbinary_gauss_adj_fill_3(:,:,size))
                    = "bubble";
                categoricalSegmentation = categorical(stringArray);
                J_overlay_3 = labeloverlay(I_sub_gauss_scale_3(:,:,
                    size),categoricalSegmentation,'IncludedLabels',"
                    bubble",'Colormap','autumn','Transparency',0.8);
            % Display
            i = i+1;
            f = figure(i);
            f.WindowStyle = 'docked';
            imshow(J_overlay_1, []);
            title({[num2str(Q_val) ' l/min Overlay (Original)'],['
                Downstream']});
            subtitle('Downstream')
            impixelinfo;
            i = i+1;
            f = figure(i);
```

```
        f.WindowStyle = 'docked';
        imshow(J_overlay_2, []);
        title({[num2str(Q_val) ' l/min Overlay (Original)'],['
            Middle']});
        subtitle('Middle')
        impixelinfo;
        i = i+1;
        f = figure(i);
        f.WindowStyle = 'docked';
        imshow(J_overlay_3, []);
        title({[num2str(Q_val) ' l/min Overlay (Original)'],['
            Upstream']});
        subtitle('Upstream')
        impixelinfo;
    % Corrected
        % Definition
            % Downstream
            stringArray = repmat("water",height(
                J_sgbinary_gauss_adj_fill_1c(:,:,size)),length(
                J_sgbinary_gauss_adj_fill_1c(:,:,size)));
            stringArray(J_sgbinary_gauss_adj_fill_1c(:,:,size))
                = "bubble";
            categoricalSegmentation = categorical(stringArray);
            J_overlay_1c = labeloverlay(I_sub_gauss_scale_1c
                (:,:,size),categoricalSegmentation,'
                IncludedLabels',"bubble",'Colormap','autumn','
                Transparency',0.8);
            % Middle
            stringArray = repmat("water",height(
                J_sgbinary_gauss_adj_fill_2c(:,:,size)),length(
                J_sgbinary_gauss_adj_fill_2c(:,:,size)));
            stringArray(J_sgbinary_gauss_adj_fill_2c(:,:,size))
                = "bubble";
            categoricalSegmentation = categorical(stringArray);
            J_overlay_2c = labeloverlay(I_sub_gauss_scale_2c
                (:,:,size),categoricalSegmentation,'
                IncludedLabels',"bubble",'Colormap','autumn','
                Transparency',0.8);
            % Upstream
            stringArray = repmat("water",height(
                J_sgbinary_gauss_adj_fill_3c(:,:,size)),length(
                J_sgbinary_gauss_adj_fill_3c(:,:,size)));
            stringArray(J_sgbinary_gauss_adj_fill_3c(:,:,size))
                = "bubble";
            categoricalSegmentation = categorical(stringArray);
            J_overlay_3c = labeloverlay(I_sub_gauss_scale_3c
                (:,:,size),categoricalSegmentation,'
                IncludedLabels',"bubble",'Colormap','autumn','
                Transparency',0.8);
        % Display
        i = i+1;
```

```
                f = figure(i);
                f.WindowStyle = 'docked';
                imshow(J_overlay_1c, []);
                title({[num2str(Q_val) ' l/min Overlay (Corrected)'],['
                    Downstream']});
                subtitle('Downstream')
                impixelinfo;
                i = i+1;
                f = figure(i);
                f.WindowStyle = 'docked';
                imshow(J_overlay_2c, []);
                title({[num2str(Q_val) ' l/min Overlay (Corrected)'],['
                    Middle']});
                subtitle('Middle')
                impixelinfo;
                i = i+1;
                f = figure(i);
                f.WindowStyle = 'docked';
                imshow(J_overlay_3c, []);
                title({[num2str(Q_val) ' l/min Overlay (Corrected)'],['
                    Upstream']});
                subtitle('Upstream')
                impixelinfo;
        end
    end
%% Cumulative Mean
% Definition
    % Original
    nw_cum_mean = cumsum(nw_sg_gauss_adj_tot,1)./(1:numel(
        nw_sg_gauss_adj_tot(1:size,1)))'; % row-wise sum
    % Corrected
    nw_cum_mean_corr = cumsum(nw_sg_gauss_adj_tot_corr,1)./(1:numel(
        nw_sg_gauss_adj_tot_corr(1:size,1)))'; % row-wise sum
% Plot
    fontsize = 23;
    labelsize = 30;
    legendsize = 23;
            i = i+1;
            f = figure(i);
            f.WindowStyle = 'docked';
            plot(1:height(nw_cum_mean_corr),nw_cum_mean_corr(:,1), '-',
                'LineWidth', 0.1, 'Marker', '.', 'MarkerSize', 10, '
                DisplayName', ['Q = ' num2str(Q_val) ' l/min'])
            grid on;
            xlabel({'';'$$n$$ [-]'},'FontSize',labelsize,'interpreter',
                'latex');
            ylabel({'$$A_{nw}/A_{w}$$ [$$\%$$]';'\textrm{(downstream of
                injection slot)}';''},'FontSize',labelsize,'interpreter
                ','latex');
            legend('Location','best');
            ax = gca;
```

```
ax.PositionConstraint = "outerposition";
ax.XAxis.FontSize = fontsize;
ax.YAxis.FontSize = fontsize;
ax.XLabel.FontSize = labelsize;
ax.YLabel.FontSize = labelsize;
ax.Title.FontSize = 30;
ax.Legend.FontSize = legendsize;

i = i+1;
f = figure(i);
f.WindowStyle = 'docked';
plot(1:height(nw_sg_gauss_adj_corr),nw_sg_gauss_adj_corr
   (:,1), '-', 'LineWidth', 1, 'Marker', 'o', 'MarkerSize',
    5, 'DisplayName', 'Downstream');
hold on
plot(1:height(nw_sg_gauss_adj_corr),nw_sg_gauss_adj_corr
   (:,2), '-', 'LineWidth', 1, 'Marker', 'o', 'MarkerSize',
    5, 'DisplayName', 'Middle');
hold on
plot(1:height(nw_sg_gauss_adj_corr),nw_sg_gauss_adj_corr
   (:,3), '-', 'LineWidth', 1, 'Marker', 'o', 'MarkerSize',
    5, 'DisplayName', 'Upstream');
grid on;
xlabel({'$$n$$ [-]'},'interpreter','latex');
ylabel({'$$A_{nw}/A_{w} \textrm{(downstream of injection
   slot)}$$ [$$\%$$]'},'interpreter','latex');
legend('Location','best');
ax = gca;
ax.PositionConstraint = "outerposition";
ax.XAxis.FontSize = 15;
ax.YAxis.FontSize = 15;
ax.XLabel.FontSize = 24;
ax.YLabel.FontSize = 24;
ax.Title.FontSize = 30;
ax.Legend.FontSize = 15;
```

# References


ITTC. Proceedings. In *13th International Towing Tank Conference*, volume 1. 1972. [Cited on page 1]

McCormick, M. E. and Bhattacharya. Drag reduction on a submersible hull by electrolysis. *Naval Engineers Journal*, 85:11–16, 1973. [Cited on pages 7, 8, 9, 12, and 16]

Sclichting, H. *Boundary Layer Theory*. McGraw-Hill Book Company, 1979. [Cited on pages 5 and 7]

Madavan, N. K., Deutsch, S., and Merkle, C. L. Reduction of turbulent skin friction by microbubbles. *Physics of Fluids*, 27:356–363, 1984. [Cited on pages 8, 9, 12, and 16]

White, F. M. *Viscous Fluid Flow*. McGraw-Hill, 1991. [Cited on page 10]

Grigson, C. W. B. An Accurate Smooth Friction Line for Use in Performance Prediction. *Transactions of the Royal Institution of Naval Architects*, 135:149–162, 1992. [Cited on page 7]

International Towing Tank Conference. Testing and Extrapolation Methods Resistance Uncertainty Analysis Example for Resistance Test. *ITTC - Recommended Procedures and Guidelines 7.5-02-02-02*, 2002. [Cited on pages 16, 22, 37, and 47]

Woud, H. K. and Stapersma, D. *Design of Propulsion and Elecric Power Generation Systems*. The Institute of Marine Engineering, Science and Technology, 2002. [Cited on page 1]

Katsui, T., Asai, H., Himeno, Y., and Tahara, Y. The Proposal of a New Friction Line. In *Fifth Osaka Colloquium on Advanced CFD Applications to Ship Flow and Hull Form Design*. Osaka, Japan, 2005. [Cited on page 7]

Lu, J., Fernández, A., and Tryggvason, G. The effect of bubbles on the wall drag in a turbulent channel flow. *Physics of Fluids*, 17:095102–1 – 095102–12, 2005. [Cited on pages vi, 9, 10, 12, and 43]

International Towing Tank Conference. Testing and Extrapolation Methods, General Density and Viscosity of Water. *ITTC - Recommended Procedures and Guidelines 7.5-02-01-03*, 2006. [Cited on pages 23 and 38]

Sanders, W. C., Winkel, E. S., Dowling, D. R., Perlin, M., and Ceccio, S. L. Bubble friction drag reduction in a high-Reynolds-number flat-plate turbulent boundary layer. *Journal of Fluid Mechanics*, 552:353–380, 2006. [Cited on pages vi, 3, 9, 10, 11, 12, and 16]

Elbing, B. R., Winkel, E. S., Lay, K. A., Ceccio, S. L., Dowling, D. R., and Perlin, M. Bubble-induced skin-friction drag reduction and the abrupt transition to air-layer drag reduction. *Journal of Fluid Mechnanics*, 612:201–236, 2008. [Cited on pages 2, 12, 13, 14, 16, 17, 23, and 42]

Lay, K. A., Elbing, B. R., Yakushiji, R., Perlin, M., and Ceccio, S. L. Skin-Friction Drag Reduction by Air Layers and Partial Cavities. In *27th Symposium on Naval Hydrodynamics*, pages 5–10. 2008. [Cited on page 16]

Beer, F. P., E. Russel Johnston, J., DeWolf, J. T., and Mazzurek, D. F. *Mechanics of Materials*. McGrawHill, 2009. [Cited on page 24]

Bertin, J. J. and Cummings, R. M. *Aerodynamics for Engineers*. Pearson Education International, 2009. [Cited on page 6]

Larsson, L., Raven, H. C., and Paulling, J. R. *Ship Resistance and Flow*. Society of Naval Architects and Marine Engineers, 2010. [Cited on page 1]

Mäkiharju, S. A., Perlin, M., and Ceccio, S. L. On the energy economics of air lubrication drag reduction. *International Journal of Naval Architecture and Ocean Engineering*, 4:412–422, 2012. [Cited on page 2]

Murai, Y. Frictional drag reduction by bubble injection. *Experiments in FLuids: Experimental Methods and their Applications to Fluid Flow*, 55(1773):1–28, 2014. [Cited on pages vi, 9, 11, and 12]

Zverkhovskyi, O. *Ship Drag Reduction by Air Cavities*. Ph.D. thesis, Delft University of Technology, 2014. [Cited on pages vi, 2, 3, 14, 15, 16, and 42]

Rotte, G., Zverkhovskyi, O., Kerkvliet, M., and van Terwisga, T. On the physical mechanisms for the numerical modelling of flows around air lubricated ships. In *Proceedings of the 12th International Conference on Hydrodynamics*. 2016. [Cited on page 2]

White, F. M. *Fluid Mechanics*. McGraw-Hill, 2016. [Cited on page 7]

ITTC. Uncertainty Analysis, Instrument Calibration. *ITTC - Recommended Procedures and Guidelines*, 7.5-1-03-01, 2017. [Cited on pages 27 and 29]

Schlichting, H. *Boundary-Layer Theory*. Springer, 2017. [Cited on page 7]

Rajput, R. K. *A Textbook of Strength of Materials*. S. Chand, 2018. [Cited on pages vi and 27]

Hao, W. U., Yongpeng, O., and Qing, Y. E. Experimental study of air layer drag reduction on a flat plate and bottom hull of a ship with cavity. *Oceaan Engineering*, 183:236–248, 2019. [Cited on page 3]

Pavlov, G. A., Yun, L., Bliault, A., and He, S.-L. *Air Lubricated and Air Cavity Ships Development, Design, and Application*. Springer, 2020. [Cited on page 2]

Nikolaidou, L., Laskari, A., van Terwisga, T., and Poelma, C. On the characteristics of air layer regimes. In *11th International Symposium on Cavitation*, pages 1–6. 2021. [Cited on pages vi, 13, 14, 17, and 43]

Gao, F. *What Drives Shipowners' Decision to Adopt Energy Saving Technologies (ESTs) for Ship Retrofitting?* Master's thesis, Nord University Business School, 2022. [Cited on page 1]

International Maritime Organisation. Initial IMO GHG Strategies. https://www.imo.org/en/MediaCentre/HotTopics/Pages/Reducing-greenhouse-gas-emissions-from-ships.aspx, 2022. [Cited on page 1]

Nikolaidou, L., Laskari, A., Poelma, C., and van Terwisga, T. Effect of incoming boundary layer characteristics on an air layer within a liquid turbulent boundary layer. In *12th International Symposium on Turbulence and Shear Flow Phenomena*, pages 1–6. 2022. [Cited on pages vi, 14, 15, and 16]

Fiscaletti, D., Thill, C., Nanda, S., Nikolaidou, L., Stigter, R., Delfos, R., Schreier, S., Poelma, C., Westerweel, J., and van Terwisga, T. The Multi-Phase Flow Tunnel of Delft university of Technology - Design Considerations and Preliminary Flow Characterisation. 2023. [Cited on pages vi, 20, 22, and 24]

Silverstream Technologies. Air lubrication for the shipping industry. https://www.silverstream-tech.com, 2023. [Cited on page 1]

Zhao, X. and Zong, Z. Experimental and numerical studies on the air-injection drag reduction of the ship model. *Ocean Engineering*, 2023. [Cited on pages 12 and 43]

# Nomenclature

## Abbreviations

| Symbol | Description |
|---|---|
| ALDR | Air layer drag reduction |
| AD | Analog-digital |
| BDR | Bubble drag reduction |
| FSR | Full-scale range |
| LE | Leading edge |
| MPFT | Multi-phase flow tunnel |
| PIV | Particle image velocimetry |
| PCDR | Partial cavity drag reduction |
| TALDR | Transitional air layer drag reduction |
| TBL | Turbulent boundary layer |
| ULE | Upstream of leading edge |

## Greek variables

| Symbol | Description | SI Unit |
|---|---|---|
| $\delta$ | boundary layer thickness | m |
| $\mu$ | dynamic viscosity | $\mathrm{kg \cdot m^{-1} \cdot s^{-1}}$ |
| $\nu$ | kinematic viscosity | $\mathrm{m^2 \cdot s^{-1}}$ |
| $\rho$ | density | $\mathrm{kg \cdot m^{-3}}$ |
| $\tau_w$ | wall shear stress | $\mathrm{N \cdot m^{-2}}$ |

## Roman variables

| Symbol | Description | SI Unit |
|---|---|---|
| $A_{nw}/A_w$ | non-wetted area ratio | % |
| $B$ | bias uncertainty | varied |
| $B$ | buoyancy | N |
| $C_F$ | friction coefficient | - |
| $c_f^{'}$ | local friction coefficient | - |
| $D$ | drag | N |
| $d$ | diameter | m |
| $L$ | characteristic diamater | m |
| $DR$ | drag reduction | % |
| $DR_{eff}$ | effective drag reduction | % |
| $F$ | force | N |
| $Fr$ | Froude number | - |
| $g$ | acceleration due to gravity | $\mathrm{m} \cdot \mathrm{s}^{-2}$ |
| $L$ | characteristic length | m |
| $l$ | length | m |
| $M$ | magnification factor | - |
| $P$ | precision uncertainty | varied |
| $p$ | pressure | $\mathrm{N} \cdot \mathrm{m}^{-2}$ |
| $Q_{air}$ | air injection rate | $\mathrm{m}^3 \cdot \mathrm{s}^{-1}$ |
| $Re$ | Reynolds number | - |
| $R_F$ | fricitonal resistance | N |
| $S$ | wetted surface area | $\mathrm{m}^2$ |
| $T$ | temperature | ℃ |
| $t$ | time | s |
| $t_{air}$ | air layer thickness | m |
| $U$ | uncertainty | varied |
| $u^*$ | friction velocity | $\mathrm{m} \cdot \mathrm{s}^{-1}$ |

| | | |
|---|---|---|
| $U_\infty$ | free-stream velocity | $\mathrm{m} \cdot \mathrm{s}^{-1}$ |
| $U$ | velocity | $\mathrm{m} \cdot \mathrm{s}^{-1}$ |